Electron Conduction Processes in Tantalum - Germanium Multilayers

by

Heather Leigh Johnson

A thesis

submitted to the Victoria University of Wellington
in fulfilment of the
requirements for the degree of
Doctor of Philosophy
in Physics

Victoria University of Wellington
1993

VICTORIA UNIVERSITY OF WELLINGTON

Abstract

An explosion of both theoretical and experimental research into structurally disordered materials in the late 1970s has greatly increased our understanding of these complex systems. A number of facets of the conduction processes remain unexplained, however, particularly in the area of non-simple metals. Multilayers of disordered tantalum and amorphous germanium with individual layer thicknesses of between 4 & 120Å and 13 & 220Å respectively have been prepared by vapour deposition and the in-plane resistance measured from 1.5 to 300K. Results for samples with germanium layers of sufficient thickness to prevent tunnelling between the conducting tantalum layers can be interpreted in terms of conduction in the tantalum layers alone. In these samples the behaviour of the resistance as a function of temperature and the tantalum layer thickness can be explained in terms of the interplay between quantum interference effects and disorder enhanced electron-electron interaction effects. At high temperatures the negative temperature coefficient of resistance arises from the destruction of coherent interference in the back-scattered direction by phonons. From the data, the electron-phonon scattering rate is found to be comparable in magnitude to that expected for scattering in either the "clean" or "dirty" limits while the temperature dependence of the scattering rate lies between that expected for each of these limits. At lower temperatures a turn over to a positive temperature coefficient of resistance is seen as spin-orbit scattering and superconducting fluctuations become important. At still lower temperatures the resistance is dominated by electron-electron interaction effects and we have observed a transition from three-dimensional to two-dimensional behaviour as the tantalum layer thickness is reduced. Evidence for the onset of superconductivity is seen for samples with a low temperature sheet resistance of less than 3000Ω/□.. We have also investigated samples with thin germanium layers (<40Å) in which coupling between the layers causes an increase in the superconducting transition temperature. We present some preliminary measurements which suggest that the transition from isolated to coupled tantalum layers, as the germanium layer thickness is reduced, can be followed in the form of the fluctuation conductivity.

Acknowledgements

It is with great pleasure that I thank my supervisor Dr. Joe Trodahl for suggesting the topic for this thesis and more importantly for giving me the confidence to start, the inspiration to continue and the encouragement to finish.

I would also like to acknowledge and thank Dr. Ian Vickridge of the Institute of Geological and Nuclear Sciences for performing the RBS measurements, Bob Halford and Grant Parratt of the Physics Department for designing and constructing the current controller and Laurel Quirke and Karen Reader of the University's Electron Microscope Facility for microtome sectioning of samples.

Thanks also to all the staff of the Physics Department, with special thanks to Dave Gilmour for making molehills out of my mountains.

Lastly, and most importantly, thank you to both my family and Peter.

Contents

List of Figures .... *vii*
List of Tables .... *x*
List of Symbols and Abbreviations .... *xi*

1. Introduction 1

2. Sample Fabrication 11
    2.1 Substrates 12
    2.2 Starting Materials 12
    2.3 The Vacuum System 14
    2.4 Film Deposition 15
    2.5 Sample Nomenclature 16

3. Sample Characterisation 18
    3.1 Multiple Beam Interferometry 19
    3.2 Rutherford Backscattering Spectrometry 20
        3.2.1 Introduction 20
        3.2.2 Experimental Details 25
        3.2.3 Results 27
        3.2.4 Conclusion 27
    3.3 Transmission Electron Microscopy 30
        3.3.1 Specimen Preparation 30
        3.3.2 Electron Microscopy 30
        3.3.3 Results 31
        3.3.4 Conclusion 40

4. Resistance Measurement 41
    4.1 Cryostat Insert Design 41
    4.2 Temperature Measurement 44
    4.3 Resistance Measurement 45
    4.4 Computer Program 47
    4.5 Measurement Techniques 49

4.6 Sample Ageing 49

5. Temperature Dependence of the Resistivity 52
5.1 Theoretical Predictions 52
5.1.1 Disorder in a Classical Picture 52
5.1.2 Quantum Interference Effects 55
5.1.3 The Phase Relaxation Time 60
5.1.3.1 Electron-Phonon Scattering 61
5.1.3.2 Electron-Electron Scattering 63
5.1.3.3 Spin-Spin Scattering 65
5.1.3.4 Summary 65
5.1.4 Spin-Orbit Scattering 65
5.1.5 Summary: Quantum Interference Effects 68
5.1.6 Electron-Electron Interaction 71
5.1.6.1 The Diffusion Channel 72
5.1.6.2 The Cooper Channel 74
5.1.6.3 Summary 75
5.1.7 Summary 76
5.2 Experimental Results 77
5.2.1 Overview of the Results 77
5.2.2 Characteristic Length Scales of Conduction 79
5.2.3 Room Temperature Resistivity 81
5.2.4 High Temperature Results 85
5.2.4 Low Temperature Results 96
5.2.5 Conclusion 105

6. Superconductivity 107
6.1 Influence of Structural Disorder on T_c 108
6.2 Superconductor - Insulator Transition 110
6.3 Superconducting Fluctuations Above T_c 111
6.4 Conclusions 115

7. Discussion and Conclusion 116

Appendix I: Thermometer Calibration 119

Appendix II: Current Controller 122

Appendix III: Probability of Self-Intersection in a Random Walk 126

Appendix IV: Variation in Potential at a Ta/Ge Interface 127

References 133

List of Figures

Figure 3.1 Rutherford backscattering spectrum for (a) Bi implanted Si wafer standard and (b) sample 37/1G1. 28

Figure 3.2 Rutherford backscattering spectrum for (a) sample 34/1G1 and (b) sample 18/3G4. 29

Figure 3.3 Microtome sectioning of multilayer embedded in resin block. 31

Figure 3.4 TEM bright field images of a multilayer that was sectioned by microtoming along the direction of the layers. 32

Figure 3.5 TEM bright field image of sample 16/3M3. 33

Figure 3.6 TEM bright field images of sample 32/2M2. 34

Figure 3.7 TEM bright field images of sample 30/3M6. 35

Figure 3.8 TEM bright field image of sample 20/3M6 showing layering fault. 36

Figure 3.9 TEM bright field images showing small scale non-uniformity. (a) Sample 29/3M2 and (b) Sample 28/3M5. 37

Figure 3.10 Variation in intensity across a multilayer showing Fresnel fringes. 38

Figure 4.1 Cryostat insert. 42

Figure 4.2 Exploded view of lower portion of cryostat insert. 43

Figure 4.3 (a) Diagram of sample showing scribing lines, and contact positions and (b) circuit for measuring the resistance. 46

Figure 4.4 Sample ageing over a six month period. 51

Figure 5.1 Comparison of electrical resistance characteristics of bcc and disordered Ta. 53

Figure 5.2 Three possible paths for an electron diffusing between points A and B. 57

Figure 5.3 Quantum interference correction to the resistivity for different spin-orbit scattering rates. 69

Figure 5.4 Electron-electron interaction correction to the resistance. 76

Figure 5.5 Resistance of the multilayers as a function of thickness. 78

Figure 5.6 The predicted phase breaking and diffusion lengths as a function of temperature. 81

Figure 5.7 Room temperature resistivity as a function of Ta layer thickness and estimated impurity concentration. 84

Figure 5.8 Temperature coefficient of resistance (TCR) at 300K as a function of Ta layer thickness and estimated impurity concentration. 86

Figure 5.9 Raw data (normalised to 300K) fitted to $1/R = a + bT^{p/2}$. 88

Figure 5.10 Deviation of measured high temperature resistance from fitted function $1/R = a + bT^{p/2}$. 89

Figure 5.11 Value of p (the temperature exponent of the phase breaking rate) deduced from fits to data 100-300K. 91

Figure 5.12 Deviation of measured high temperature resistance from fitted function $1/R = a + b\sqrt{cT+T^2}$. 92

Figure 5.13a "Clean" electron-phonon scattering rate from transverse phonons. 93

Figure 5.13b "Dirty" electron-phonon scattering rate from transverse phonons. 94

Figure 5.14 Schematic representation of the low temperature resistivity as the Ta layer thickness is varied. 98

Figure 5.15a Low temperature region of logarithmic variation of the conductivity for a sample with thin Ta layers. 99

Figure 5.15b Low temperature region of logarithmic variation of the conductivity for a sample with thick Ta layers. 100

Figure 5.16 Low temperature data fitted to (a) two dimensional prediction and (b) three dimensional prediction. 104

Figure 6.1 Onset of superconductivity for multilayers with thick Ge layers. 109

Figure 6.2 Superconducting transition of multilayers with Ta layers of thickness (28±5)Å and various Ge layer thicknesses. 112

Figure 6.3 Transition from decoupled to coupled behaviour of the fluctuation conductivity. 114

Figure II.1 Current contoller interconnection. 123

Figure II.2 Current controller. 124

Figure II.3 Current controller layout. 125

Figure IV.1 (a) Density of states of amorphous Ge. (b) Band diagram for isolated Ta and Ge. (c) Equilibrium band diagram for Ta/Ge interface. 128

Figure IV.2 The potential variation near a Ta/Ge interface. 131

List of Tables

Table 2.1 Ta source materials - impurity analyses. 13

Table 2.2 Deposition conditions. 17

Table 3.1 Summary of MBI and RBS measurements. 21

Table 5.1 Free electron values for Ta. 56

Table 5.2 Order of magnitude estimates for the phase breaking rates. 66

Table 5.3 Characteristic length scales of conduction and values of constants. 82

Table 5.4 Summary of results of fits to high temperature data. 90

Table 5.5 Coefficients of logarithmic variation a at low temperature. 101

Table 5.6 Parameters from fits to three dimensional QUIADs at low temperature. 103

Table I.1 Coefficients for evaluating the temperature reference function. 120

Table I.2 Coefficients for evaluating ΔZ for Rh-Fe resistance thermometer. 121

List of Symbols and Abbreviations

A	Atomic mass.
a	Film thickness or wire diameter.
a_{Ta} (a_{Ge})	Tantalum (germanium) layer thickness.
α	Sum of constants entering two dimensional logarithmic interaction and quantum interference corrections to the conductivity.
α_D	Constant entering two dimensional logarithmic interaction correction to the conductivity.
α_{FS}	Fine structure constant.
α_{QI}	Constant entering two dimensional logarithmic quantum interfenence correction to the conductivity.
α_S	Sticking coefficient.
β	Constant entering phase breaking rate.
c_L (c_T)	Longitudinal (tranverse) velocity of sound.
D	Diffusion constant.
d	Dimensionality.
δ	Pair breaking parameter.
$D'_{Ta,Ge}$	Total amount of tantalum or germaium deposited during evaporation.
ΔE	Energy change in a single collision (Chapter 5).
ΔE_{in}	Energy loss as the incident particle travels into the target before colliding (RBS).
ΔE_{out}	Energy loss as the scattered particle travels out of the target after colliding (RBS).
Δf	Defocus (TEM).
$\Delta\phi$	Phase change.
E	Energy of incident particle immediately before scattering (RBS).
e	Electronic charge.
E'	Energy of incident particle immediately after scattering (RBS).
ε_F	Fermi energy.
E_o	Beam energy (RBS).
F	Screening factor.

f_{Ta} (f_{Ge})	Fraction of the rotation period that the multilayers are exposed to the tantalum (germanium) sources.
g	Film growth rate (Chapter 2).
$\hbar$	Planck's constant.
K	Kinematic factor (RBS).
κ	Inverse screening length.
k_B	Boltzmann's constant.
k_F	Fermi wave vector.
λ	Electron wavelength.
λ_d	Interaction constant.
ℓ	Length of sample resistance path.
l	Mean free path.
l_ϕ	Average distance electron travels between phase breaking events.
l_{in}	Average distance electron travels between inelastic scattering events.
l_o	Elastic mean free path.
l_{tr}	Transport mean free path.
L_ϕ	Phase breaking length.
L_{oo}	Universal constant see (Equation 5.25).
L_T	Diffusion length.
m	Electronic mass.
M	Ionic mass.
M_1 (M_2)	Mass of incident particle (target nucleus) (RBS).
n	Number of multilayer periods.
n_e	Number of free electrons per unit area.
N	Density of states.
N_s	Number of target atoms per unit area of a given atomic species (RBS).
N_{Ta} (N_{Ge})	Number of tantalum (germanium) atoms per unit surface area.
P	Partial pressure of the residual gas (Chapter 2).
p	Temperature exponent of the phase breaking rate.
Q	Total number of incident particles (RBS).
θ	Angle through which particle is scattered (RBS).
Q_D	Number of detected particles (RBS).
Θ_D	Debye temperature.
q_{ph}	Phonon wave vector.
QUIAD	Quantum interference at defects.
R	Ratio of the arrival rates of tantalum atoms to that of residual gas at the film surface during evaporation (Chapter 2).
R	Resistance.

$R_{\square}$	Resistance per square.
R_{Q}	Quantum resistance for paired electrons.
R_1, R_2, R_3	Resistance of samples.
R_c	Critical resistance.
R_{std}	Resistance of standard resistor.
ρ	Resistivity.
ρ_m	Mass density.
r_s	Radius of sphere whose volume is equal to the volume per conduction electron.
σ_1	Conductance per unit length.
σ_2	Conductance per square .
σ_3 (or σ)	Conductance.
$\sigma(\theta)$	Scattering cross-section (RBS).
σ_B	Boltzmann conductivity.
σ_o	Temperature independent conductivity.
s	Mulitlayer period.
t	Depth at which incident particle is scattered (RBS).
t	Time (Chapter 5).
t_r	Reduced temperature.
T	Temperature.
T_c	Superconducting transition temperature.
TCR	Temperature coefficient of resistance.
T_F	Fermi temperature.
τ	Relaxation time.
τ_{ee}^{-1}	Electron-electron scattering rate.
$\tau_{el\text{-}ph}^{1}$	Electron phonon scattering rate.
τ_{ϕ}	Time over which wavefunction retains its coherence or the phase relaxation time.
τ_{ϕ}^{-1}	Phase breaking rate.
τ_{in}^{-1}	Inelastic scattering rate.
τ_{s}^{-1}	Spin-spin scattering rate.
τ_{so}^{-1}	Spin-orbit scattering rate.
υ_F	Fermi velocity.
V_1, V_2, V_3	Voltage across samples.
V_{std}	Voltage across standard resistor.
w	Width of sample resistance path.
Ω	Detector solid angle (RBS).
$\Omega/\square$	Units of sheet resistance.

ξ	Coherence length.
ξ_o	Coherence length in a pure superconductor.
Z	Atomic number.
Z_e	Number of conduction electrons per atom.

Chapter One

Introduction

The last hundred years has seen the development of a very powerful and unified theory of crystalline solids. The area of disordered solids however, has suffered comparative neglect owing to the complications which arise from the absence of lattice periodicity. With the publication of the scaling theory of localisation by Abrahams et al. in 1979 there was a surge of interest in conduction processes in disordered metals. Early theoretical work predicted that electron conduction would depend critically on the dimensionality of the system as well as on the resistance and the rate at which electrons suffer inelastic collisions. More recently, the theories have been refined to include the effects of spin-orbit and magnetic impurity scattering, while theories describing disorder enhanced electron-electron interaction have developed in parallel. The explicit predictions for the behaviour of the resistance as a function of both temperature and magnetic field provided by these theories have been investigated largely in experiments on amorphous two-dimensional thin films and three-dimensional bulk alloys. Although the results have generally been in good agreement with the theory some important points remain unresolved. The mechanism by which electrons are inelastically scattered, and the dependence of the scattering rate on temperature in different temperature regimes, is a particular puzzle. So too is the precise origin and magnitude of spin-orbit scattering.

Against this background we present the results of a study of electron conduction in disordered Ta, fabricated in the form of vapour deposited tantalum/germanium (Ta/Ge) multilayers. We have chosen to study disordered Ta, both for its intrinsic interest, as well as from fabrication considerations. Efforts to understand transport in disordered metals have tended to focus on simple metals rather than the more complicated transition metals. Now that the behaviour of simple disordered metals is relatively well understood, it seems a propitious moment to embark on a study of a more complicated metal such as Ta. Furthermore, spin-orbit scattering can be investigated in this system since Ta is expected to be a strong spin-orbit scatterer owing to its high atomic number. One problem that has hampered the study of pure disordered metals at high temperatures is the need to prepare and maintain the samples at low temperatures to prevent crystallisation. In line with the results of Nestell et al., 1982, who found that thin films of vapour deposited Ta remained amorphous until ~400K, we find no evidence of crystallisation up to the highest temperatures measured in this study (300K) and so are able to probe electron conduction mechanisms over a wide range of temperatures. The initial motivation for preparing the Ta as Ta/Ge multilayers (that is, a stack of Ta films in parallel, separated by insulating Ge layers) was to make samples with lower more easily measured total resistances as well as making the samples more mechanically robust and the Ta layers less prone to oxidation. In addition to these benefits we have found that depositing Ta onto amorphous Ge causes the Ta to form electrically continuous films at thicknesses of only a few atomic layers.[1] The ability to make ultrathin homogeneous layers has the important consequence that dimensionality effects associated with the layer thickness can be investigated across the two-dimensional to three dimensional transition.

Early studies of disordered metallic systems were centred on rapidly quenched liquid alloys made up of mixtures of transition metals or of simple metals alloyed with semi-metals, transition metals or rare earths.[2] These alloys or "metallic glasses" have higher resistivities than the crystalline phase with a mean free path deduced from the resistivity using Boltzmann's equation comparable to the interatomic distance. While the resistivity of some metallic glasses decreases as the temperature is lowered, (that is, metallic behaviour) other metallic glasses show a non-metallic increase. These results were summarised by Mooij, 1973, in what has become known as the Mooij correlation: for disordered metals with resistivities less than ~150μΩ·cm, the change in the resistivity with temperature is generally metallic (that is $d\rho/dT > 0$) while those with resistivities greater than ~150μΩ·cm generally show non-metallic behaviour ($d\rho/dT < 0$). In addition, the Hall coefficients are almost always positive and the magnetoresistance at low temperatures is found to be large and either positive or negative. This is in complete contrast to nearly free electron models in which the Hall coefficients are negative and the resistance increases only weakly in a magnetic field.

Up to 1979 all the theories put forward to explain the Mooij correlation were nearly free electron models based on the Boltzmann transport theory.[3] Underlying the use of the Boltzmann transport theory is the assumption that electrons travel along classical trajectories between collisions. In terms of transport theory, the electron is described as a propagating spherical wave originating from a single scattering site. Provided the time between successive collisions is long (that is the mean free path is much longer than the wavelength of the electron) then the assumption of classical trajectories is valid. However in the case of high resistivity metallic glasses where the mean free path approaches the interatomic distance, and the time between collisions is short, the picture of a single scattering site must be replaced by multiple scattering sites, each a centre for a propagating spherical wave. Because of the proximity of the scattering sites relative to the electron wavelength, interference between these scattered partial waves can no longer be neglected and Boltzmann transport theory in not appropriate.

---

[1] That ultrathin conductive metal films can be prepared by initially depositing an underlayer of amorphous Ge was first reported by Strongin et al., 1970.

[2] For a review of rapid quenching of liquid alloys see for example *Treatise on Materials Science and Technology*, 1981.

[3] The main models are the Ziman-Faber model (Ziman, 1961, and Faber & Ziman, 1965), Mott's s-d scattering model for transition metals (Mott, 1972) and Anderson's model involving scattering from two-level states (Anderson et al., 1972). These theories and later modifications are described and compared in reviews by Naugle,1983, and Howson & Gallagher, 1988.

In 1958, Anderson (Anderson, 1958) had shown that for sufficient disorder electron states are localised to a small region of space so that at $T = 0$ electrons cannot diffuse and the material is an insulator. In two dimensions, any finite degree of disorder causes *all* electron states to be localised at $T = 0$ whereas in three dimensions, a metal-insulator transition is predicted as the degree of disorder is increased. As the temperature is raised, electrons are able to move via phonon-assisted hopping and the conductivity increases. Jonson & Girvin, 1979, discussed a model to explain the Mooij correlation which involves phonon-assisted tunnelling via extended states near the onset of localisation.

Also appearing in 1979 was the landmark paper on the scaling theory of localisation by Abrahams et al. (Abrahams et al., 1979) which sparked papers by Anderson et al., 1979, Gor'kov et al., 1979, and Kaveh & Mott, 1981(a), 1981(b) & 1982(a), in which the conductivity in a disordered system near the onset of localisation is calculated. The conductivity is predicted to increase as the temperature is lowered although the exact temperature dependence is a function of both the temperature dependence of the inelastic scattering rate and the dimensionality of the system (two or three dimensional). This theory, which has come to be known as the theory of quantum interference or "weak localisation", gives the correction to the Boltzmann conductivity that results from quantum interference of scattered partial waves from multiple scattering sites. Bergmann, 1983, has given a rather clear physical picture of quantum interference at defects and shown how the interference of scattered partial waves leads to constructive interference or an "echo" in the backscattered direction that tends to reduce the conductivity below the Boltzmann value. Inelastic scattering events, which become more probable as the temperature is increased, destroy the phase coherence which gives rise to coherent backscattering. As a result the echo in the backscattered direction is progressively destroyed as the temperature is raised, and the conductivity increases (that is, $d\rho/dT < 0$). An interesting feature of the theory of weak localisation is the importance of the sample dimensionality in determining the way in which electron conduction depends on temperature. If the average distance an electron diffuses between collisions that contribute to the destruction of coherent interference is greater than one or more of the sample dimensions then weak localisation theory predicts, not only a much larger correction to the Boltzmann conductivity, but also a different temperature dependence than expected for a sample of infinite dimensions.

It was first suggested by Imry, 1980, that the explanation for the observed increase in the resisitivity in high resistivity metallic glasses as the temperature is lowered, is due to weak localisation. Subsequently Kaveh & Mott, 1982(b), showed how the interplay between weak localisation and Boltzmann conductivity results in a correlation similar to that noted by Mooij. Furthermore, they point out that the correlation between the magnitude and the temperature dependence of the resistivity is more general than originally envisaged by Mooij. At low temperatures, quantum interference effects will always dominate the temperature dependence of the resistivity, giving a negative slope, but at higher temperatures the slope becomes positive as inelastic scattering destroys the coherent backscattering to reveal behaviour characteristic of Boltzmann conductivity. The temperature at which the minimum in the resistivity occurs depends on the degree of disorder. For low resistivity metallic glasses the maximum occurs below room temperature while for high resistivity glasses quantum interference effects dominate the temperature dependence of the resistivity right up to the crystallisation temperature.

Thus weak localisation theory represents a qualitative description of the observed trends in the resistivity. However, it goes only part way to explaining the magnetoresistance and does not explain the observed Hall effect at all. (Weak localisation theory predicts that a magnetic field destroys coherent interference in a similar manner to inelastic scattering, the result being an increase in the conductivity or a *negative* magnetoresistance,[4] while the Hall coefficient[5] should be unaffected by interference effects.) The discrepancies between weak localisation theory and the experimental results can be essentially resolved by treating the interaction between electrons, which has so far been ignored in this discussion, and by including spin-orbit scattering. The enhancement of the interaction between electrons in disordered systems has evolved as a separate theory while the inclusion of spin-orbit coupling into weak localisation theory ~~yeilds~~ yields some suprising results.

The effect of the spin-orbit interaction on the interference of scattered partial waves is often referred to as "weak anti-localisation" because the constructive interference described earlier changes to destructive interference in the presence of strong spin-orbit coupling. Consequently at low temperatures,[6] in materials where spin-orbit coupling is strong, an increase in resistivity as the temperature is raised and a positive magnetoresistance replace the decrease in resistivity and the negative magnetoresistance of weak localisation. This was discovered theoretically by Hikami et al., 1980, and later verified by Bergmann, 1982(a).

---

[4] Kawabata, 1980(a), 1980(b).

[5] Fukuyama, 1980 and Altshuler et al., 1980.

[6] Note that at high temperatures weak localisation behaviour is regained.

In the crystalline phase, the electron-electron interaction turns out to be rather small because the full Coulomb interaction between any given pair of electrons is screened by all the other electrons. In a disordered solid the electron is so frequently scattered that the motion of the electron is diffusive rather than freely propagating and the electron cloud is therefore unable to respond quickly to the motion of a given electron, with the result that the electron-electron interaction is less well screened in disordered systems. The question of the effect of disorder on the interaction between electrons was first addressed by Alt'shuler & Aronov 1979(a). The same authors later calculated the resulting temperature and magnetic field dependence of the resistivity (Alt'shuler & Aronov 1979(b) and 1981 respectively) while Alt'shuler et al., 1980(a), calculated the magnetoresistance and Hall effect in two dimensions. The theory of electron-electron interaction predicts the same low temperature variation in the resistivity as weak localisation, but while weak localisation predicts no change to the Hall coefficient, electron-electron interaction leads to a positive, temperature dependent, coefficient.[7] To a first approximation the magnetoresistance is unaffected by the interaction between electrons.

Although it was originally thought that electron-electron interaction and weak localisation were competing theories, it is now widely recognised that both effects contribute to the observed properties of metallic glasses. At high temperatures, the interaction between electrons has a negligible influence on electron conduction and the correlation between the magnitude and temperature dependence of the resistivity embodied in the Mooij correlation can be explained in terms of the interplay between weak localisation and conventional electron transport. Quantum interference effects are also largely responsible for the magnetoresistance of metallic glasses which may be either positive or negative depending on the strength of the spin-orbit coupling in a given metallic glass. On the other hand the Hall effect is insensitive to quantum interference and the observed coefficients have their origin in interaction effects. The interpretation of the low temperature behaviour of the resistivity requires careful consideration of both effects.

We should emphasise that the quantum theory discussed here is only one of a number of descriptions which have been advanced to explain electron conduction in metallic glasses, for an overview of the subject the following review articles and papers should be consulted: Naugle, 1983, Mizutani, 1983 & 1993, Howson & Gallagher, 1988, Cote & Meisel, 1981 and Howson and Greig, 1986.

---

[7] This has been confirmed in two dimensions by Bergmann, 1984(a). Schulte et al, 1984, made very accurate measurements of the Hall coefficients of a number of Mg/Zn alloys. Gallagher et al., 1984, later reanalysed their results and found them to be entirely consistent with the predictions of electron-electron interaction theory.

Early confirmation of the theories of weak localisation and interaction[8] came from low temperature studies of the resistance as a function of temperature and magnetic field. The interpretation of the resistance in terms of weak localisation theory relies on knowledge of the temperature dependence of the inelastic scattering rate (or more properly the phase breaking rate) but neither the scattering mechanism nor its temperature dependence are fully understood. A measurement of the magnetoresistance, however, yields the phase breaking rate directly, and is hence preferable. It is generally assumed that the phase breaking rate can be written $\tau_\phi = \beta T^p$ and that possible mechanisms are electron-phonon, electron-electron or magnetic impurity scattering. In an ordered lattice the temperature dependence of the scattering rates are well known. The electron-phonon scattering rate varies as T^3 ($p = 3$) at low temperatures and as T ($p = 1$) at high temperatures ($T > \Theta_D$) while the electrton-electron scattering rate varies as T^2 ($p = 2$) and is only important at low temperatures. Provided the disorder is not too severe so that the phonon wavelength remains much smaller than the mean free path of the electrons (the so-called “clean” limit) these temperature depndences should also be observed in disordered systems. It is predicted however that in the opposite limit (the "dirty" limit) the temperature dependence of the scattering rates will be modified and will also depend on the dimensionality of the samples. Theoretical predictions for p range from 2, 3 or 4 for electron-phonon scattering to 1 or 1.5 for electron-electron scattering ($p = 1$ in two dimensions while $p = 1$ or 1.5 in three dimensions).

Magnetoresistance measurements on films of simple metals (see Bergmann, 1984(b), for a review of results up to 1984) have yielded a variety of temperature dependences but generally it is found that $p = 1$ at low temperatures (< 4K) and $p = 2$ at higher temperatures ($5 < T < 20$K). Bergmann points out that early studies failed to allow for a temperature independent term in the phase breaking rate from magnetic impurity scattering so that it is possible that the observed decrease in p at low temperature is more properly attributed to the increasing importance of magnetic impurity scattering at low temperatures. Bergmann, 1982(b), has repeated measurements of the noble metals Au, Ag, and Cu, in which he allows for magnetic impurity scattering and concluded $p = 1.65$. It is unclear how such a phase breaking rate could arise but it may be that the phase breaking rate is better described as the sum of two separate rates due to two different mechanisms as was concluded by Uren et al, 1981, in silicon doping inversion layers. More recent studies in Zn films find $p = 1.89$ in the temperature range 3-60K (Meikap et al, 1990) although again magnetic scattering is not specifically excluded. Higher values of p are generally found in Al: Bergmann, 1984(c), finds $p = 2.13$ while Santhanam & Prober, 1984, find a composite rate $\tau_\phi^{-1} = AT + BT^3$.

---

[8] This will not be discussed in detail as excellent reviews of the subject are available - see Bergmann, 1984(b), and Lee & Ramakrishnan, 1985.

In the case of non-simple metal films, measured values of p at low temperature are close to unity suggesting that, in common with the simple metals, electron-electron scattering dominates at low temperature. Sacharoff & Westervelt, 1985, find $p = 1$ for Ti below 10K after careful consideration of both the spin-orbit and magnetic impurity scattering rates while Lin & Giordano, 1987, find $p = 1.1 \pm 0.3$ in Au-Pd alloy films. The resistance measurements of Shearwood & Greig, 1991, for thin CuTi alloys suggest $p \sim 1.2$ although extracting values of the temperature dependence of the scattering rates from the resistance data is problematic. Biswas et al., 1993, find $p = 1$ below 4K in Si:Sb ultra-thin doping layers. Results in bulk (three-dimensional) disordered metals have been slower to emerge largely because the effects are much less pronounced and hence more difficult to measure. Howson & Gallagher have reviewed the results up to 1988 (Howson & Gallagher, 1988) which tend to support $p = 2$ to 3.

At low temperatures, spin-orbit coupling may also be important. Although predictions for the magnitude of the spin-orbit scattering rate, τ_{so}^{-1}, are yet to be put on a firm theoretical footing it is thought that τ_{so}^{-1} is material dependent but temperature independent. Measurements on a wide range of materials place τ_{so} in the range 0.1 - 30ps. Hickey et al, 1986, investigated CuTi alloys and in a later paper CuTiAu alloys (Hickey et al, 1987) and found that the spin-orbit scattering rate increased with increasing concentration of the species with the highest atomic number (that is with Cu and Au concentration respectively). This dependence on atomic number is not unexpected but Hickey et al, 1987 also observed, contrary to expectations, a slight dependence of τ_{so} on temperature. Although individual authors have generally obtained consistent results there does not appear to be a simple trend in the spin-orbit scattering rate when the results from various sources are collected together. This may simply be a consequence of the lack of a consistent interpretation from author to author[9] but it is also possible that surface scattering plays an important role in determining the spin-orbit scattering rate[10] and that the variation from author to author merely reflects differing surface properties.

While the low temperature behaviour of both simple and non-simple disordered metals is relatively well understood, the situation at high temperatures is more controversial. We summarise the position for high resistivity metallic glasses. A number of authors continue to favour the generalised Ziman-Faber structural model while others have fitted their high temperature results to an empirical, exponential-type temperature dependence for which there is currently no theoretical basis[11] (see Mizutani et al., 1987 and Yamada et al., 1987a&b). The remaining authors interpret their results in terms of weak localisation theory. Howson, 1984, studied $Cu_{50}Ti_{50}$ and $Ti_{50}Be_{40}Zr_{10}$ alloys with room temperature resistivities of ~200μΩ·cm and found ~~their~~ his results to be consistent with weak localisation theory with electron-phonon scattering in the clean limit as the phase breaking mechanism (that is, $p = 1$). Similar results were found by Rathnayaka et al, 1986(a) in CuTi films and by Rathnayaka et al, 1986(b) in TaIr films. Mizutani et al, 1988, studied the AgCuGe alloy system and find a value of p of slightly less than 2 for alloys with resistivities greater than 500μΩ·cm.

---

[9] Lindqvist and Rapp, 1988, show that a range of approaches produce quite different values of τ_{so}.

[10] Lindelof and Wang, 1986, describe measurements of magnesium evaporated onto a variety of substrates in which they are able to separate the contribution to the spin-orbit scattering rate from the surface and from the bulk. They find that the bulk scattering rate remains reasonably constant from film to film but the surface scattering rate is very sensitive to the underlying substrate.

Very few authors have examined one system across the transition from thin film (two-dimensional) behaviour to thick film or bulk sample (three dimensional) behaviour. As mentioned earlier, the dimensionality of a system depends on the sample thickness relative to some critical length scale, the critical length scale being different for weak localisation and interaction effects. Four methods of examining the crossover have been reported, the simplest being to vary the sample thickness or the temperature. McLachlan, 1983, found evidence for a two to three dimensional transition as a function of sample thickness in Bi films. Shearwood and Greig, 1991, investigated CuTi alloys ranging in thickness form 20Å to 50 000Å and concluded that all films show two dimensional behaviour at low temperatures with a transition, at some temperature T_x, to three dimensional interaction effects (they concluded, however, that weak localisation effects remain two dimensional). In the case of magnetoresistance studies, varying the magnetic field allows the change in dimensionality of quantum interference effects to be investigated because the critical length scale over which phase coherence is retained is a function of the field strength (see Ovadyahu et al, 1985). A less obvious method of traversing the crossover in dimensionality is to vary the thickness of the intermediate insulating layer in a disordered metal / insulator multilayer. Coupling across the thin insulator layers between effectively two dimensional disordered metal layers can induce a transition to an anisotropic quasi- three dimensional system. Such studies have been reported by Jin & Ketterson, 1986, for $Nb_{0.53}Ti_{0.47}$/Ge multilayers by Cherradi et al, 1989, in Au/Si multilayers and by Audouard et al, 1990, in Au_xSi_{1-x} and Cu/Si multilayers. Jin & Ketterson found evidence from the temperature and magnetic field dependence of the resistivity of a crossover from three to two dimensional behaviour when the Ge layers became thinner than ~30Å. Cherradi et al. and Audouard et al. found coupling across the silicon layers at a similar thickness.

---

[11] Mizutani et al., 1987, have suggested that the explanation for the exponential-type behaviour may be related to the presence of d electrons at the Fermi level.

There are two possible objections to the application of quantum interference theory to the disordered Ta in this study. Firstly the derivation of the theory of quantum interference effects is based on a simple model of a single isotropic conduction band and isotropic or "s"-scattering by impurities, assumptions which are not strictly applicable to Ta, and secondly, the theory was originally derived only for weak disorder, that is $k_F l \gg 1$, but in this study $k_F l$ is close to unity. These objections are commonly encountered problems in experimental studies of real metals. Rainer & Bergmann, 1985, considered the first problem and concluded that quantum interference theory (in the form given by Hikami et al., 1980) remains valid in the case of anisotropic impurity scattering in a metal with an arbitrary number of anisotropic conduction bands provided the diffusion coefficient, the density of states and the various scattering rates entering the theory are correctly interpreted as suitable averages. In relation to the second problem Morgan et al., 1985, in considering a generalised kinetic equation for electrons in disordered solids, concluded that the restriction $k_F l > 1$ (rather than $k_F l \gg 1$) is sufficient for weak localisation theory, which represents a first order perturbation expansion in $k_F l$, to be valid.

So far we have not touched on the question of superconductivity. In the elemental crystalline superconductors, transitions are sharp and fluctuation induced formation of Cooper pairs generally negligible at temperatures higher than twice the transition temperature. Lattice disorder tends to reduce the transition temperature as well as broadening the transition to the superconducting state. Indeed fluctuation effects can extend to temperatures well in excess of the superconducting transition temperature. An interesting question is how superconductivity is destroyed as the degree of disorder is increased, or the film thickness reduced.

While the main thrust of this investigation was to study electron conduction in disordered Ta, superconducting effects associated with the multilayer structure also proved of interest. Currently, one of the most studied problems in solid state physics is that of superconductivity in the highly anisotropic copper oxide materials. Evidence has been accumulating from a variety of recent studies (nuclear magnetic resonance, angle-resolved photoemission and microwave penetration depth measurements) that the electron pairing state is not isotropic as was originally thought. This has been taken as evidence of d-wave, rather than BCS-like s-wave, pairing by a number of groups although others have proposed that the high T_c materials be modelled as two-dimensional superconducting layers (within which the electrons pair in BCS-type states) coupled by Josephson-like tunnelling.[12] The investigation of the second of these models is complicated because of the difficulty in experimentally varying the model parameters in the copper oxide materials. A number of authors have reported measurements of conventional superconductor / insulator multilayers[13] and have interpreted their results as a model system for high temperature superconductors. Such systems have the advantage that detailed measurements of the properties of a single two-dimensional layer are possible and that the interlayer coupling can be systematically varied by altering the thickness of the insulating layers.

---

[12] See Levi, 1993, and references therein.

In this thesis we present the results of measurements of the resistance of Ta/Ge multilayers as a function of both temperature and layer thickness. Although magnetoresistance measurements are preferable for extracting information on the various scattering rates at low temperature, the resistance measurements have provided a wealth of interesting information. In Chapters Two and Three, the fabrication and characterisation of the multilayers is described, while Chapter Four deals with the measurement of the resistance. The results are presented in Chapter Five and their analysis in terms of the theories of weak localisation and interaction effects are discussed. Chapter Six explores superconductivity in the Ta/Ge multilayer system.

---

[13] Neerinck et al., 1990 &1991, have studied Pb/Ge multilayers, while Steel et al.,1993, studied MoGe/Ge multilayers in this context. The study of Josephson-coupled two-dimensional superconductors is not new. Ruggiero et al., 1980 & 1982, for example studied Nb/Ge multilayers.

Chapter Two

Sample Fabrication

Vapour deposited films of high purity and uniformity are relatively simple to prepare routinely. Careful choice of deposition parameters give fine control over the physical dimensions and structure of the films. This makes vapour deposited films ideally suited to the study of disordered metals especially where two dimensional effects are of interest (see for example Markiewicz and Harris, 1981, van den Dries et al., 1981, and Bergmann, 1982(c)). It must be borne in mind however, that a monolayer of contaminates will be chemisorbed or physisorbed onto the surface of the film on a time scale of the order of nanoseconds at atmospheric pressure. This will, in most cases, be followed by the formation of stable compounds (oxides, nitrides, hydrides or carbides). To prevent surface degradation, films need either to be fabricated, stored and measured under ultra-high vacuum or to be shielded from atmospheric gases by a protective coating. This requirement is particularly stringent in the case of Ta. Jackson & Haas, 1967, have shown Ta to be one of the most effective getters, taking up common atmospheric gases very rapidly. Mathieu et al., 1985, and more recently Tapping et al., 1988, have measured the natural surface oxide on Ta to be of the order of 30Å which represents a significant problem when preparing films of thicknesses in the range 4-400Å.

Although a vacuum chamber for film deposition was available, in situ measurements on the samples were not possible. Instead, thin Ta layers were protected from oxidation by fabricating them in the form of Ta/Ge multilayers. A multilayer system has additional advantages over a single film in that tunnelling between the Ta layers can be studied. In addition, a multilayer is more mechanically robust and small variations in the substrate surface have a less significant effect on the measured properties. Moreover, the effective resistance of several Ta layers in parallel is less than that of a single Ta film, making resistance measurements, especially of very thin, highly resistive films, less technically demanding.

In the current study Ta/Ge multilayers were vapour deposited on glass substrates in an ultra high vacuum system. The Ge was evaporated by resistive heating in a tungsten boat, while an electron gun was needed to evaporate the Ta. The multilayer structure was made by alternately rotating the substrates at an even rate through the Ta and the Ge vapour streams. This chapter describes the method of sample fabrication in detail.

2.1 Substrates

Films to be studied by Transmission Electron Microscopy (TEM) were deposited on disks cut from 60μm thick mylar sheet. The mylar substrates were cleaned by rinsing in acetone. Any excess acetone was drained by touching the edge of the disk onto a dry lint free cloth. No problems with film peel-off or streaking were experienced using this method. Samples destined for all other measurements were deposited on glass substrates cut from microscope slides. At first the glass substrates were cleaned according to the method given by Long, 1989, which involved soaking the substrates in Decon 90, followed by a neutralising acid rinse, ultrasonic cleaning in water, and degreasing in isopropanol. This method often produced a bloom on the glass substrates that necessitated a second cleaning. A simpler method based on a suggestion from Beaglehole[1] was found to be faster and more reliable. The method was as follows. Any visible dirt was removed with a dampened cotton bud, care being taken to avoid scratching the glass. The substrates were then immersed briefly (~10 seconds) in a standard glass cleaning solution of HF, HNO_3 and water mixed in the ratio 1:7:12 by volume. This was quickly followed by a high purity water rinse.[2] The last step was to clean ultrasonically in water for 15 minutes, with water changes every five minutes. Immediately prior to insertion into the vacuum system the substrates were dried by blowing with instrument grade nitrogen gas (purity 99.99% minimum).

2.2 Starting Materials

The Ge source used was 99.9999% pure Ge lumps as supplied by Goodfellows Metals Limited, Cambridge, England. Large lumps were broken up to ensure good thermal contact between the lumps and the tungsten boat. Failure to do this resulted in lengthy melting times and the necessity to take extreme care not to overheat and break the boat.

Two different Ta sources were used. The first (hereafter 'low purity Ta') was

---

[1] D. Beaglehole, private communication.

[2] Water of purity exceeding type I reagent grade water standard from a *Milli-Q Ultrapure Water System* by Millipore Corporation, Australia.

ELEMENT	IMPURITY CONCENTRATION ppm	
	Low Purity *(Goodfellows)*	High Purity *(ESPI)*
Ag		<0.10
Al	5	1.80
As		<0.10
C	25	
Ca	2	0.08
Cd		<0.10
Cl		0.24
Co	1	<0.20
Cr	5	0.29
Cu	2	0.60
Fe	30	0.46
Ga		<0.10
Ge		<0.10
H	2	
Hf		<0.10
In		<0.10
K		0.69
Li		0.05
Mg	5	0.19
Mn	2	<0.10
Mo	100	0.15
N	25	
Na	10	0.41
Nb	<500	
Ni	3	0.91
O	50	
P		0.79
Pb		<0.10
Pd		<0.10
Pt		<0.10
Rh		<0.10
S		0.23
Sb		<0.10
Si	10	1.20
Sn	2	<0.10
Ti	20	5.00
V	5	0.24
W	100	2.40
Zn		0.33
Zr	10	

Table 2.1 Ta source materials: typical impurity analyses as supplied by manufacturers.

annealed, 6.35mm diameter Ta rod of 99.9% purity, again supplied by Goodfellows. Typical impurity analysis for this product is shown in Table 2.1. Two approximately 8mm lengths cut from the rod provided a stable evaporant source. It is possible that magnetic impurities, even at extremely low concentration levels of a few parts per million, could give rise to observable features in the resistivity. As a comparison, a number of samples were made from a second, higher purity, melt zone refined, 0.030" diameter Ta wire source (hereafter 'high purity Ta') supplied by Electronic Space Products

International (ESPI), California. A typical analysis of this product shows impurities to be present at a level of less than 20ppm (see Table 2.1). The wire was coiled into a dense lump approximately 1cm in diameter for use in the electron gun. Nevertheless some difficulty was experienced in maintaining a steady rate. In each case, the Ta source was cleaned in dilute hydrofluoric acid[3] to remove any surface oxide before placing in the vacuum system.

2.3 The Vacuum System

Samples were prepared in a Varian *FC-12E Ultra High Vacuum System*[4]. After sustaining some damage, the glass bell jar was replaced by a stainless steel top as described by Homewood, 1990. Although this led to an increase in the total volume to be evacuated, the stainless steel top could be outgassed more effectively, resulting in lower ultimate pressures.

Ta requires a very high evaporation temperature. Even when using an electron gun to evaporate the Ta source, considerable heating and consequent outgassing of surrounding equipment and chamber walls occurs. Extensive outgassing, leading to a rise in pressure, causes two problems. Firstly, ionization of gas molecules in the vicinity of the electron gun reduces the power and focus of the electron beam, and at pressures above 10^{-5} Torr, dielectric breakdown can occur. The second problem is the incorporation of gaseous impurities into the sample. In a review on the preparation and properties of Ta thin films, Baker, 1972, gives the ratio R of the arrival rates of Ta atoms and of residual gas at the film surface during evaporation as

$$R = 2\mathrm{x}10^{-8}\,\frac{g}{P} \tag{2.1}$$

where g is the film growth rate in Å·min^{-1} and P is the partial pressure of the residual gas (taken to be air) in Torr. The value of the sticking coefficient, α_s, of oxygen on Ta (i.e. the fraction of impinging oxygen molecules that will be incorporated in a Ta film) is about 10^{-2} according to a measurement by Maissel and Schaible, 1965. Thus to keep the impurity concentration (given approximately by α_s/R)[5] below 1000ppm using an evaporation rate of 100Å·min^{-1} requires the partial pressure of residual gas to be less than 2x10^{-7} Torr. Described below is the rigourous pumpdown and outgassing procedure adopted in an attempt to achieve deposition pressures of 10^{-7} Torr or better.

---

[3] Dilute HF is a commonly used etch for Ta_2O_5 - see for example Kern & Schnable, 1987.

[4] Varian Associates, Palo Alto, California.

[5] Baker gives the impurity concentration incorrectly as $\alpha_s R$.

Two Varian *VacSorb*[6] pumps roughed the sample chamber to ~10^{-4} Torr. When using the stainless steel top, the larger volume required initial pumping to 1 Torr with a Venturi pump to avoid overloading the *VacSorb* pumps. Glass fibre insulated heating tape wound around the entire system heated the exterior to ~100°C[7]. The following day the sample chamber was briefly pumped with one of the *VacSorb* pumps prior to opening the poppet valve to the lower chamber. This chamber is kept constantly at pressures below 10^{-5} Torr by five Varian *VacIon* pumps and a three filament titanium sublimation pump. Once the poppet valve is opened the entire chamber rapidly attains a pressure of 10^{-7} Torr at which point the Ta and Ge sources are melted and outgassed. Strausser, 1968, has reported that final outgassing rates after a lengthy 150°C bake-out differs little from those for a shorter 300°C bake-out. Bearing in mind the risk of damaging the viton, outgassing was achieved by baking at 100-150°C for periods of about a week. In addition, internal components surrounding the electron gun were further outgassed by heating the Ta source to red hot for several minutes every half hour until the heating did not cause an appreciable pressure rise. The vacuum system was then left to cool overnight. Base pressures attained were less than 10^{-9} Torr.

2.4 Film Deposition

Layering of the samples was achieved using a rotating substrate assembly designed by Grant Williams. As it is described in detail in his thesis (Williams,1990), only a brief outline will be given here. The substrates are rotated above each of the two isolated sources in turn. Three geared substrate holders, each with six samples, allow simultaneous fabrication of three sets of multilayers of different layer thicknesses. A shield that shadows the substrates during some fraction of the rotation period gives further control over the relative layer thicknesses. Pure films of Ta and of Ge were deposited onto glass substrates held in one of two stationary substrate holders mounted either side of the rotating substrate assembly for later layer thickness determination using Multiple Beam Interferometry. The electromagnetic shutter described by Williams proved unreliable at the high temperatures used in this study. It was replaced by a centrally pivoted shutter attached, via a chain drive, to a mechanically operated rotary motion feedthrough. Switches mounted externally on the body of the feedthrough were triggered in the open and closed positions by the operating lever. The signal from the switches was used to synchronise the opening and closing of the shutter with the starting and stopping of the substrate rotation.

---

[6] VacSorb pumps contain a synthetic zeolite with a large surface to volume ratio which will physically absorb most gases when cooled to liquid nitrogen temperatures.

[7] The viton seal to the stainless steel top or bell jar precluded bake-out above 200°C. In practice temperatures were kept below 120°C to prevent vulcanisation of the viton.

The vapour stream of Ta is produced by a 2kW Varian *e-Gun* capable of Ta deposition rates up to 300Å·min^{-1}, 250mm directly above the source. Somewhat higher rates can be achieved if heat loss is reduced by operating the electron gun with an evaporant soiled crucible. In practice, rates between 70 & 360Å·min^{-1} (as measured at the substrates) were used. The Ta did not wet the copper crucible of the *e-Gun*. The Ge was evaporated from a resistively heated tungsten boat at rates between 200 & 1000Å·min^{-1} (again, as measured at the substrates). Evaporation rates were controlled by two Sloan *DDC-1000 Digital Deposition Controllers* that use quartz crystal monitors. During film deposition, fluctuations about the average rate were of the order of 5 to10%. The fluctuations, were of sufficiently high frequency that the total evaporant deposited varied by only a few percent from layer to layer.

Details of the deposition conditions of each evaporation are given in Table 2.2. Maximum evaporation pressures range between 4x10^{-9} Torr and 2x10^{-5} Torr. Estimated impurity concentrations in the Ta layers (calculated from equation 2.1) lie between 0.0007% and 23%.

2.5 Sample Nomenclature

Samples are identified as *x*/*ySz* where *x* refers to the evaporation number, *y* denotes the substrate holder (y = 1, 2 or 3), *S* is a symbol identifying the substrate (G = glass, M = mylar) and *z* indicates the position on the substrate holder (z = 1, 2, 3, 4, 5 or 6). Thus, for example, samples 43/1G3 and 43/1M2 will have the same layer thicknesses but the top and bottom layers may not be identical.

Evaporation number	Maximum Evaporation Pressure Torr	Ta Deposition Rate Å·min^{-1}	Impurity Content in Ta Layer ppm
18	4×10^{-7}	228	880
19	4×10^{-6}	152	13 000
20	2×10^{-6}	87	11 000
21	5×10^{-7}	65	3 800
22	8×10^{-7}	87	4 600
23	9×10^{-7}	87	5 200
28	1×10^{-6}	56	8 900
29	1×10^{-8}	56	89
30	4×10^{-9}	115	17
31	3×10^{-9}	219	7
32	2×10^{-6}	43	23 000
33	1×10^{-6}	108	4 600
34	6×10^{-7}	108	2 800
35	4×10^{-7}	217	920
36	2×10^{-7}	65	1 500
37	2×10^{-6}	43	23 000
38	2×10^{-5}	43	230 000
39	3×10^{-7}	87	1 700
42	2×10^{-8}	282	35
43	2×10^{-8}	155	65
50	8×10^{-8}	144	280

Table 2.2 Deposition conditions. Approximate values only are given for the maximum pressure during film deposition and the Ta deposition rate. An upper limit for the impurity concentration in the Ta layer is estimated using Equation 2.1 and assuming a sticking coefficient of 10^{-2}.

Chapter Three

Sample Characterisation

The electrical properties of the multilayers depend critically on their physical properties - the number of layers, the thickness of each layer, the structure of the material within the layer, the structure of the interface and the level of impurities. To interpret the resistance measurements correctly it is therefore important to determine as many of these characteristics as possible.

The rotation rate of the substrates during film deposition, together with the total deposition time, determines the number of layers, while the layer thicknesses can be estimated from the deposition rates. A more accurate estimate of the layer thickness is derived from a Multiple Beam Interferometry (MBI) measurement of the thickness of simultaneously evaporated films. Although this technique offers a rapid and simple cross-check of the expected layer thicknesses, a direct measurement is clearly preferable. Rutherford Backscattering Spectrometry (RBS) provides such a technique. RBS measures the number of atoms per unit area of each species in the multilayer, from which the number of atoms per layer can be deduced provided the number of layer pairs is known. The information from RBS differs slightly from a measurement of the layer thickness but a knowledge of the number of atoms per layer can be combined with an assumed density to give approximate layer thicknesses if necessary. Transmission Electron Microscopy (TEM) has the potential to give information on the uniformity, structure, composition, number and thickness of the layers as well as the diffuseness of the boundaries between the layers.

All three of these techniques were applied to the multilayers to give a comprehensive picture of their morphology. MBI and RBS give a quantitative measure of the average layer size while TEM shows qualitatively how closely individual layers approximate average properties. The MBI, RBS and TEM measurements will be discussed in the following sections.

3.1 Multiple Beam Interferometry

Multiple Beam Interferometry (MBI) uses an angled plate to produce a wedge shaped air gap above a specimen. Multiple reflections formed by illuminating the air gap with a monochromatic light source produce an interference pattern. Any height irregularity or step on the surface of the specimen results in a bending of the fringe pattern by an amount proportional to the vertical variation in the specimen.

Using a Varian *Å-scope* interferometer,[1] film thicknesses can be measured with a precision of 30Å. This is clearly insufficient for a direct measurement of the layer thickness even if individual layers could somehow be isolated. Instead, measurements were made on substrates that had been exposed for the duration of the evaporation to only one of the sources (see Section 2.4). The thickness of Ta in these pure films, D_{Ta}, can be related to the total thickness of Ta in simultaneously deposited multilayers provided firstly, that the film density does not depend on the film thickness, and secondly, that the deposition rate at the multilayer substrates and at the pure film substrates is the same. The Ta layer thickness in the multilayer samples, a_{Ta}, is then given by

$$a_{Ta} = \frac{D'_{Ta} \cdot f_{Ta}}{n} \tag{3.1}$$

where f_{Ta} is the fraction of a rotation period that the multilayers were exposed to the Ta source and n is the number of layers. A similar calculation yields the Ge layer thickness.

In practice there is considerable spatial variation in the deposition rate, both in the vertical and in the horizontal plane. Vertical variation in the deposition rate arises because the deposition rate falls off approximately as the square of the distance from the evaporant source. As the substrates for MBI measurements are ~3mm further from the sources than the multilayer substrates, a correction of approximately 2.4% should be applied to Equation 3.1. The horizontal variation in the deposition rate is more pronounced. Although the Ge vapour stream is uniform to within 2% over the length of the substrate assembly, the Ta vapour stream can vary by up to 20% over the same length. To improve the accuracy of the measurement, a series of measurements corresponding to different positions along the length of the substrate assembly are taken. The deposition rate at a given substrate holder is then taken from the average of the measurements of the two pure films closest to that substrate holder during the deposition.

A more serious problem with this method is the assumption that the density in the individual layers of a multilayer is the same as the density in the corresponding "bulk", pure film used for the MBI measurement. It is generally observed that the density of a film decreases with decreasing film thickness. To take an example, Hartman, 1965, found that the density of a 200Å aluminium film was less than 75% of the bulk density while that of a 1000Å aluminium film was ~96% of the bulk density. It is almost certainly the case that the density of Ta and Ge films also depends on thickness. Thus thicknesses deduced from MBI measurements may be in error by more than 25%.

---

[1] Model 980-4006, Varian Associates, Palo Alto, California.

MBI measurements on the "bulk" pure films were made in the following manner. A step at the edge of the film was formed by masking part of the glass substrate during the evaporation. For good fringe visibility, a highly reflecting opaque layer of aluminium, approximately 1000Å thick, was deposited at normal incidence over the film. The height of step at the edge of the film (i.e. the "bulk" film thickness D'_{Ta} or D'_{Ge}) was measured using the Varian *Å-scope* interferometer. Layer thicknesses were then deduced using Equation 3.1 corrected for vertical variation in the deposition rate as described above. Table 3.1 lists the results of the MBI layer thickness measurements. The uncertainty quoted in the measurement is a result of both the large variation in the deposition rate along the length of the substrate assembly and the resolution of the *Å-scope* itself.

It can be seen that MBI measurements of the layer thicknesses have severe limitations. For some samples the uncertainty in the measurement is as large as 40%. It proved impossible to measure the thicknesses D'_{Ta} or D'_{Ge} in cases where they were less than about 200Å owing to distortions in an old Fizeaux plate.[2] The possibility that the density of the films depends on their thickness introduces a further uncertainty of unknown magnitude into the measurement.

3.2 Rutherford Backscattering Spectrometry

3.2.1 Introduction

Rutherford backscattering spectrometry or RBS is based on Rutherford's famous experiment in which he observed the recoil of alpha particles from a gold foil. RBS is a surface analysis technique that identifies different atomic species and measures their absolute concentrations, making it ideal for characterising thin film multilayers. A brief outline of the technique will be given below. More detailed descriptions can be found in

---

[2] The angled plate of the *Å-scope* .

Sample	Ta layer thickness deduced from;			Ge layer thickness deduced from;		
	Å-scope	RBS surface energy approximation	RBS ΔE correction	Å-scope	RBS surface energy approximation	RBS ΔE correction
	Å	10^{15} atoms·cm^{-2}	10^{15} atoms·cm^{-2}	Å	10^{15} atoms·cm^{-2}	10^{15} atoms·cm^{-2}
18/1G4	88±3	35±2	35±2	77±6	38±2	38±2
18/2G4	132±5	61±4	60±4	116±9	63±4	61±4
18/3G4	198±8	94±5	91±5	173±13	83±5	81±5
19/2G4	77±6	39±2	-	95±3	48±3	-
20/2G4	15±2	6.2±0.4	6.0±0.4	81±2	35±2	34±2
21/2G4	5±1	2.3±0.1	2.2±0.1	32±1	14.7±0.9	14.3±0.9
22/2G4	27±1	13.0±0.7	12.5±0.7	77±4	36±2	34±2
23/1G4	20±3	10.4±0.6	10.1±0.6	62±1	26±2	25±2
23/2G4	40±5	19±1	-	93±1	45±3	-
23/3G4	66±2	30±2	-	139±1	63±4	-
28/1G1	11±1	5.2±0.3	5.1±0.3	68±2	27±2	27±2
28/2G1	21±1	10.0±0.6	9.7±0.6	101±3	48±3	47±3
28/3G1	34±2	18±1	17±1	152±4	70±4	67±4
29/1G1	10±3	5.3±0.3	5.1±0.3	101±3	43±3	42±3
29/2G1	17±2	8.1±0.5	7.7±0.5	151±5	73±4	70±4
29/3G1	27±3	11.7±0.7	11.2±0.7	227±7	102±6	98±6
30/1G1	45±1	21±1	21±1	58±1	23±1	22±1
30/2G1	73±3	34±2	33±2	88±1	41±3	40±3
30/3G1	100±10	47±3	46±3	131±2	61±4	60±4
32/1G1	11±2	4.7±0.3	4.6±0.3	54±1	22±1	21±1
32/2G1	18±3	8.8±0.5	8.6±0.5	82±2	37±2	36±2
32/3G1	26±5	13.3±0.8	13.0±0.8	122±3	54±3	53±3

Table 3.1 Summary of MBI and RBS measurements. Where MBI measurements are unavailable, approximate layer thicknesses deduced from the evaporation rates are quoted. (Table continued overleaf.)

Table 3.1 continued.

Sample	Ta layer thickness deduced from;			Ge layer thickness deduced from;		
	Å-scope	RBS surface energy approximation	RBS ΔE correction	Å-scope	RBS surface energy approximation	RBS ΔE correction
	Å	10^{15} atoms·cm^{-2}	10^{15} atoms·cm^{-2}	Å	10^{15} atoms·cm^{-2}	10^{15} atoms·cm^{-2}
33/1G1	26±6	11.6±0.7	11.4±0.7	53±2	20±1	20±1
33/2G1	49±5	23±1	22±1	80±3	38±2	37±2
33/3G1	70±4	32±2	31±2	120±5	56±3	54±3
34/1G1	280±40	118±7	-	530±10	210±10	-
34/2G1	350±20	146±9	-	530±10	230±20	-
34/3G1	367±6	160±10	-	530±10	230±14	-
35/1G1	~26	11.1±0.6	-	13.9±0.4	5.9±0.4	-
35/2G1	~26	13.9±0.8	13.6±0.8	20.8±0.6	9.8±0.6	9.6±0.6
35/3G1	~26	15.2±0.9	14.9±0.9	31.2±0.9	13.9±0.9	13.6±0.9
36/1G1	27±6	11.5±0.5	-	50±1	18.9±0.9	-
36/2G1	53±6	24±1	-	50±1	22±1	-
36/3G1	82±5	38±2	-	50±1	21±1	-
37/1G1	7±3	2.7±0.2	-	46±8	19.3±0.9	-
37/2G1	18±3	6.0±0.3	-	46±8	21±1	-
37/3G1	28±5	11.0±0.7	-	46±8	19±1	-
38/1G4	~4	1.36±0.07	-	~74	31±2	-
38/2G4	~6	3.1±0.1	-	~74	33±2	-
38/3G4	~9	6.0±0.2	-	~74	34±2	-
39/1G3	~20	10.2±0.5	-	~80	44±2	-
39/1G6	~20	10.0±0.5	-	~80	45±2	-
39/3G3	~40	30±3	-	~80	46±2	-

standard texts (see for example, Chu et al., 1978).

In essence, RBS is a classical scattering experiment in a central force field. A monoenergetic beam of charged particles – usually singly charged helium ions – bombards the sample. The particles are scattered through large angles via single Coulomb interactions with positively charged, target nuclei. A nuclear particle detector, placed as close as practical to the backscattered direction, gives an output pulse proportional to the energy of each detected particle.

In being scattered, the incident particle imparts some fraction of its energy to the heavier target nucleus. Assuming the target nucleus is initially at rest, the energy lost by the incident particle (determined from conservation of energy and momentum) is

$$\Delta E_s = E - E' = E - KE = E(1 - K) \tag{3.2}$$

where E and E' are the energies of the incident particle immediately before and immediately after scattering, and K is the kinematic factor:

$$K = \frac{E'}{E} = \left[\frac{\left(M_2^2 - M_1^2\sin^2\theta\right)^{1/2} + M_1\cos\theta}{M_2 + M_1}\right]^2 . \tag{3.3}$$

Here M_1 is the mass of the incident particle, M_2 is the mass of the target nucleus and θ is the angle through which the particle is scattered.[3] It can be seen that, at a given angle, the energy of the scattered particle will be characteristic of the mass of the target nucleus. The elements present in a sample can therefore be identified.

The number of target atoms per unit area of a given atomic species, N_s, is determined from the number of detected particles of the appropriate energy, Q_D. The number of detected particles will also depend on the scattering cross-section $\sigma(\theta)$, the detector solid angle Ω and the total number of incident particles Q as

$$Q_D = \sigma(\theta) \cdot \Omega \cdot Q \cdot N_S . \tag{3.4}$$

For Coulomb scattering the cross-section is given by

---

[3] Note that the maximum value of K occurs at $\theta = 180°$, where the incident particle is reflected back along its incoming path. Therefore placing the detector as close as possible to the incoming particle beam (and directed at the sample) gives the best energy resolution.

$$\sigma(\theta) \;=\; \left(\frac{Z_1 Z_2 e^2}{4E}\right)^2 \frac{\left[\left(M_2^2 - M_1^2 \sin^2\theta\right)^{1/2} + M_2 \cos\theta\right]^2}{M_2\left(M_2^2 - M_1^2 \sin^2\theta\right)^{1/2}} \; . \tag{3.5}$$

By determining the characteristics of the detector from a spectrum of a standard of known composition, calculating the cross-section from Equation 3.5, and deducing the total number of incident particles in the beam from the time integration of the current incident upon the target, the composition of the target can be determined from Equation 3.4.

In addition to determining the type and concentration of atomic species present in a sample, RBS can give information on their depth distribution. The energy E that enters Equations 3.2 and 3.5 will only be equal to the beam energy E_o if the particle collides with a nucleus on the very surface of the sample. In general the particles travel some distance into the sample before suffering a collision and in so doing lose energy in numerous inelastic collisions with electrons. If the particle travels a distance *t* before being elastically scattered in a Coulomb interaction with a nucleus, its energy just before the collision will be given by

$$E = E_o - \Delta E_{in} = E_o - \int_0^t \frac{dE}{dx}\,dx \approx E_o - \left.\frac{dE}{dx}\right|_{E_o} \cdot t \, . \tag{3.6}$$

The stopping power dE/d*x* of a material is usually calculated from Bohr's classical fast collision theory (see Bohr, 1913). As the backscattered particle travels a distance $t\,/\cos\theta$ out of the sample it will suffer further inelastic collisions that reduce its energy by an amount

$$\Delta E_{out} = \int_{t/\cos\theta}^{0} \frac{dE}{dx}\,dx \approx \left.\frac{dE}{dx}\right|_{E_1} \cdot \frac{t}{|\cos\theta|} \tag{3.7}$$

where $E_1 = E_o - \Delta E_{in} - \Delta E_s - \Delta E_{out}$ is the energy of the particle measured at the detector. If, for example, a particular atomic species is distributed evenly to a maximum depth d_m then the bombarding particles will be backscattered with a range of energies - the maximum energy $E_o - \Delta E_s$ is characteristic of the atomic species, while the minimum energy depends on d_m.

3.2.2 Experimental Details

RBS experiments were carried out at the Institute of Geological & Nuclear Sciences Limited, Lower Hutt, with the help of Dr. Ian Vickridge.

The Accelerator

The 2.0 MeV beam of singly charged helium ions was produced by a 3MV single ended vertical Van de Graaff accelerator.[4] The choice of beam energy is inevitably a trade-off between good energy separation of the elements (see Equation 3.2) and a large cross-section (see Equation 3.4). A 2MeV beam allowed adequate energy separation of the Ta and Ge signals ($\Delta E_s(\text{Ta}) = 166\text{keV}$ and $\Delta E_s(\text{Ge}) = 389\text{keV}$) while ensuring large enough cross-sections that counting times were not prohibitively long.

The Target Chamber

Most experiments were performed in the microprobe chamber described by Coote and Sparks, 1981. The beam current was set to values below 100nA by an adjustable aperture in the beam line. Four magnetic quadrapole lenses focussed the beam to a 1x1mm square spot.[5] The beam line and target chamber were evacuated to below 10^{-6} Torr. Care was taken to ensure that the samples were electrically connected to the sample holder since in early experiments unexpected sample charging caused problems with current integration.

Some later measurements were performed on a second beam line of the accelerator in a new dedicated Ion Beam Analysis chamber in which up to 18 samples could be mounted at once, minimising the number of pumpdown cycles required. The experimental parameters were essentially the same as those for the microprobe chamber in all other respects.

Charge Integration

The total number of incident particles was measured using an Ortec[6] 439 beam current integrator connected to the insulated target chamber that acted as a Faraday cup for charge collection. Beam currents were kept below 100nA.

---

[4] Model KN, High Voltage Engineering Corporation, Burlington, Massachusetts.

[5] Initially, it was found that the beam could not be focussed to a single spot. A poor vacuum appeared to be causing partial ionisation of the beam to He^{++}. The problem was fixed by the addition of extra pumping facilities.

[6] AG & G Ortec, Oak Ridge, Tennessee.

The Detection System

Backscattered particles were collected at an angle $\theta = 163.5°$ by an Ortec, 100µm partially depleted Si surface barrier detector. It was placed ~75mm from the sample surface and collimated with a 2mm^2 diaphragm. The solid angle of the detector is therefore of the order of 0.4msr. The sample-detector distance in the dedicated Ion Beam Analysis chamber was ~40mm giving a larger solid angle of ~1.2msr. Variations in the source-detector distance due to the different thicknesses of sample and standard were less than 0.5mm, giving an error of the order of a few percent. The count rate measured by the detector was kept below 1000 counts per second by controlling the beam current. Dead-time was less than 5% and variation in the dead-time between samples was negligible. The output of the detector was fed to an Ortec 919 multi-channel buffer controlled by Ortec's *Maestro for Windows 3* multi-channel analyser emulation software.

Primary Standard

The primary standard used to determine the solid angle of the detector was a piece of a Bi-implanted Si wafer. The elastic scattering cross-section of Bi for 2MeV He$^+$ has been accurately measured (see Climent-Font, 1991) making Bi suitable for use as a reference standard. The Si wafer had been amorphised by argon bombardment prior to the implantation of the Bi. Channeling of the probing He$^+$ beam in the standard was not therefore expected. (Amorphisation also prevents channeling of the Bi atoms to depths greater than the projected range of 220Å during implantation). The Bi content, derived from a measurement[7] relative to a similarly fabricated Harwell[8] standard, was $(5.7 \pm 0.1)\times 10^{15}$ atoms·cm^{-2}.

A spectrum from the primary standard was collected before and after each series of measurements on the samples. Variations in the spectra were within expected statistical fluctuations.

Secondary Standard

A plasma oxidised Ta layer (approximately of the composition Ta_2O_5) on a Si substrate was used as a secondary standard to verify the solid angle of the detector and to give an approximate energy calibration.

---

[7] Calibration performed by C. Cohen, University of Paris 7, Paris.

[8] Atomic Energy Research Authority, Harwell, Oxfordshire.

Analysis

Energy calibration, peak integrals and spectra simulations were done using the RBS spectra simulation programme RUMP (see Doolittle, 1985) version 3.51. This programme uses a fifth order polynomial fit to the empirical stopping power values of Ziegler et al, 1982.

Equations 3.4 & 3.5 together with the surface energy approximation $E = E_o$ was used to find the number of atoms per unit surface area of Ta and of Ge present in a sample from the measured spectra. This approximation is reasonable provided the total sample thickness is small. For thicker samples, the mean energy approximation $E = E_o - \Delta E/4$ (where ΔE is the peak width) was used.

3.2.3 Results

The results of measurements of the number of atoms per unit area per layer are collected in Table 3.1. Figure 3.1(a) shows a spectrum for the primary standard. The peak at ~1.85MeV corresponds to the buried Bi, and the bulk yeild at low energy to the Si substrate. Resolution at low energies is limited by energy straggling but this does not effect the determination of the detector solid angle. Figure 3.1(b) shows a typical spectrum of a Ta/Ge multilayer deposited on glass. The individual Ta and Ge layers are too thin to be resolved. The spectrum can be well fitted by assuming the Ta and the Ge are evenly distributed throughout the multilayer. The composition of the glass is approximately $SiCa_{0.2}Na_{0.4}O_3$ although the presence of boron, which is too light to be detected, cannot be ruled out.

Individual Ta and Ge layers of thicknesses greater than approximately 200Å can be resolved. The spectrum of a Ge-Ta-Ge sandwich is shown in Figure 3.2(a). That of a multilayer with three Ta layers and four Ge layers is shown in Figure 3.2(b). To improve the resolution of the layers, the sample was tilted at 45° to the incident beam, thereby increasing the effective layer thicknesses by a factor of $\sqrt{2}$. Further tilting the sample causes the Ta peaks to overlap the Ge peaks. The considerable variation in the Ta layer thicknesses (~15%) found by RUMP was expected from consideration of the measured evaporation rates and is not representative of multilayers from other evaporations. The surface Ge layer was incomplete.

3.2.4 Conclusion

Rutherford Backscattering spectrometry provides a rapid and accurate method for

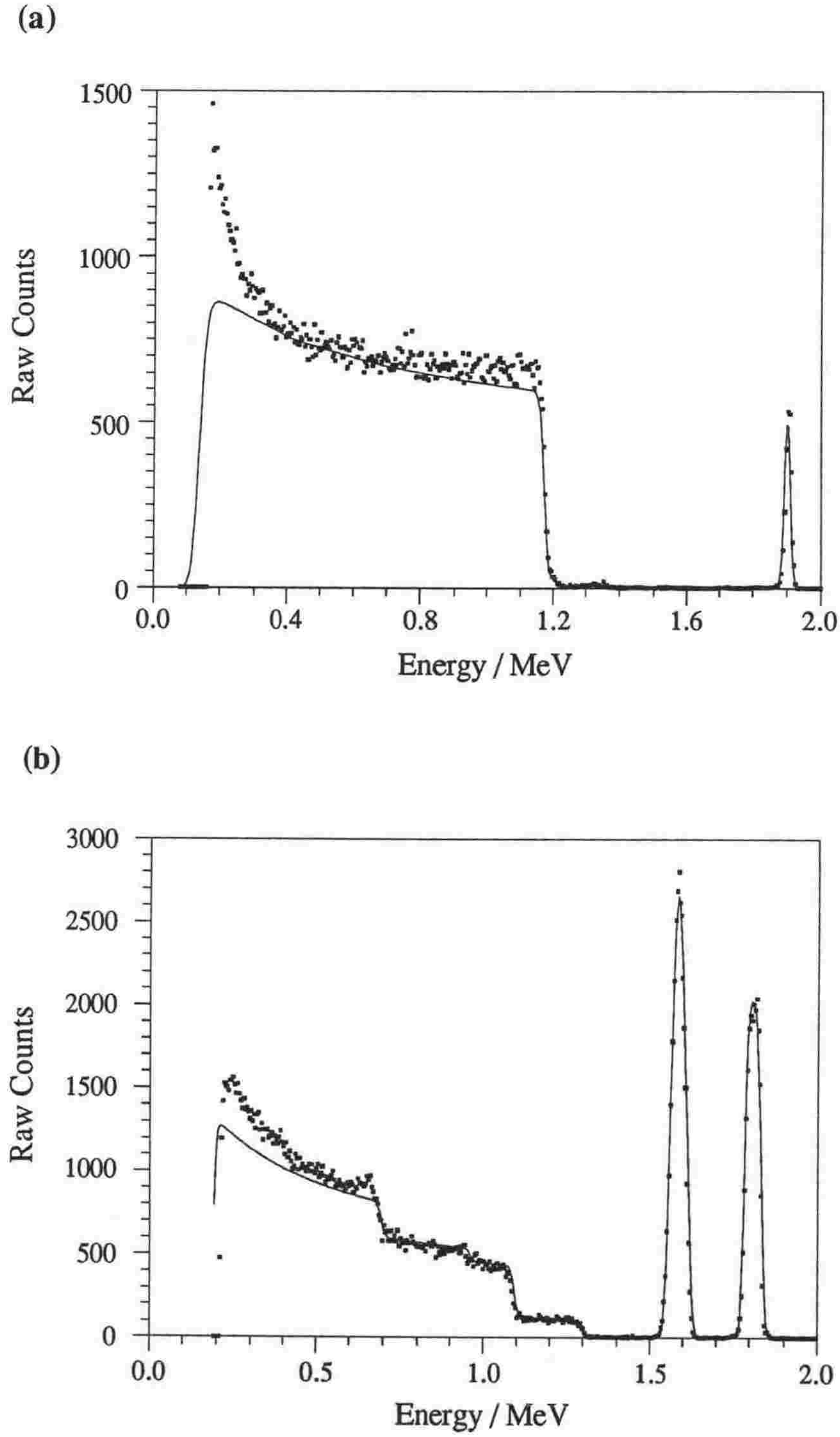

Figure 3.1 Rutherford backscattering spectrum for (a) Bi implanted Si wafer standard and (b) sample 37/1G1 and simulation of 323×10^{15} atoms·cm^{-2} of $TaGe_7$ and 0.01mm of $SiCa_{0.2}Na_{0.4}O_3$. Experimental points shown as small squares and rump simulation as solid line. Simulation parameters are $\Omega = 0.40$msr, detector resolution FWHM 20keV, and straggling factor 1 (i.e. Bohr straggling).

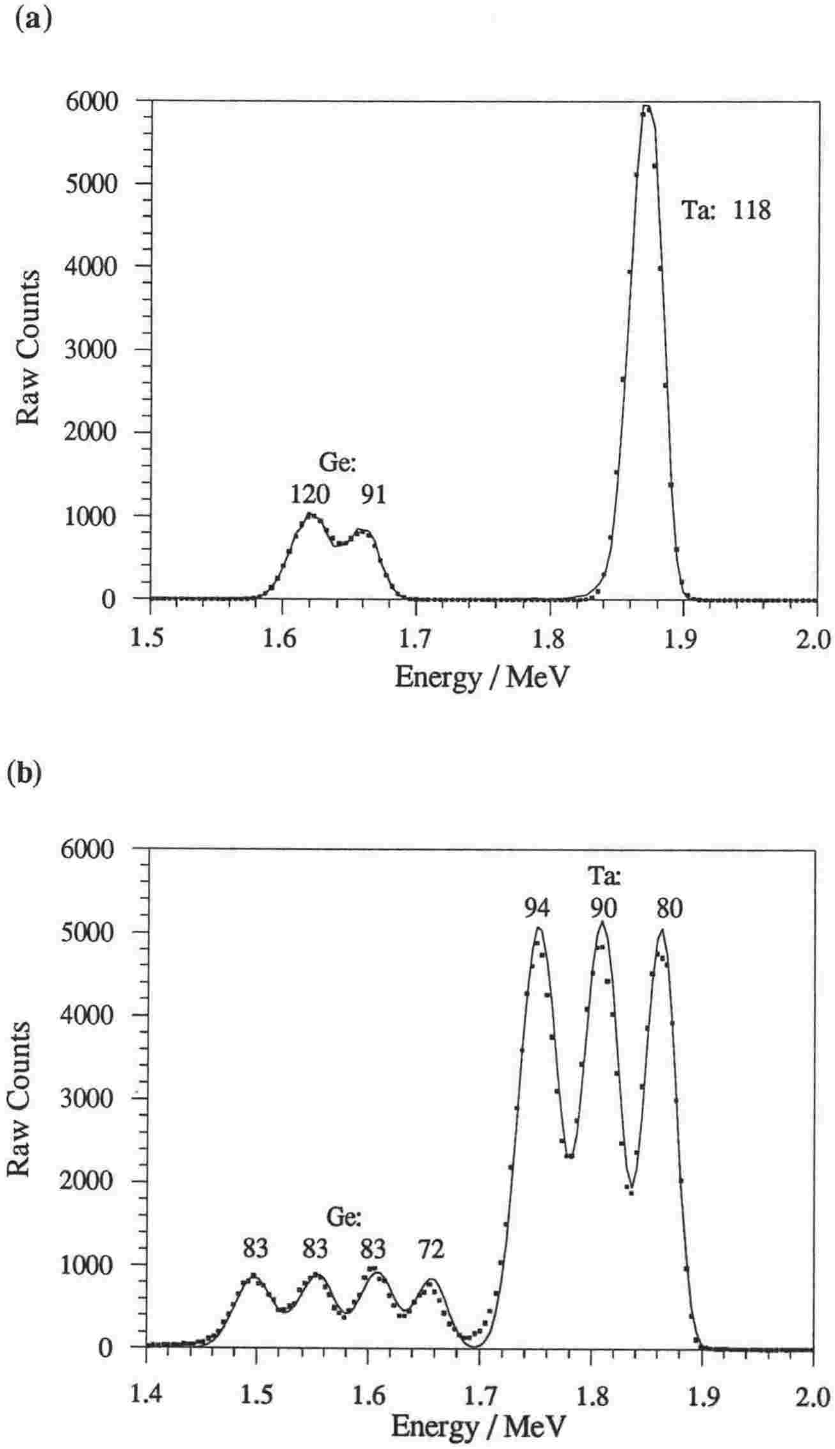

Figure 3.2 Rutherford backscattering spectrum for (a) sample 34/1G1 and three layer simulation Ge--Ta-Ge (thicknesses as shown in atoms·cm^{-2}) and (b) sample 18/3G4 tilted at 45° to incident beam and seven layer simulation Ge-Ta-Ge-Ta-Ge-Ta-Ge (thicknesses as shown in atoms·cm^{-2}). Experimental points shown as small squares and RUMP simulations as solid line. Simulation parameters are $\Omega = 0.40$ msr, detector resolution FWHM 20keV, and straggling factor 1 (i.e. Bohr straggling).

determining the number of atoms per unit area per layer of the multilayers. Because the RBS measurements are more direct, and in most cases more precise than the MBI measurements, layer thicknesses will be quoted in terms of atoms per unit area.[9]

3.3 Transmission Electron Microscopy

3.3.1 Specimen Preparation

Specimens were prepared for viewing in the electron microscope from multilayers deposited onto mylar substrates. A thin strip about 0.2mm wide was cut from the sample and embedded in resin. Cross-sections of the multilayers, 50-70Å thick, were microtomed[10] from the resin block using a diamond knife. Care was taken to cut the sections perpendicular to the layering plane to ensure that later TEM measurements of the total thickness of the multilayer were accurate. Knife damage to the multilayers was minimised by sectioning through the layers rather than along the layers (see Figure 3.3). Sectioning along the layers caused the sample to break into small lengths and curl. Buckling within these lengths was also troublesome. A micrograph of a specimen prepared in this manner is shown in Figure 3.4. All other specimens referred to in this section were microtomed with the knife cut made through the layers. After microtoming, the sections were collected on copper grids or carbon coated copper grids.

3.3.2 Electron Microscopy

Specimens were examined in a Philips[11] 420 transmission electron microscope using an accelerating voltage of 100keV. The use of lower beam energies was precluded since this would require thinner sections which are more prone to distortion and tearing during the sectioning process. The specimens were imaged both in bright field and diffraction mode.

---

[9] Areal densities may be converted to approximate layer thicknesses using $\rho_m(\text{Ta}) \approx 0.46\text{x}10^{23}$ ~~s(23)~~ atoms·cm^{-3} and $\rho_m(\text{Ge}) \approx 0.43\text{x}10^{23}$ atoms·cm^{-3}.

[10] Sectioning was done on an Ultracut E microtome, Reichert-Jung, Vienna, Austria.

[11] Philips, Electronic Instruments Co., USA.

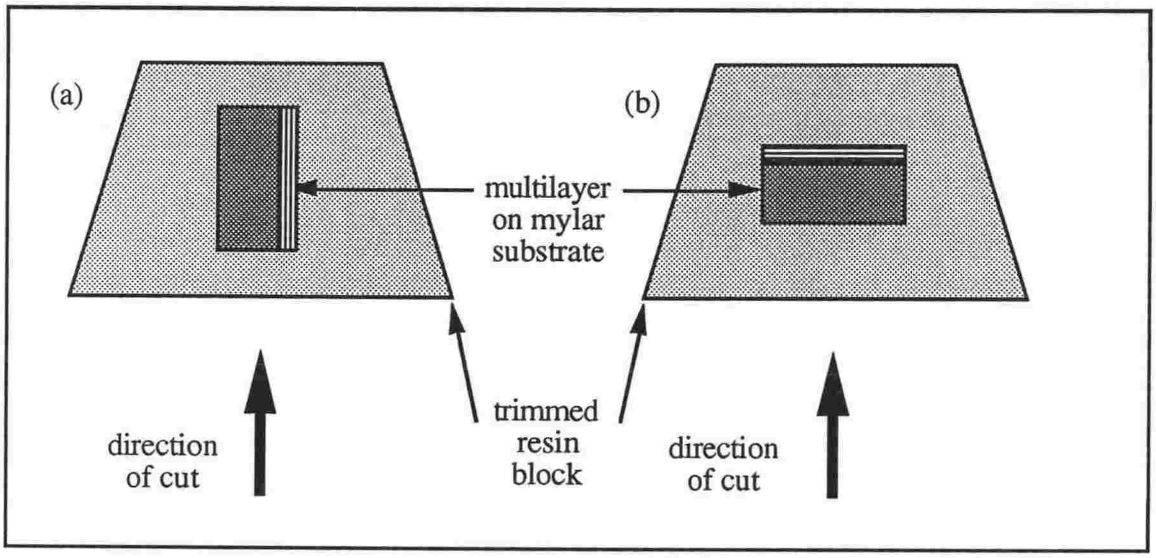

Figure 3.3 Microtome sectioning of multilayer embedded in resin block. Knife cut made (a) along the layers and (b) across the layers.

3.3.3 Results

Cross-sections of multilayers from every evaporation were examined. Typical micrographs are shown in Figures 3.5-3.7.

Morphology

TEM confirmed the number of layers and identified layering faults in some early samples (see Figure 3.8 for example). The layers were continuous over the length of the section (typically of the order of 0.2mm) with no evidence of island formation in Ta layers as thin as ~15Å. Moreover no significant variation in the layer period, either along the length of the section or across the multilayer, was observed.

The interfaces were reasonably uniform although some small scale roughness was evident in most cases. (This is in addition to the larger scale 'rippling' or 'buckling' caused by knife damage.) In cases where the small scale roughness is more pronounced in thinner areas of the section the small scale roughness is also attributed to knife damage (see Figure 3.9(a)). However, where the total thickness of a multilayer exceeds ~1000Å, layers further from the substrate are clearly less uniform (see Figure 3.9(b)). This would be the case if the small scale irregularities were formed during film growth. (For a discussion of the growth of amorphous films see Tang et al., 1990). In most cases the cause of the observed small scale roughness is not so obvious although it is thought to be a combination of both inherent roughness and knife damage.

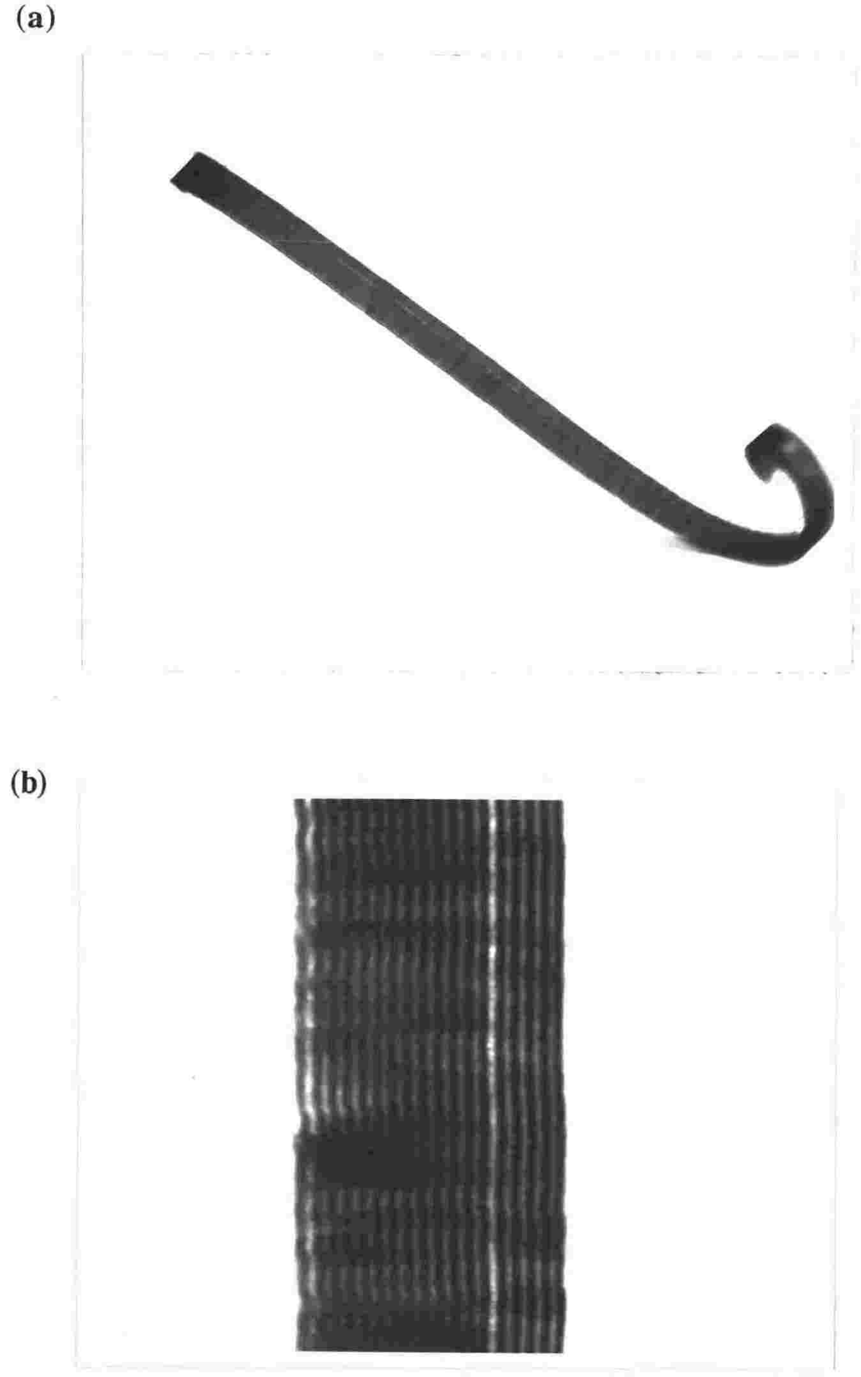

Figure 3.4 TEM bright field images of a multilayer that was sectioned by microtoming along the direction of the layers at magnifications of (a) x 30 000 and (b) x 210 000. Sections prepared in this manner have a tendency to break into short lengths and curl. Note the buckling that is evident even in the straight part of the section.

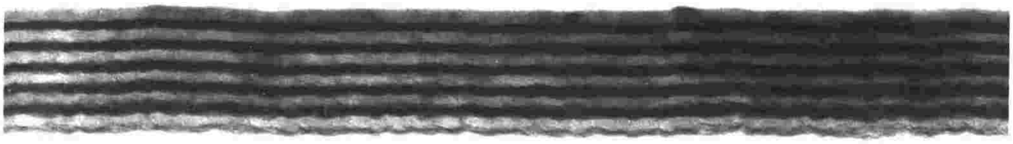

Figure 3.5 TEM bright field image of sample 16/3M3 at a magnification of x 210 000. Dark layers are Ta.

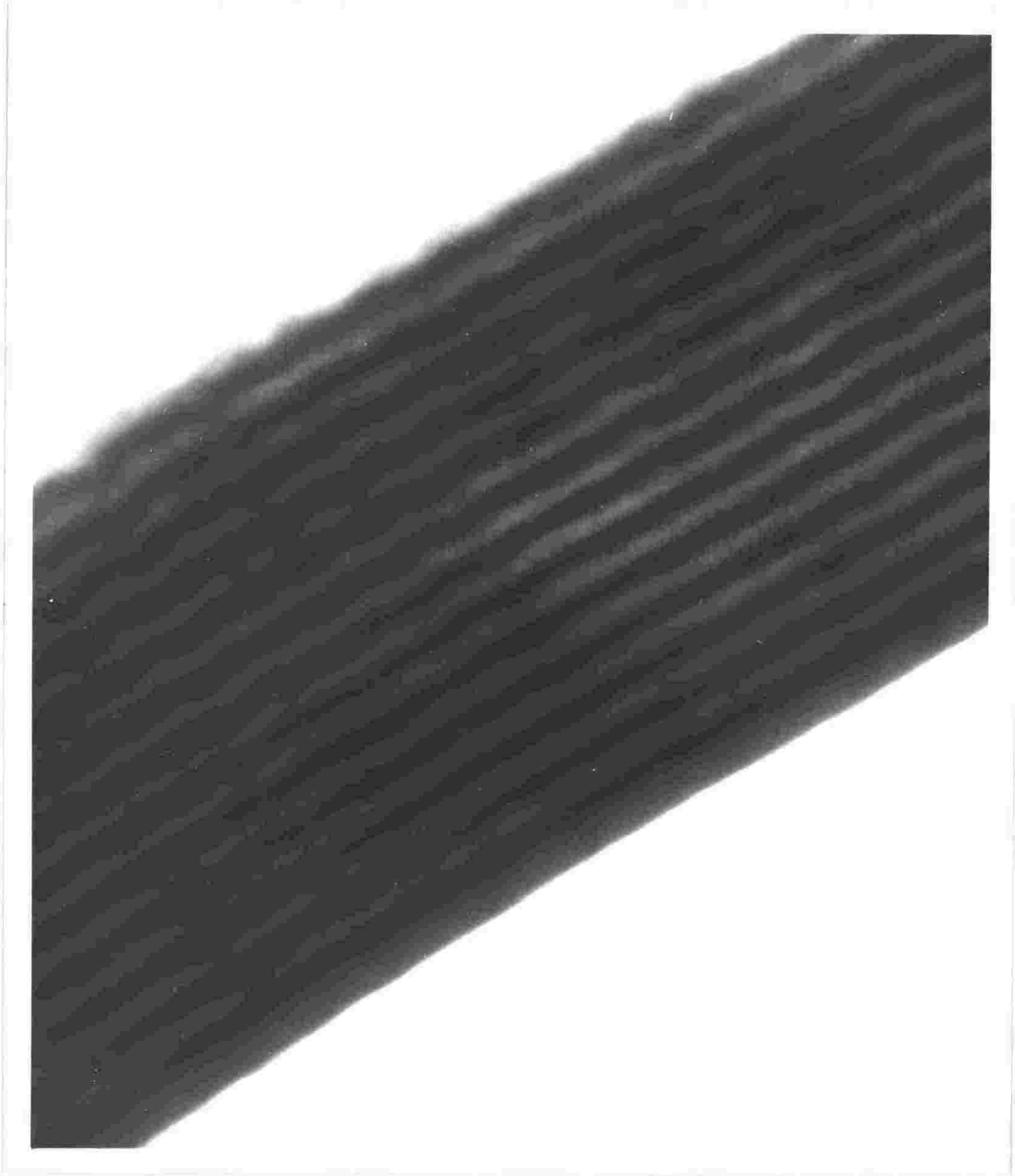

Figure 3.6 TEM bright field images of sample 32/2M2 at a magnification of x 600 000. Dark layers are Ta.

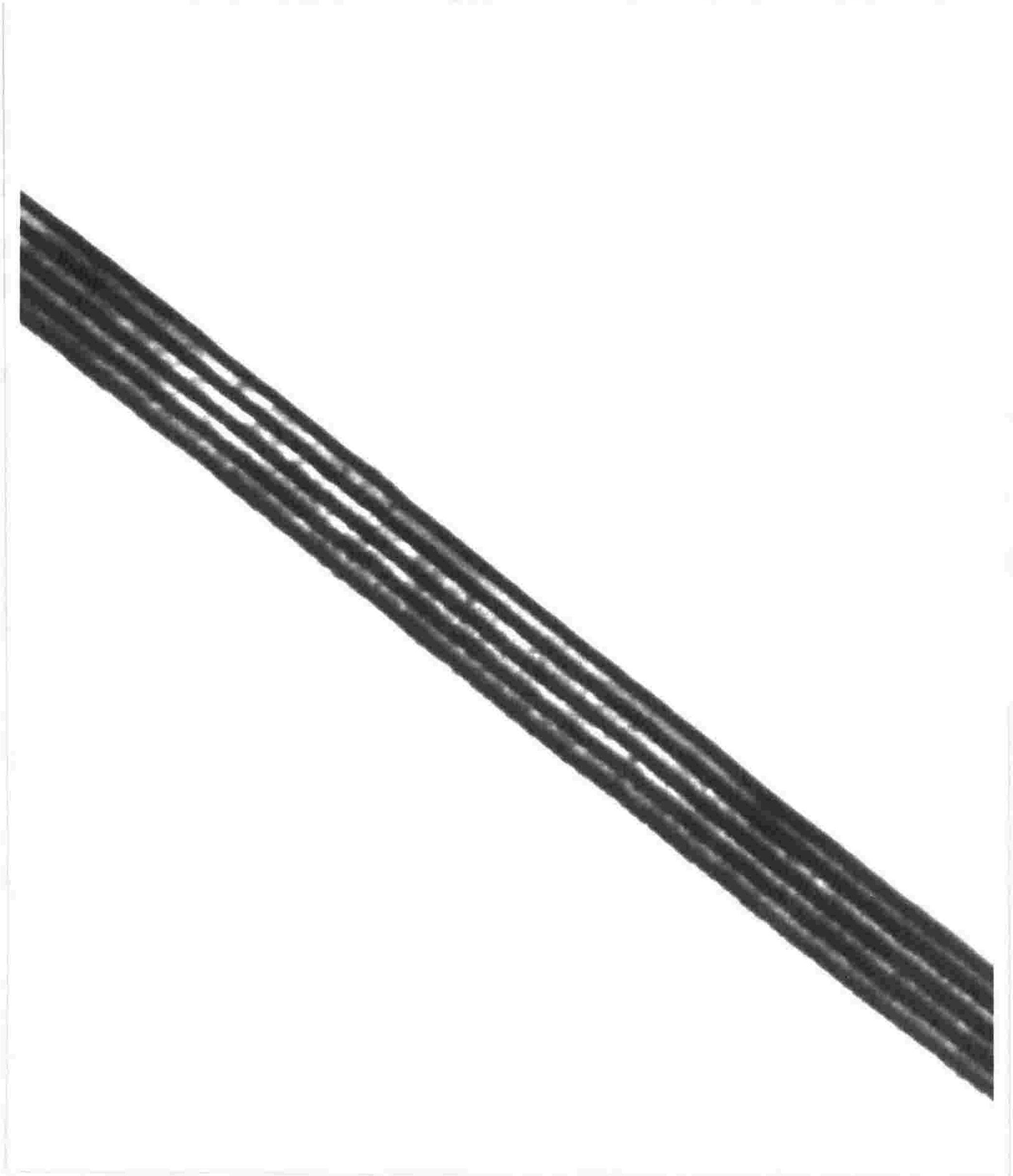

Figure 3.7 TEM bright field images of sample 30/3M6 at a magnification of x 135 000. Dark layers are Ta. Note the structure in the Ge layers caused by electron beam heating.

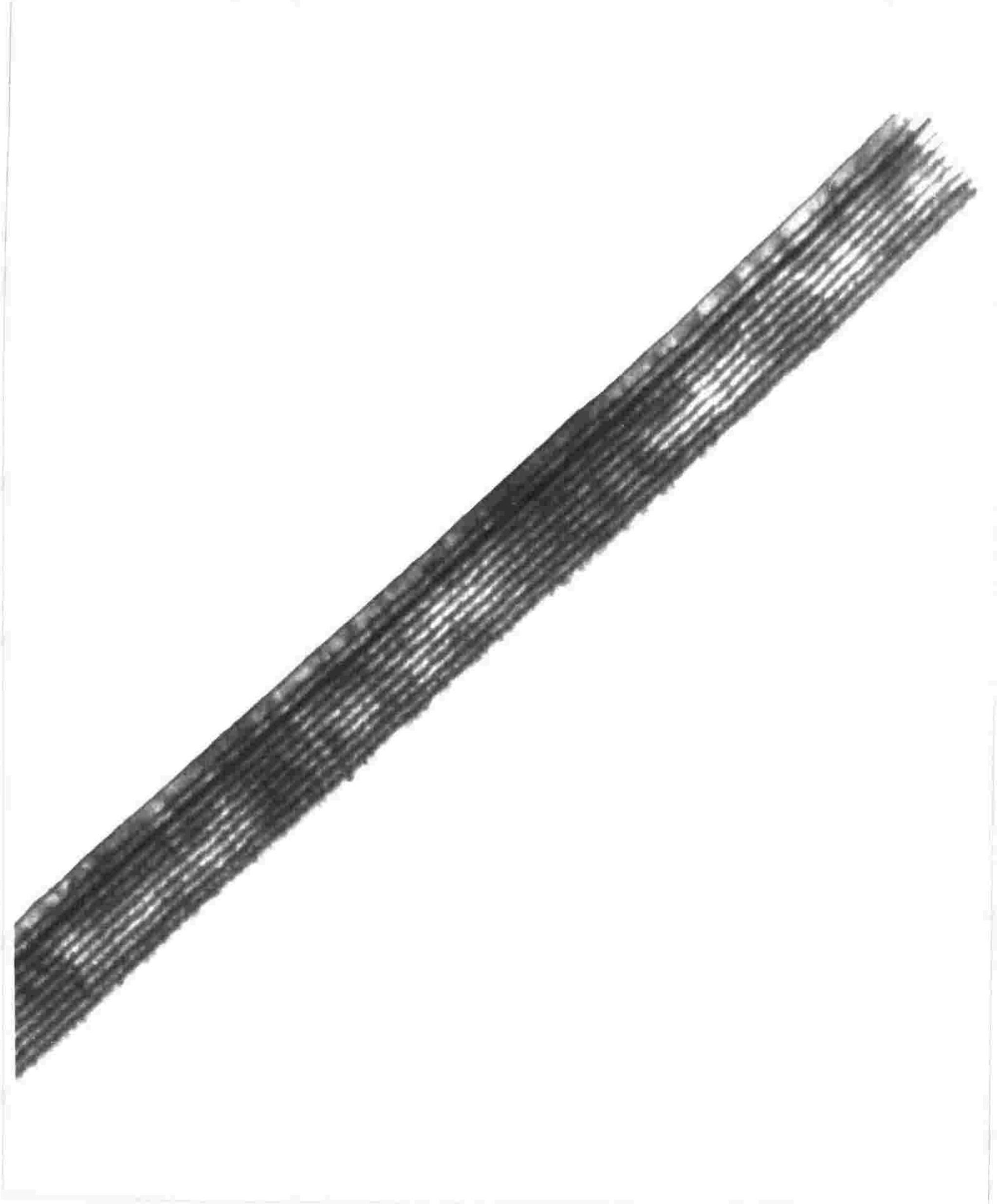

Figure 3.8 TEM bright field images of sample 20/3M6 at a magnification of x 95.000. Dark layers are Ta. Note the layering fault.

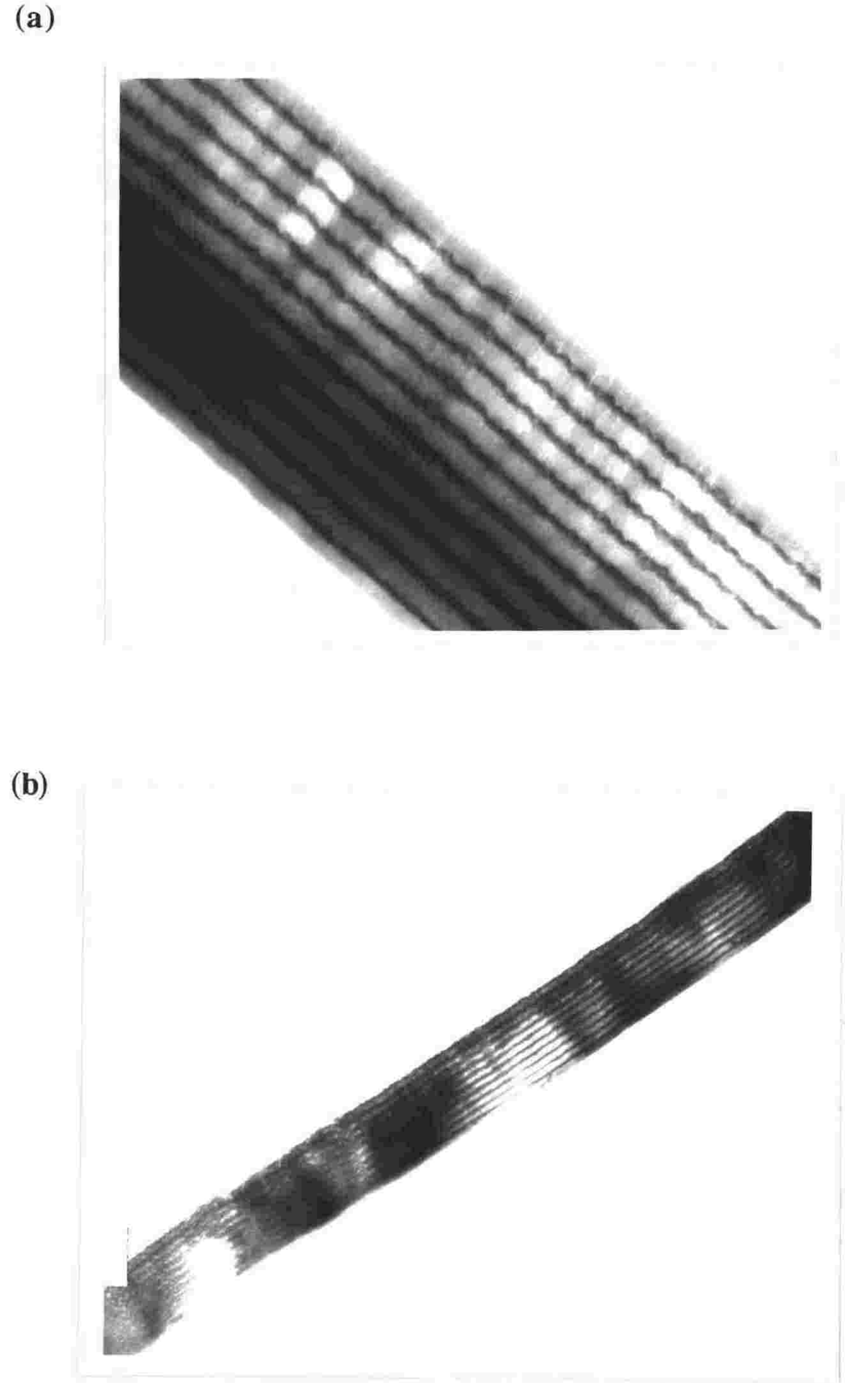

Figure 3.9 TEM bright field images showing small scale non-uniformity. (a) Sample 29/3M2 at a magnification of x 166 000. Layers closer to the substrate are more uniform. (b) Sample 28/3M5 at a magnification of x 57 500. Layers appear more uniform in thicker areas of the section. Dark layers in each case are Ta.

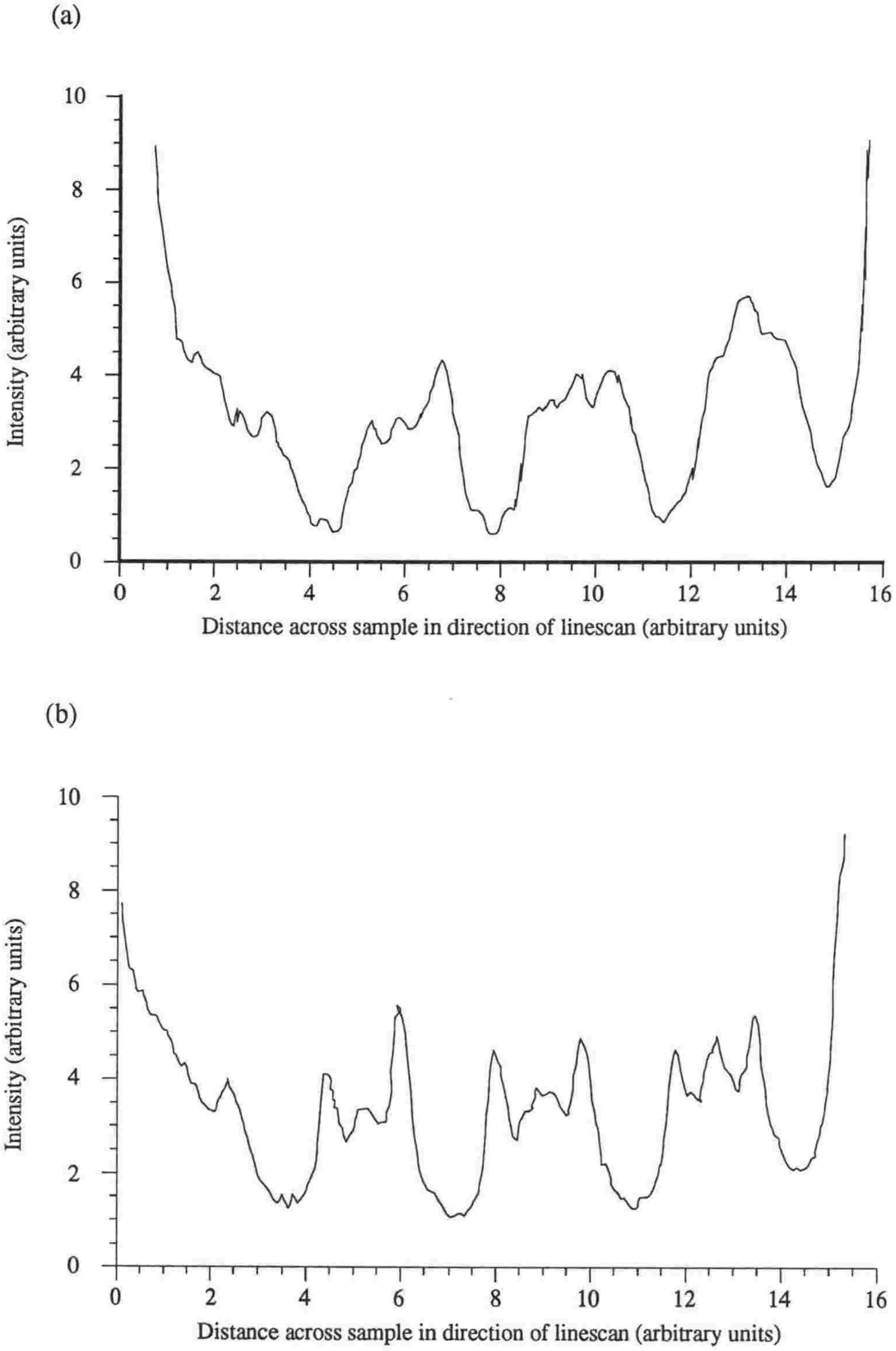

Figure 3.10 Variation in intensity across a multilayer showing Fresnel fringes for two different values of defocus: (a)Δf = -8000Å (b)Δf = -4000Å. The image was digitised using a Molecular Dynamics computing densitometer and the linescan taken with Molecular Dynamics ImageQuant Software v3.0.

Layer Thicknesses

The apparent thickness of the layers in an electron micrograph cannot be directly related to the true layer thickness. A full explanation in terms of imaging theory will not be given here but broadly speaking, Ta scatters electrons more strongly than Ge with the result that in the image, the Ta layers appear broadened at the expense of the Ge layers. The layering period deduced from electron micrographs however represents the true period to a good approximation. Measurements of the layering period deduced from micrographs agreed within experimental uncertainty with the MBI measurements made on the "bulk" films.

Structure

The structure of the Ta and the Ge layers was investigated in diffraction mode. Even for the thickest layers, diffraction spots indicating the presence of crystalline order were not seen. Both the embedding resin and the mylar substrate give rise to diffuse ring diffraction patterns that obscure any diffuse diffraction rings from amorphous Ta or Ge that may be present. This is the case even in selected area diffraction since the smallest diffraction aperture illuminates an area of diameter 1μm at the sample - a much larger area than that occupied by the width of the multilayer (typically 0.1-0.2μm). Excessive beam heating of the specimen caused an alteration in the character of the Ge layers, with bright patches and blobs such as those in Figure 3.7 developing in bright field images. Although no change in the diffraction pattern was seen, the appearance of bright patches could be due to the onset of crystallisation. (Amorphous Ge is known to crystallise under electron bombardment - see for example Buckley, 1979).

Boundary Diffuseness

Light passing though a restriction or aperture forms a Fresnel diffraction pattern on a nearby screen. An electron beam behaves in the same manner, and indeed in TEM work Fresnel fringes formed at a sharp edge are often used as a focussing aid. A sharp boundary between two materials of different scattering powers, such as the interfaces of a multilayer, will also produce Fresnel contrast when illuminated by an electron beam. Ness et al.,1986 and Ross & Stobbs, 1991, have developed a method of estimating the amount of intermixing at layer boundaries from the Fresnel contrast seen in a through-focal series of micrographs. The technique involves refining a computer simulation based on the continuum multislice model[12] until it matches the intensity profile seen experimentally. This allows the interface diffuseness, the layer width and the composition profile to be estimated with close to atomic resolution in the systems they have studied.

---

[12] See for example Self & O'Keefe, 1988.

The application of this method to Ta/Ge multilayers was investigated. Although it proved possible to prepare samples showing good Fresnel fringe visibility, such samples could not be prepared routinely, the most common problem being interface distortion during sectioning. Intensity profiles taken from a through-focal series of micrographs are shown in Figure 3.10. The large difference in scattering powers of Ta and Ge and the increase in elastic scattering due to the disordered nature of the layers means that the usual continuum multislice model is a poor approximation in the case of Ta/Ge multilayers. Due to the complexity of the problem both experimentally and theoretically the application of this technique to Ta/Ge multilayers was not pursued.

3.3.4 Conclusion

Transmission Electron Microscopy of cross-sections of the multilayers confirmed the number of layers and the layering period. The layers appear uniform with sharp interfaces although the top layers of very thick multilayers are slightly distorted. Although it proved impossible to collect direct structural evidence it is very unlikely that either the Ta or Ge layers are crystalline.

Chapter Four

Resistance Measurement

This chapter describes the techniques used to measure the in-plane DC resistance of the multilayers from room temperature down to liquid helium temperatures. The sample resistance was typically of the order of several hundred ohms with a fractional change in the resistance as a function of temperature of the order of 200ppm per kelvin. The very small changes in resistance as a function of temperature demanded careful measurement to attain sufficient precision (roughly 1 part in 10^5). A four-point probe method was used to eliminate what would otherwise be significant lead and contact resistance errors. In addition, thermal gradients were minimised by allowing the samples to warm to room temperature over a period of several days, as even small thermal gradients between sample and thermometer cannot be tolerated. The resistance measurements were performed in a helium bath cryostat using an insert designed for this project. In the following sections, the design of the cryostat insert is described as well as the method of attaching contacts to the samples, the measurement of the resistance and the temperature, the computer program written to collect the data, and the experimental techniques used.

4.1 Cryostat Insert Design

A cryostat insert was designed for resistance measurements in the temperature range 1.3 - 300K. The main features of the insert are shown in Figures 4.1 and 4.2. The sample block, including a heater mount and a cavity for the thermometer, was machined from a single piece of copper. The sample block can accommodate three samples, 18mm in diameter. Copper shields are mounted around the sample block to minimise radiation losses. The sample block and shields are contained within a stainless steel vacuum can. Thermal isolation of the samples from the liquid nitrogen or liquid helium bath is achieved by using thin wall stainless steel tubing to connect the sample block to the vacuum can. The vacuum can is connected to the top flange by a thin wall stainless steel pumping tube. The design permitted the insert to be used in either a stainless steel or a glass dewar.

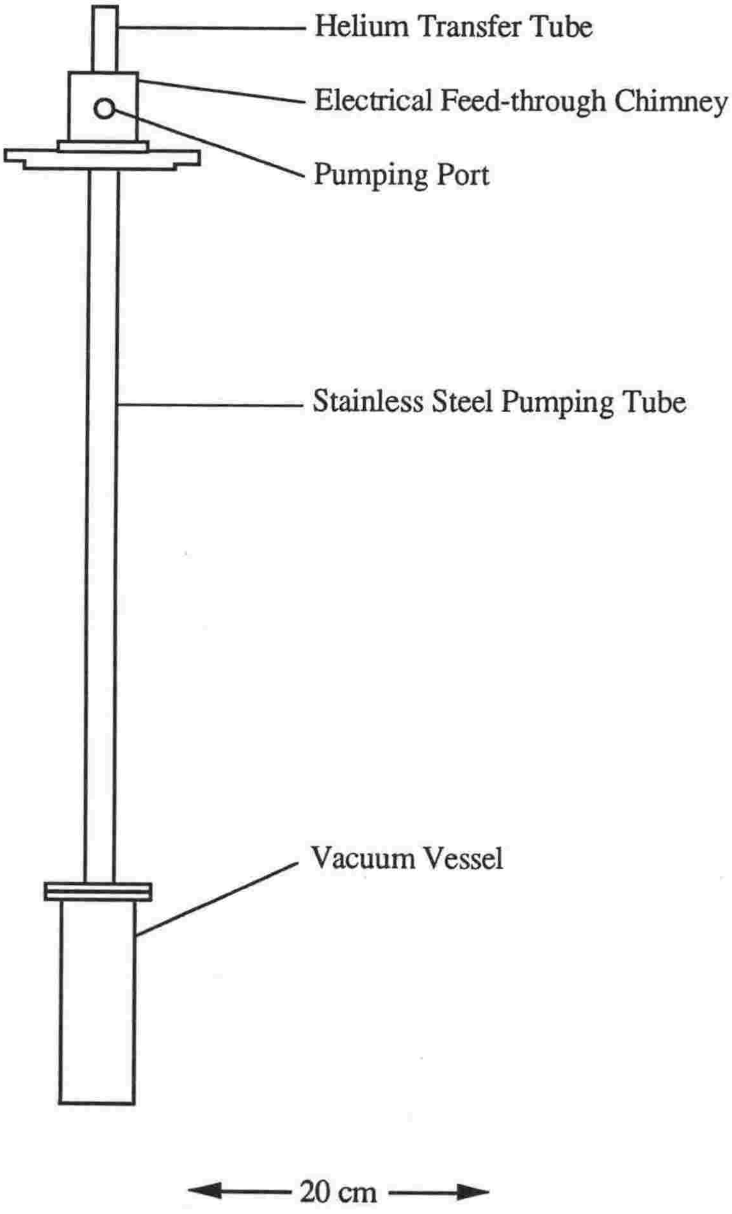
Helium Transfer Tube
Electrical Feed-through Chimney
Pumping Port
Stainless Steel Pumping Tube
Vacuum Vessel
20 cm

Figure 4.1 Cryostat insert (to scale).

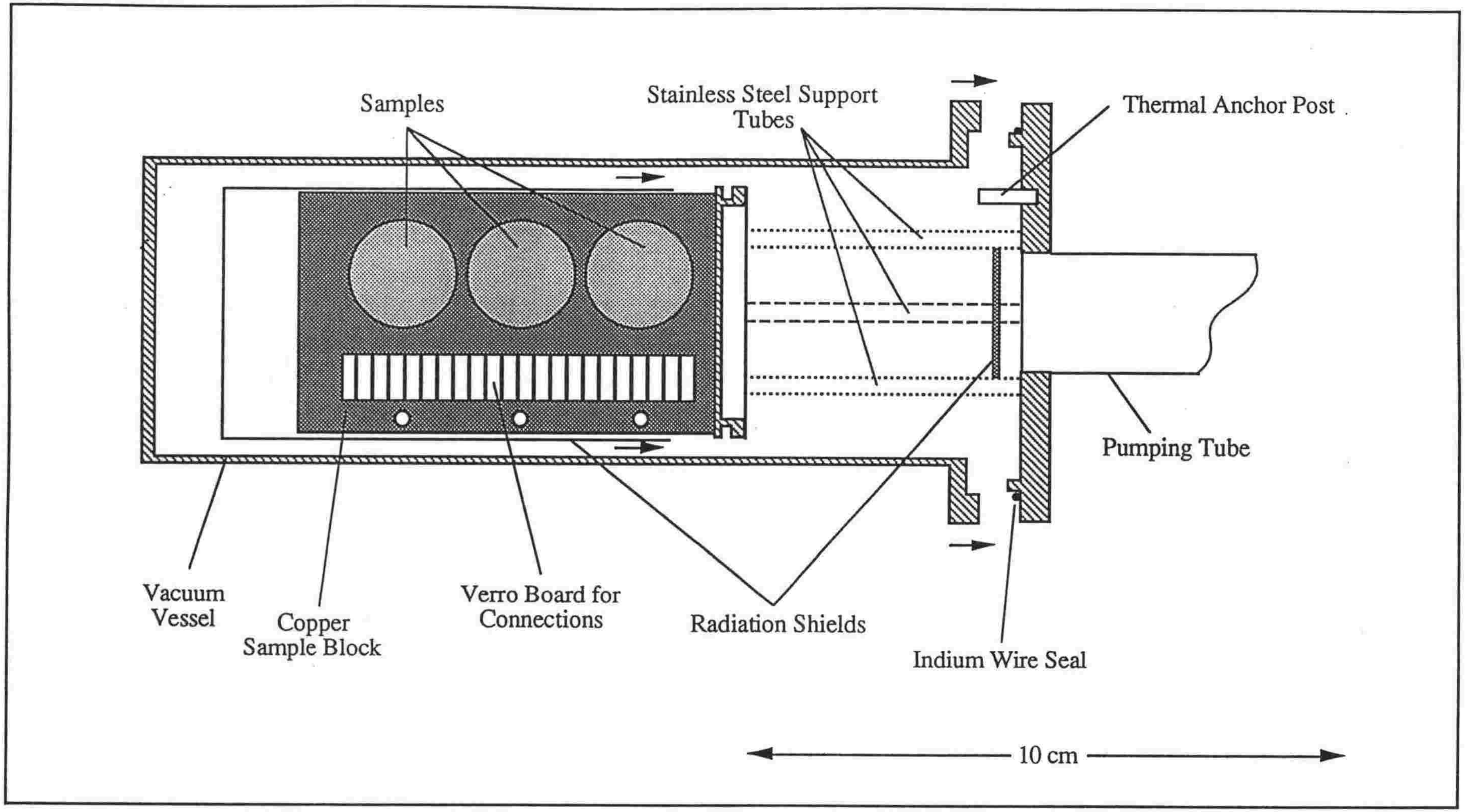
Samples
Stainless Steel Support Tubes
Thermal Anchor Post
Pumping Tube
Vacuum Vessel
Copper Sample Block
Verro Board for Connections
Radiation Shields
Indium Wire Seal
10 cm

Figure 4.2 Exploded view of lower portion of cryostat insert.

Constantan wires of diameter 0.132mm are used as leads for sample resistance measurements. Owing to the small measuring currents used, resistive heating of the leads is negligible, while the low thermal conductivity of constantan reduces the heat flow into the sample area from the top of the cryostat. The wires are connected to a glass feed-through at the top of the insert and fed down through the pumping tube, around heat sinks in the vacuum can and the sample block, to a verro board connector on the sample block.

The heater was wound non-magnetically with ~9m of 0.132mm diameter constantan wire. The heater leads are heat sunk separately from the measurement leads.

4.2 Temperature Measurement

The temperature is measured with a 20Ω rhodium-0.5% iron resistance thermometer[1] calibrated by Cryogenic Calibrations Ltd. (calibration number 18417) against standard resistance thermometers whose own calibrations are accurate to within ±3mK up to 30K and ±5mK above 30K.[2] To simplify data analysis the thermometer calibration is expressed as a function of the resistance of the thermometer. The fit approximates the calibration to within ±3mK below 27K, ±5mK from 27K to 100K and ±7mK from 100K to 273K . Details are given in Appendix I.

A Keithley 580 micro-ohmmeter is used to make a four terminal measurement of the thermometer resistance. The resolution of the micro-ohmmeter (10μΩ on the 2Ω range and 1mΩ on the 20Ω range) introduces a maximum uncertainty in the temperature measurement of 5mK. The overall accuracy of the temperature measurement (assuming thermal equilibrium between sample and thermometer) is 15mK.[3] Slightly better accuracy (~10mK) is achieved below 30K and above 100K.

The thermometer is used to measure temperatures below the lowest calibration point of 1.485K and above the highest temperature in the reference scale by extrapolating the calculated calibration curve. Although absolute temperature values below 1.485K and above 273K are not necessarily reliable, the extrapolation is useful for making comparisons between samples.

---

[1] H. Tinsley and Co. Ltd.

[2] Standard thermometers used by Cryogenic Calibrations Ltd. have been calibrated at the National Physics Laboratory, U.K. against EPT-76 below 30K and IPTS-68 above 30K.

[3] The thermometer is mounted on the underside of the copper sample block of the cryostat insert, beneath the samples (see Figure 4.2).

4.3 Resistance Measurement

The resistance of the multilayers is measured using samples deposited on glass substrates. A network for a four-point probe resistance measurement is scribed through the entire thickness of the film with scribing lines of the order of 0.2mm wide. The rectangular area of the film over which the resistance is measured is approximately 2mm x 6mm . Provided the scribing is done carefully, the uncertainty in the dimensions of the rectangular section of the film (measured accurately with a travelling microscope) contribute less than 5% uncertainty to the final measurement of the sheet resistance of the sample.[4] Before making contacts to the samples, a small hole is scratched through the film to ensure that conduction occurs purely in the plane of the layers. (If the contacts were to be placed directly on the surface of the film, the current would have to first flow down through the layers). Figure 4.3(a) shows the scribing lines together with the positions of the contacts.

Contacts to the film are made using fine copper wire 80µm in diameter, tinned with a lead/tin solder, and attached to the film with indium. Initially the indium contacts were soldered to the film using low soldering temperatures to minimise thermal damage to the sample. These contacts were generally reliable but occasionally fell off at low temperatures. Better contacts could be made by soldering a small blob of indium to the copper wire and then gently pressing the ~~induim~~ indium onto the sample.

The circuit used to measure the DC resistance of the samples is shown in Figure 4.3(b). Three separate meters measure the potential difference across each sample, V_1, V_2, and V_3. The current I through the samples is determined from a measurement of the potential difference V_{std} across a standard resistor R_{std} in series with the samples. Thus the resistance R_1 of sample 1 is given by $R_1 = R_{\mathrm{std}} \cdot V_1 / V_{\mathrm{std}}$ and similarly for samples 2 and 3.

The standard resistor was a 100Ω commercial metal film resistor with a quoted temperature coefficient of resistance of 15ppm·K^{-1}. Direct measurements suggest a lower value of 5ppm·K^{-1} at room temperature. Although the standard resistor was protected from rapid thermal fluctuations by embedding it in expanded polystyrene of low thermal conductivity[5] its temperature changed slowly in response to the variation in room temperature over a 24 hour period. The room temperature varied between about 24°C

---

[4] Note that the contribution of 5% uncertainty to the *sheet resistance* of the film from the dimensions of the sample does not compromise the requirement that the *resistance* be measured with a precision of at least 1 part in 10^5.

[5] Endurathane 3245, Polymer Development New Zealand Ltd.

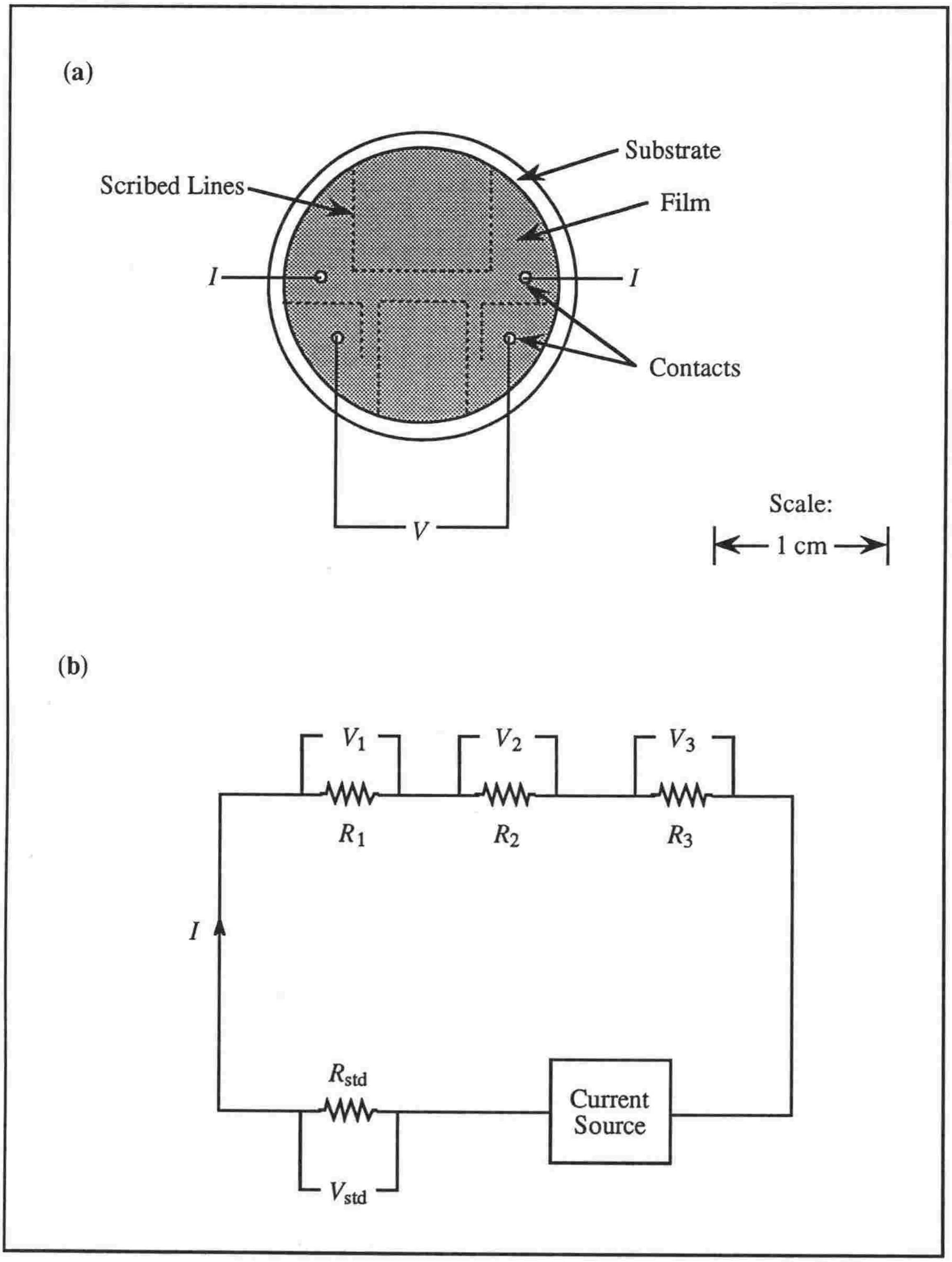
(a)
Substrate
Scribed Lines
Film
I
I
Contacts
V
Scale:
1 cm
(b)
V_1
V_2
V_3
R_1
R_2
R_3
I
R_{std}
Current Source
V_{std}

Figure 4.3 (a) Diagram of sample showing scribing lines, and contact positions for the input of the current I and measurement of the voltage V and (b) circuit for measuring the resistance R_1, R_2 and R_3 of samples 1, 2 and 3 using a standard resistor R_{std} .

mid-afternoon down to about 20°C around midnight causing the resistance of the standard resistor to change by ~20ppm.

A Keithley[6] 197A auto-ranging microvolt DMM with $5^1/2$ digit resolution was used to measure V_{std}. V_1 was measured with a Keithley 195A digital multimeter with $5^1/2$ digit resolution, V_2 with a Keithley 181 digital nanovoltmeter also with $5^1/2$ digit resolution and V_3 with a Keithley 196 system DMM with $6^1/2$ digit resolution. Absolute values of the sample resistance therefore had an uncertainty of less than 75ppm (5ppm from V_{std}, 20ppm from R_{std} and less than 50ppm from the measurement of the potential difference across the sample).

A direct current of 100μA is used for all samples. Self-heating of the sample is negligible at this current even at low temperatures. Measurements were taken with the current in the forward and reverse directions to eliminate thermal offsets in the voltage.

4.4 Computer Program

A computer program was written to control the current to the samples, collect readings from the meters, calculate and display the temperature and the resistance of each sample and save the results to disk for later analysis. The program was written using *ASYST*[7] software for an IBM compatible PC.

To fully automate the collection of data, the current through the samples needed to be controlled from within the computer program. A simple circuit connected to the printer port of the computer and fed by a constant current source allowed a signal generated within the program to reverse the direction of the current and to turn the current on and off. Details of the controller circuit are given in Appendix II.

The program is menu driven. The data acquisition menu or the plotting menu may be chosen from the main menu. From the plotting menu, previously stored data can be retrieved from disk and plotted either to the screen or printer. The data acquisition menu launches the data collection routines of which four are available. The first simply displays a continuously updated measurement of the temperature and is useful for monitoring the temperature where a more time consuming measurement of the sample resistances is not required. The remaining three routines measure and store the resistance as a function of temperature either "manually", "semi-automatically" or "automatically". In the manual mode each reading must be triggered by a keyboard command and the current is switched by the user when prompted by the program. In the semi-automatic mode, readings are again triggered by a keyboard command but the current is switched automatically via the current controller. In the fully automatic mode, both the triggering of readings at set intervals, and the switching of the current, are performed by the program with no input from the user. Data presented in this thesis was collected using the automatic routine, although the other routines proved useful in preliminary measurements.

---

[6] Keithley Instruments, Inc., Cleveland, Ohio.

[7] Asyst Software Technologies, Inc., New York.

Once a routine to measure the resistance as a function of temperature is chosen, the user must enter a number of details when prompted by the program. This includes a file name for subsequent data storage, the sample names, the resistance of the standard resistor and, in the case of automatic collection, the time delay between consecutive readings. Once the program has initialised the meters, it is ready to begin collecting data. In the case of automatic collection, measurements are taken in the following manner:

1. The controller is triggered to switch the current on, in the forward direction.
2. After a two second delay to allow the current to stabilise, all meters are simultaneously triggered to take a reading.
3. The program interrogates each meter sequentially for this reading and stores the results.
4. The controller is triggered to reverse the direction of the current.
5. Steps 2 & 3 are repeated.
6. The controller is triggered to switch the current off.
7. The temperature is calculated (as outlined in Appendix I) from the average of the two measurements of the resistance of the thermometer. (Note that the temperature is changed only very slowly so that the difference in the two measurements is negligible).
8. The voltage across the standard resistor and each of the samples is taken as $(V_+ - V_-)/2$ so as to eliminate thermal offsets. (Here V_+ is the measured voltage with the current in the forward direction and V_- is the voltage with the current in the opposite direction.)
9. The resistance of each of the samples is calculated as outlined in Section 4.4.
10. The temperature and the resistance of each sample is displayed on the monitor and stored to disk. (The results are stored both in binary for later plotting in the plot menu, and also as a text file for analysis in Kaleidagraph[8].)
11. The program waits the specified delay time. The delay time may be changed during program execution. The maximum reading rate (that is, delay time set to zero) is

---

[8] Kaleidagraph, Synergy Software, Reading, PA.

four readings per minute.

12. Steps 1.-11. are repeated until interrupted by the user.

In the semi-automatic and manual modes step 11 is modified so that the program waits for a keyboard command before returning to Step 1. In the manual routine, Steps 1, 4 and 6 are replaced by prompts for the user to manually switch the current.

4.5 Measurement Techniques

This section briefly describes the process of taking a measurement of the sample resistance as a function of temperature.

Three samples are secured in the sample block of the cryostat with nail polish. The nail polish provides good thermal contact without creating an electrical path from the samples to the block. The vacuum can is sealed with 1mm diameter indium wire. A reliable seal can be made repeatedly with the same piece of wire. The sample space is evacuated to below 10^{-5} Torr and then back-filled with helium to act as an exchange gas, thermally connecting the samples to the bath. Liquid nitrogen is used to pre-cool the system to about 80K at which point liquid helium is transferred cooling the samples to ~4.2K. The temperature is lowered below 4.2K by pumping on the helium bath. The pumping speed is chosen so as to lower the temperature at a rate of ~20mK·min^{-1}. Once the lowest temperature is reached (typically 1.3 - 1.4K) the exchange gas is removed and the samples left to warm gradually. Warming rates are generally of the order of, or less than, 10mK·min^{-1} up to 25 or 30K. From 30K to 60K the samples warm rapidly. Above 60K the temperature increases at a rate of less than 100mK·min^{-1}. The samples reach room temperature after two to three days. Measurements are taken during pre-cooling, pumping, and warming. Where two sets of data are taken for the same temperature range, the data collected at the slowest heating rate are presented.

4.6 Sample Ageing

An important question is whether sample ageing is significant. Three ageing processes are possible;

- slow diffusion of gases (particularly oxygen) into the layers from the atmosphere or the substrate,
- migration of Ge atoms into the Ta layers (and vice versa) with the associated possibility of alloy formation at the interfaces and

- strain relaxation in the Ta layers.

If the effect of each of these processes is to merely change the magnitude of the resistivity of the Ta layers slightly, then the length of time which elapses between sample fabrication and the resistance measurement is unimportant in terms of the interpretation of the data. It is conceivable however that sample ageing changes the characteristics of electron conduction.

To investigate the effect of sample ageing the resistance of two samples was measured soon after fabrication and then again, six months later.[9] The room temperature sheet resistance increased by 7% for sample 23/2G2 and 0.3% for 23/3G2 while the superconducting transition temperature moved to lower temperatures by ~0.1K (see Figure 4.4). The main ageing mechanism is therefore most likely to be the diffusion of impurities into the Ta layers, since strain relaxation within the Ta layers would decrease the resistivity while alloy formation is most likely to increase the superconducting transition temperature[10]. While it is clear from these results that ageing changes the purity of the Ta layers, it was found that in each case the second measurement of the resistance could be mapped directly onto the first measurement by multiplication by a constant factor (except for the superconducting region). It is therefore concluded that while sample ageing may be important in terms of the superconducting transition it does not significantly change electron conduction at higher temperatures.

---

[9] Note that when not in use all samples were stored under vacuum ($<10^{-1}$ Torr) to minimise the in-diffusion of atmospheric gases.

[10] This point will be discussed in more detail in Chapter 6.

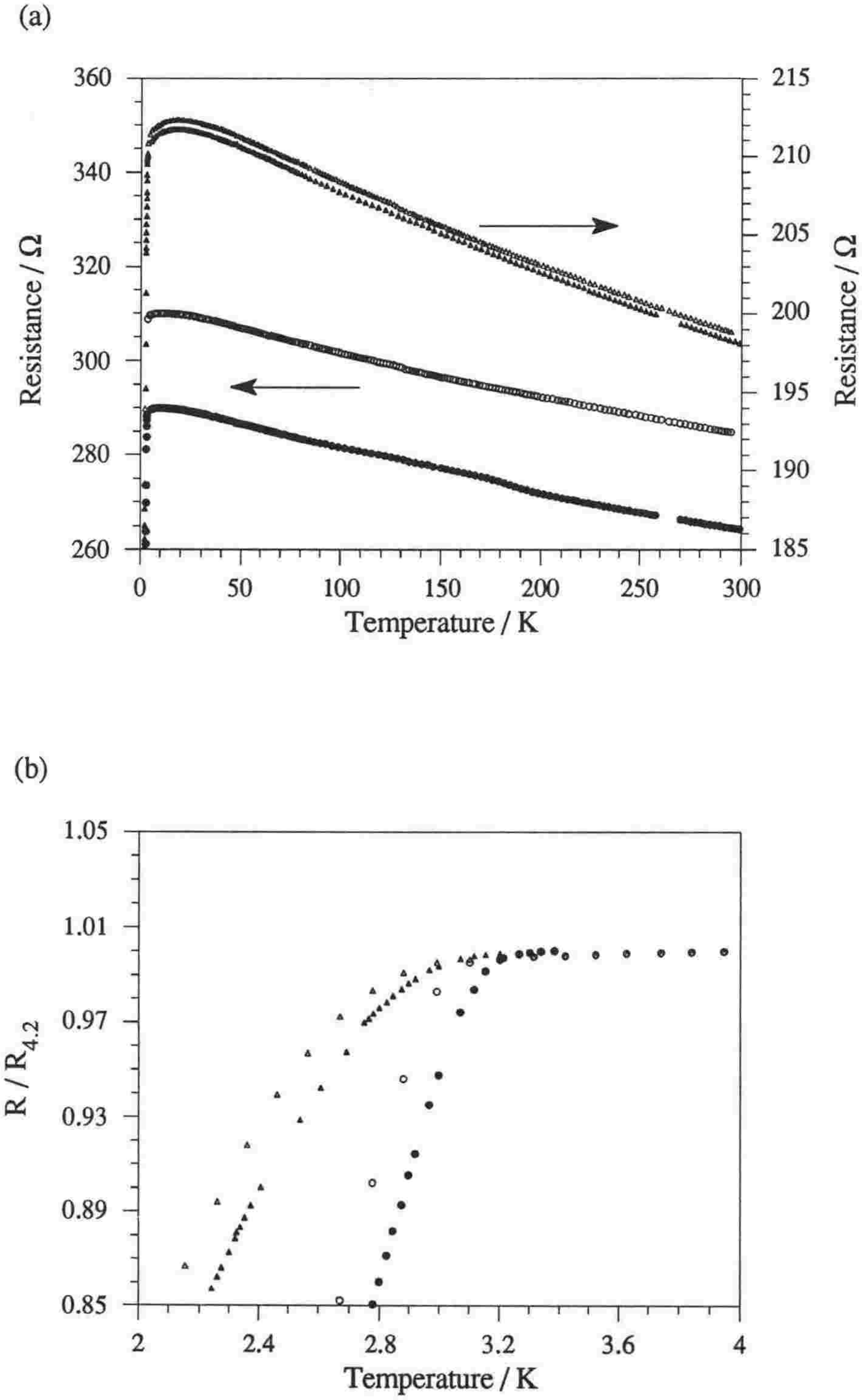

Figure 4.4 Sample ageing over a six month period. Initial measurements are shown as solid symbols and later measurements as open symbols. Triangles are sample 23/3G2 and circles are sample 23/2G2. (a) After six months the magnitude of the resistance has increased but the form of the resistance is unchanged above the superconducting transition. (b) The superconducting transition is moved to lower temperatures (the resistance normalised to that at 4.2K is plotted in this case).

Chapter Five

Temperature Dependence of the Resistivity

In Figure 5.1 a schematic representation of the variation of the resistance with temperature for bulk crystalline Ta (bcc) is compared with that measured for a typical multilayer sample. The resistance clearly behaves quite differently in each case. The resistivity of the mulitlayer is more than an order of magnitude larger than bcc Ta, increases rather than decreases as the temperature is lowered and shows anomalous behaviour at low temperatures. In addition the superconducting transition temperature is lowered in the multilayer samples . It will be argued in Section 5.2 that the measured resistivity of the multilayers can be interpreted as that of n thin Ta films connected in parallel. The profound differences in the character of the resistivity of bcc Ta and the multilayer samples therefore occurs because the Ta in the multilayers is disordered. The first section of this chapter explains, in general terms, the physical mechanisms underlying the difference in conduction in ordered and disordered materials, while in the second section the results are presented and analysed. (Note that the superconducting transition will be discussed in Chapter Six.)

5.1 Theoretical Predictions

5.1.1 Disorder in a Classical Picture

To attempt to understand the features of the resistivity discussed above, it is useful to be able to relate a physical picture of electron scattering to the conductivity (or resistivity). In the relaxation time approximation, the conductivity is given by the Boltzmann transport equation as[1]

$$\sigma = \frac{n_e e^2 \tau}{m} \tag{5.1}$$

---

[1] See for example Kittel & Kroemer, 1980.

(a)

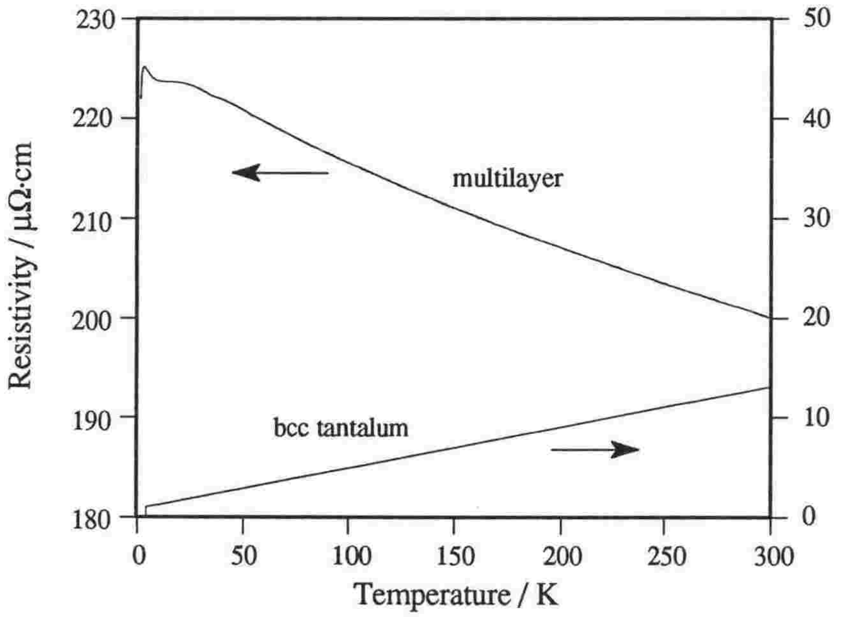

(b)

	Ta phase	
	bcc	disordered
Room temperature resistivity / µΩ·cm	13.1[2]	200
Low temperature resistivity / µΩ·cm	<1	220
TCR / ppm·K^{-1}	3600[3]	-200
T_c / K	4.39[4]	<1.4

Figure 5.1 Comparison of electrical resistance characteristics of bcc and disordered Ta (the values quoted for disordered Ta are those measured in the present study).

---

[2] Values are those quoted by Westwood & Livermore, 1970.

[3] See previous footnote.

[4] Calorimetrically determined transition temperature quoted in CRC Handbook of Chemistry and Physics, 1971.

where n_e is the number of free electrons per unit area, m is the mass of the electron and τ is the average time between successive collisions or the relaxation time. The mean free path l is related to the relaxation time by $l = \upsilon_F \tau$ where υ_F is the Fermi velocity. In this semi-classical kinetic theory, electronic collisions are treated as random, uncorrelated events - that is, it is assumed firstly that the motion of an electron emerging from a collision is not related to its motion prior to the collision, and secondly that the rate at which a given electron suffers collisions is independent of the distribution of the remaining electrons. Although there are serious objections to these assumptions[5], Equation 5.1 is convenient point to start the discussion.

If a metallic lattice could be made free from any defects, electrons would propagate through such a lattice at absolute zero without experiencing collisions - the electrons would have an infinite mean free path and the metal would have an infinite conductivity (or equivalently, zero resistivity). The finite conductivity of real metals at absolute zero is due to deviations from perfect lattice periodicity such as missing, misplaced or foreign ions which act as electron scattering sites. The resistivity at absolute zero (the "residual resistivity") will therefore depend on the concentration of lattice imperfections or "impurities"[6] - the higher the level of impurities, the greater the number of collisions, the shorter the mean free path and the higher the resistivity. Electrons propagating through metallic crystals typically have low-temperature mean free paths of the order of several thousand angstroms although mean free paths of the order of centimetres have been achieved in exceptionally pure crystals.

A disordered metal can be thought of (albeit somewhat crudely) as a crystal with a very high concentration of impurities. If the impurities are predominantly foreign ions substituted randomly into the lattice, then the metal is described as a metal alloy. Alternately, if the impurities are for the most part ions displaced randomly from their lattice positions, the metal is described as structurally disordered or *amorphous*. Provided the introduction of high concentrations of impurities has no effect on electron conduction other than to increase the density of electron scattering sites, then the simple arguments presented above suggest that the residual resistivity of a disordered metal should be much greater than the same metal in the crystalline state. Although the concept of residual resistivity is not strictly applicable to Ta since it is a superconductor at low temperatures, it is nevertheless instructive to compare the low-temperature resistivity of the ordered and disordered forms. The low temperature resistivity (above the superconducting transition) of bulk bcc Ta, although dependent on the level of impurities, is typically less than 1μΩ·cm which suggests the electron mean free path is greater than 300Å. In contrast, the Ta in this study has a low temperature resistivity of ~220μΩ·cm and hence, from Equation 5.1, an electron mean free path of 1.4Å[7]. (The electron mean free paths are calculated using values of n_e and υ_F estimated from a free electron model[8] - details are given in Table 5.1.) Two points are worthy of note: firstly, as expected, the mean free path in disordered Ta is much shorter than that in ordered Ta and secondly, the mean free path in disordered Ta is less than the inter-ion spacing. The second observation implies that the electron suffers approximately twice as many collisions as an electron colliding at every ionic site which is clearly unphysical. We are forced to conclude that the resistivity is much too large to be explained in terms of scattering from impurities alone. In the next section we discuss the explanation for this 'extra' resistivity. It is useful to define a transport relaxation time τ_{tr} and a corresponding mean free path l_{tr} as that which would be deduced directly from the resistivity using Equation 5.1. We shall show that τ_{tr} and l_{tr} are not generally equivalent to the total relaxation time τ and total mean free path l. Furthermore, even though l_{tr} may be less than the inter-ionic spacing, l remains well behaved.

---

[5] For a discussion see Rossiter, 1987.

[6] In line with much of the literature concerning conduction in disordered materials, extrinsic deviations from perfect lattice periodicity (that is lattice defects and foreign atoms) will henceforth be referred to collectively as "impurities".

5.1.2 Quantum Interference Effects

It has been assumed up to this point that the high concentration of impurities in a disordered metal has no effect on electron conduction other than to increase the density of electron scattering sites. In this semi-classical treatment, the possibility of quantum interference of scattered electron waves is ignored. In disordered metals however, electrons are scattered from randomly positioned impurities to form a chaotic jumble of electron waves in which interference effects turn out to be very important. A rather clear physical picture of quantum interference at defects (QUIAD)[9] has been given by Bergmann, 1983,

---

[7] The mean free path has been calculated assuming that the density of the Ta in the multilayers is the same as that of bulk Ta. The true density is likely to be somewhat less than 16.6g·cm^{-3}, making the value of l slightly greater than that quoted in the text. The value of l will also be greater if the number of free electrons per atom is less than the assumed five. Neither of these changes, however, alter the qualitative conclusions that are drawn.

[8] It may be more appropriate in the case of bcc Ta to take n_e and v_F from a band structure calculation such as that given by Mattheiss, 1970. This would increase the mean free path corresponding to the quoted low-temperature resistivity of bulk bcc Ta from ~300Å to ~500Å. Again, the qualitative conclusions that are drawn would not be affected.

[9] This acronym was introduced by Bergmann. The original theoretical treatment of QUIAD was as the weakly disordered limit of disorder induced electron localisation. Hence the phenomenon of QUIAD is often referred to as "weak localisation".

Quantity	Symbol	Given by	Value
Atomic Mass	A		180.95 g·mol^{-1}
Mass Density	ρ_m		16.6 g·cm^{-3}
Number of conduction electrons per atom	Z_e		5
Conduction electron density	n_e	$\frac{N_A Z \rho_m}{A}$	2.76 x 10^{23} atoms·cm^{-3}
Radius of sphere whose volume is equal to the volume per conduction electron	r_s	$\left(\frac{3}{4\pi n_e}\right)^{1/3}$	0.95 Å
Fermi wave vector	k_F	$(3\pi^2 n_e)^{1/3}$	2.01 Å^{-1}
Fermi velocity	v_F	$\frac{\hbar k_F}{m}$	2.34 x 10^{6} m·s^{-1}
Fermi energy	ε_F	$\frac{\hbar^2 k_F^2}{2m}$	15.5 eV
Transport mean free path	l_{tr}	$\frac{m v_F}{\rho n_e e^2}$	$\left(\frac{301}{\rho/\mu\Omega\cdot\mathrm{cm}}\right)$ Å

Table 5.1 Free electron values for Ta.

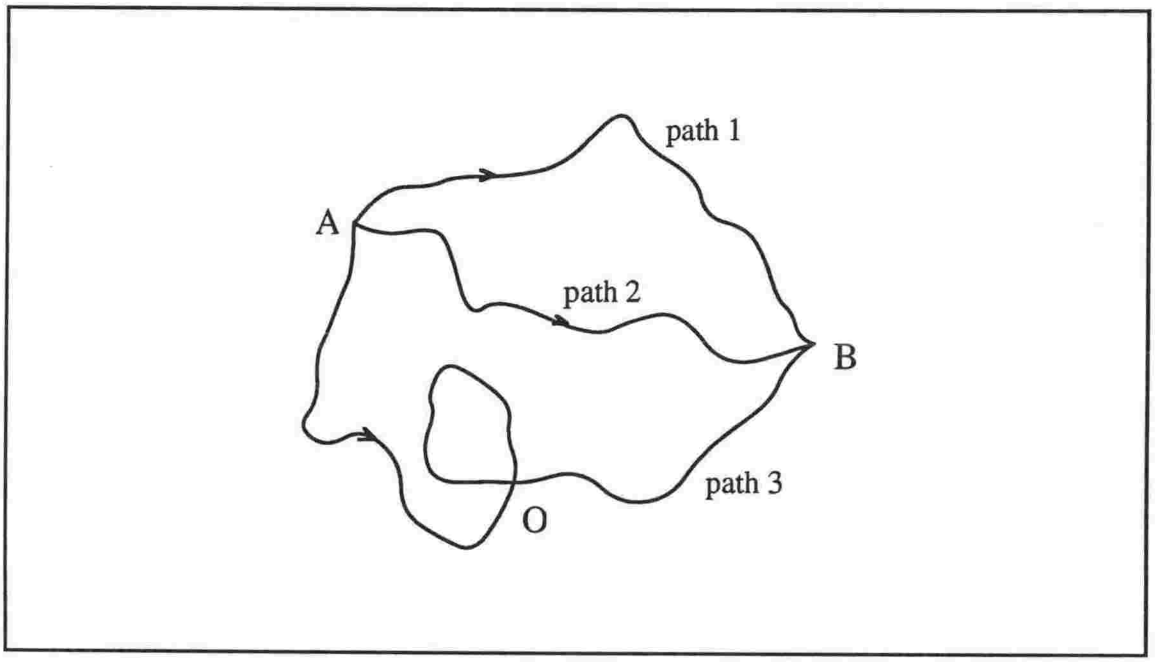

Figure 5.2 Three possible paths for an electron diffusing between points A and B.

and also Alt'shuler & Aronov, 1985. A brief summary of this description is given below.

The problem is modelled as that of a free and independent electron diffusing through an imperfect lattice, that is, the electron is described as a plane wave, and electron-electron interactions[10] are ignored. The picture of electron diffusion is as follows. On colliding with a defect the electron will be *elastically* scattered. Following the collision, the electron will continue to propagate as a plane wave but with a new momentum (note that the magnitude of the momentum remains unchanged - only the direction of propagation is affected in the collision). After some time, the electron will encounter another defect and will be scattered into yet another eigenstate of momentum. The electron's motion is made up of many such steps and the path traced out resembles Brownian motion. A time τ_o may be defined as the average time between elastic scattering events, or equivalently the *lifetime in an eigenstate of momentum*.

Consider now an electron diffusing between two points A and B (see Figure 5.2). The electron may travel via any one of an infinite number of paths. If the amplitude of the probability for an electron to traverse any given path i is A_i then the total probability that the electron diffuses from A to B is

$$\left|\sum_i A_i\right|^2 = \sum_i |A_i|^2 + \sum_{i\neq j} A_i A_j^* . \qquad (5.2)$$

---

[10] The importance of electron-electron interactions will be discussed in Section 5.1.5.

The first term of Equation 5.2 represents the classical probability of diffusion from A to B, while the second represents interference between different paths. Two different types of paths may be distinguished (see Figure 5.2); self-avoiding paths such as paths 1 and 2 and self-intersecting paths such as path 3. Any two self-avoiding paths will not, in general, be of equal length so the wave functions will not be in phase at point B. Thus the interference term averages to zero when summed over all pairs of self-avoiding paths. This is not true however, for self-intersecting paths. The probability of an electron traversing the loop of a self-intersecting path (such as that beginning at point O in path 3) is equal for propagation in either the clockwise or anti-clockwise direction. Because the electron encounters the same scattering potentials traversing each path, the amplitude in the final state is independent of the direction of loop propagation (that is, $A_c = A_{ac} = A$). Moreover, the total phase change for each path is the same because the phase evolves as $Et/\hbar$ and for each step in the clockwise path of duration *t*, and energy E, there is a corresponding step in the anti-clockwise path. The total scattered intensity at the point 0 from the two complementary scattering paths is therefore given by the coherent superposition of the waves, that is

$$\left|A_c + A_{ac}\right|^2 = \left|A_c\right|^2 + \left|A_{ac}\right|^2 + A_c{}^*A_{ac} + A_cA_{ac}{}^* = 4\left|A\right|^2. \qquad (5.3)$$

If the waves were not phase coherent then the total scattered intensity would be only $2\left|A\right|^2$. Thus the constructive interference of scattered waves gives rise to an enhanced probability of finding the electron at point O and hence a reduced probability of finding it at point B.[11] It follows that the conductivity will be *less than* the Boltzmann value. Inelastic scattering events, which destroy phase coherence, become more common as the temperature is increased.[12] As a result, constructive interference at points of self-intersection in the electron's path becomes less probable and the contribution to the resistivity from quantum interference diminishes with temperature, that is, a negative temperature coefficient of resistance (TCR) is expected.

The fractional change in the Boltzmann conductivity when interference effects are included may now be estimated. From the preceding discussion it is clear that the fractional change in the conductivity will be negative and proportional to the probability that the electrons path intersects itself *before* the electron suffers a phase destructive scattering event. Thus

---

[11] Note that an enhanced probability of finding the electron at point O is equivalent to considering the electron to be "weakly localised" at O.

[12] This point will be discussed in more detail in the next section.

$$\frac{\delta\sigma}{\sigma} \sim - \int_{\tau}^{\tau_\phi} \frac{\upsilon \cdot \lambda^2 \cdot \mathrm{d}t}{(Dt)^{3/2}} \; . \tag{5.4}$$

(see Appendix III). Here τ_ϕ is the time over which the wave function retains its coherence or the phase relaxation time, λ is the electron wavelength, υ the electron velocity and D the diffusion constant. Carrying out the integration and setting $L_\phi = \sqrt{D\tau_\phi}$ gives

$$\delta\sigma \sim \frac{e^2}{\hbar L_\phi} + \text{ const.} \tag{5.5}$$

This result was originally derived from scaling arguments in papers by Abrahams et al, 1979, Anderson et al, 1979, Gor'kov et al, 1979 and Kaveh & Mott, 1981(a), 1981(b) &1982(a).

One of the striking features of QUIAD is the strong dependence on the dimensions of the sample. As the electron is constrained to move in a reduced number of dimensions, the probability that the electron's path intersects itself in time τ_ϕ increases.[13] Consequently the correction to the conductivity is more pronounced in lower dimensional systems. A thin film of thickness a may be considered two-dimensional if an electron diffuses across the film many times between phase destructive scattering events i.e. $a << L_\phi$. Similarly a wire of diameter a may be considered one-dimensional if $a << L_\phi$. Equation 5.4 may be generalised for a sample of dimensionality d

$$\frac{\delta\sigma}{\sigma} \sim - \int_{\tau}^{\tau_\phi} \frac{\upsilon \cdot \lambda^2 \cdot \mathrm{d}t}{(Dt)^{d/2}} \cdot \frac{1}{a^{3-d}} \tag{5.6}$$

so that[14]

$$\delta\sigma_d \sim \begin{pmatrix} -\dfrac{e^2}{\hbar} \ln \left(\dfrac{L_\phi}{l_o}\right), & d = 2 \\ -\dfrac{e^2}{\hbar} L_\phi \, , & d = 1 \end{pmatrix} . \tag{5.7}$$

---

[13] For a description of the dimensional dependence of the probability of self-intersection in a random walk see Zallen, 1983.

[14] Note $\sigma_d = \sigma a^{3-d}$, that is σ_2 is the conductance per square and σ_1 is the conductance per unit length.

Note that the expected behaviour of the resistivity is qualitatively the same in each dimension. As the temperature is raised, phase destructive scattering events become more frequent, resulting in a reduction of L_ϕ and of the resistivity.

At this point we make two qualitative observations. Firstly, enhanced backscattering of electrons can explain the 'extra' resistivity discussed at the end of the previous section which cannot be explained by impurity scattering in Boltzmann's equation. Secondly, the negative TCR seen above 20K for all the samples investigated in this study is not inconsistent with quantum interference at defects. Knowledge of how the probability of an electron suffering an inelastic scattering event depends on temperature is required before a quantitative comparison between the theory of QUIAD and the experimental data can be made.

5.1.3 The Phase Relaxation Time

Although QUIAD has been widely accepted as the explanation for the behaviour of a diverse range of disordered materials, there remains considerable controversy as to the mechanism governing the phase relaxation time. The phase relaxation time is defined as the time over which the electron retains its phase coherence. It was originally suggested by Thouless, 1977, that the phase coherence time should coincide with the inelastic scattering time due to either electron-electron or electron-phonon collisions. Later, Alt'shuler et al, 1981 & 1982, pointed out that τ_ϕ should be the time in which the phase of the electron drifts by 2π. If the energy change ΔE in a single collision is large compared with the inelastic scattering rate τ_{in}^{-1} then the phase change $\Delta\phi \sim \Delta E \tau_{in}/\hbar$ is of the order of unity and $\tau_\phi \sim \tau_{in}$. However, if $\Delta E \ll \hbar\tau_{in}^{-1}$ it will take many inelastic collisions before the phase of the electron is altered by 2π. In general they estimate that the phase relaxation time should be related to the inelastic scattering time as

$$\tau_\phi \sim \left(\frac{\Delta E\,\tau_{in}}{\hbar}\right)^{-2/3} \tau_{in}. \tag{5.8}$$

The energy transferred in a single inelastic electron-phonon collision is generally large so that the phase relaxation time resulting from electron-phonon collisions is correctly given by the inelastic scattering time. This is not necessarily true for electron-electron scattering. This point will be discussed in more detail below.

By way of analogy with a pure crystal, it seems likely that electron-phonon scattering will dominate at high temperatures with electron-electron scattering only becoming significant at very low temperatures. An electron may also lose phase coherence due to spin-spin scattering. These three mechanisms will be discussed below.

5.1.3.1 Electron-Phonon Scattering

Before discussing the problem of electron-phonon scattering in a disordered lattice it is instructive to review the well established result obtained in the case of an ordered lattice.[15] At temperatures greater than the Debye temperature Θ_D, all phonon modes are excited. In this regime the number of phonons in any normal mode increases linearly with temperature with the result that the probability of electron-phonon collisions also increases linearly with temperature. Thus

$$\tau^{-1}_{el\text{-}ph} \propto T , \qquad\qquad T \gg \Theta_D \tag{5.9}$$

where $\tau_{el\text{-}ph}$ is the average time between electron-phonon collisions. At low temperatures ($T \ll \Theta_D$) where not all phonon modes are excited, the number of phonons that can scatter electrons varies as T^2. To see this consider the following argument. Electron-phonon scattering events can be thought of as the emission or absorption of a phonon by the electron.[16] At a given temperature the only phonons present in appreciable numbers - and therefore available for absorption - are those with energy less than k_BT. In the case of emission, only phonons of energy of the order of k_BT are generated since the electron must 'fall' into an empty state after emitting a phonon and the only empty states are those within k_BT of the Fermi level. Thus for both emission and absorption the phonon energy $\hbar\omega(q_{ph}) \leq k_BT$. This implies that the phonon wave vector q_{ph} is small and the dispersion relation $\omega(q_{ph}) = cq_{ph}$ is valid. (Note that c is the velocity of sound.) Hence

$$q_{ph} \sim \frac{k_BT}{\hbar c} \ . \tag{5.10}$$

Conservation of energy and crystal momentum restrict those phonons which can participate in electron-phonon scattering to those on a two dimensional surface in momentum space. The condition that $\hbar\omega(q_{ph}) \leq k_BT$ further restricts the participating phonons to an area on this two dimensional surface of area of the order of ${q_{ph}}^2$. Hence from Equation 5.10 the number of phonons that can scatter electrons increases as T^2. However, the electron-phonon scattering rate also depends on the effective coupling between electrons and phonons. For small q_{ph} this introduces another factor of T to the temperature dependence of $\tau_{el\text{-}ph}^{-1}$. The low temperature electron-phonon scattering rate therefore depends on temperature as

---

[15] See, for example, Ashcroft & Mermin, 1976, for a more rigorous discussion.

[16] Only single phonon processes will be discussed here although in principle more than one phonon may be absorbed or emitted in a single collision.

$$\tau_{el\text{-}ph}^{-1} \sim T^3, \qquad\qquad T \ll \Theta_D \,. \tag{5.11}$$

We now turn to the question of how disorder affects the electron-phonon scattering rate. Provided the disorder is only very weak (that is, $q_{ph}^{-1} < l$), the system is said to be "clean" and Equations 5.9 and 5.11 should be applicable. Howson & Greig, 1986, were able to explain the temperature dependence of the resistivity of $Cu_{50}Zr_{50}$ and $Cu_{50}Hf_{50}$ alloys above 100K using the theory of QUIADs with a phase breaking rate due to electron-phonon scattering varying linearly with T. Similarly Santhanam et al,1987, deduced an electron-phonon scattering rate $\sim T^3$ at low temperatures from measurements of aluminium films. In the "dirty" limit ($q_{ph}^{-1} > l$) the situation is not so clear. Several authors[17] have proposed that the electron-phonon relaxation time at low temperatures should be modified from T^3 to T^2 for disordered materials. The underlying argument is that the restriction of momentum conservation is relaxed so that the number of phonons able to participate in electron-phonon scattering increases as T rather than T^2. Garland et al, 1968, point out that the forces between ions should be weaker in a disordered lattice than in a perfect crystal. This has the effect of shifting the phonon spectra to lower frequencies, increasing the average amplitude of ionic vibrations and therefore enhancing the coupling between electrons and phonons. Chakravarty & Schmid, 1986, give a complete analysis of the problem which takes both these factors into account. They find a T^4 dependence at low temperatures and a T^3 or T^2 dependence at higher temperatures for scattering involving longitudinal and transverse phonons respectively. The explicit expressions for the inelastic scattering rate due to electron-phonon collisions are

$$\frac{1}{\tau_{el\text{-}phL}} = \left(\begin{array}{ll} \dfrac{7\pi\zeta(3)}{12} \cdot \dfrac{(k_BT)^3}{\hbar m M c_L^4} \,, & k_BT \gg \dfrac{\hbar c_L}{l} \,, \\[2ex] \dfrac{\pi^4}{30} \cdot \dfrac{l(k_BT)^4}{\hbar^2 m M c_L^5} \,, & k_BT \ll \dfrac{\hbar c_L}{l} \,, \end{array} \right), \tag{5.12a}$$

---

[17] Koshino,1960, Kagan & Zhernov, 1966, and Bergmann, 1971.

$$\frac{1}{\tau_{el\text{-}phT}} = \left(\begin{array}{ll} \frac{7\pi^2}{2} \cdot \frac{(k_BT)^2}{mMc_T^3 l} , & k_BT \gg \frac{\hbar c_T}{l} , \\ \frac{\pi^4}{20} \cdot \frac{l(k_BT)^4}{\hbar^2 mMc_T^5} , & k_BT \ll \frac{\hbar c_T}{l} . \end{array} \right) . \tag{5.12b}$$

where $\tau_{el\text{-}phL}$ and $\tau_{el\text{-}phT}$ are the times between electron collisions with longitudinal and transverse phonons respectively, M is the ionic mass, m the electronic mass, c_L and c_T are the longitudinal and transverse sound velocities and $\zeta(z)$ is the Riemann zeta function[18]. As discussed earlier the phase breaking rate for electron-phonon collisions is identical to the inelastic scattering rate for electron-phonon collisions.

We conclude this section by noting that we have only considered electron-phonon scattering in three dimensions. If the effective dimensionality of the phonons is limited by the size of the sample ($a < q_{ph}^{-1}$) then the number of phonon modes is restricted and the rate of electron-phonon collisions will depend less strongly on temperature (see for example Anderson et al, 1979).

5.1.3.2 Electron-Electron Scattering

Consider first electron-electron scattering in a periodic ionic lattice. Although the Coulomb force which governs the interaction between electrons is strong, the electron-electron scattering rate is quite small for two reasons. Firstly, the Coulomb interaction between any two electrons is reduced due to screening of the interaction due to the remaining electrons and secondly, the exclusion principle restricts the scattering processes to those where the two interacting electrons are scattered into empty states. This second consideration leads to an inelastic electron-electron scattering rate $\tau_{ee}^{-1} \sim T^2$.

If the underlying ionic lattice is disordered, the Coulomb attraction between electrons will be less effectively screened. More importantly, electron-electron interactions give rise to a significant alteration of the density of states at the Fermi level (this will be discussed in more detail in Section 5.1.5). Schmid, 1974, and Alt'shuler & Aronov, 1979(a) & 1981, predict that the inelastic scattering rate due to electron-electron scattering would depend on temperature as

$$\tau_{ee}^{-1} \propto T^{d/2} \tag{5.13}$$

---

[18] For z > 1 the Riemann zeta function is given by $\sum_{n=1}^{\infty} 1/n^z$ so $\zeta(3) = 1.202$.

with the constant of proportionality being a function of the disorder. Equation 5.13 represents the contribution to the electron-electron scattering rate from collisions where the energy transferred between colliding electrons is large (~T). Alt'shuler et al, 1981 & 1982, pointed out that interactions involving only small energy transfers could in some cases give a larger phase breaking rate than inelastic electron-electron collisions. By considering the influence of an external high frequency electric field, which is equivalent to the interaction of an electron with the fluctuating electromagnetic field produced by all the other electrons, they found

$$\tau_\phi^{-1} \propto T^{2/(4-\mathrm{d})} \tag{5.14}$$

In two dimensions it turns out that Equation 5.14 gives a larger phase breaking rate than Equation 5.13 and therefore

$$\frac{1}{\tau_\phi} = \frac{\pi k_B T}{\hbar} \cdot \frac{R_\square e^2}{2\pi^2 \hbar} \cdot ln\left(\frac{\pi \hbar}{e^2 R_\square}\right) \tag{5.15}$$

In three dimensions the reverse is true[19] and the phase breaking rate should be given by τ_{ee}^{-1}, that is

$$\frac{1}{\tau_\phi} = \left\{1 - \frac{3F}{4+F}\left[1 - \left(1 + \frac{F}{2}\right)^{3/2}\right]\right\} \cdot \frac{1}{12\sqrt{2}\pi^2 N \hbar} \cdot \left(\frac{k_B T}{\hbar D}\right)^{3/2} \tag{5.16}$$

where ~~κ is the inverse screening length and~~ F is a screening factor averaged over the Fermi surface. In deciding whether a sample is one, two or three dimensional with respect to electron-electron scattering the relevant length scale to consider is the diffusion length L_T where L_T is given by

$$L_T = \sqrt{\frac{D\hbar}{k_B T}} \quad . \tag{5.17}$$

Thus a cross-over in sample dimensionality is expected when the sample dimension a is of the order of L_T. Note that Equation 5.16 is only valid if $a \gg L_T \gg L_\phi$ and Equation 5.15 only if $a \ll L_T \ll L_\phi$. If the sample dimensions are such that $L_T \ll a \ll L_\phi$ then $\tau_\phi^{-1} \sim -TlnT + T^{3/2}$ (see Alt'shuler & Aronov, 1985, for a more complete description).

---

[19] This is true at temperatures less than about 1000K. At higher temperatures the electron-electron scattering rate given by Equation 5.14 becomes larger than that given by Equation 5.13.

5.1.3.3 Spin-Spin Scattering

If an electron diffusing in a disordered system encounters a magnetic impurity then it will undergo spin-spin scattering in which the spin of the conduction electron may be 'flipped'. As a result of spin-flip scattering, the two final wave functions from the complementary scattering paths considered in Section 5.1.2 will differ in their final spin states and therefore the constructive interference will be destroyed. The average time between magnetic scattering events τ_s will be independent of temperature provided τ_s is much greater than τ_o.

5.1.3.4 Summary

The phase breaking rate is often written as

$$\frac{1}{\tau_\phi} = \beta T^{\,p} \tag{5.18}$$

where β is a constant and p depends on the size of the sample, the degree of disorder, the temperature and the phase breaking mechanism. Where more than one independent phase breaking mechanism is important it is generally assumed that the total phase breaking rate is given by the sum of the individual rates.

An order of magnitude estimate of the various scattering rates for disordered Ta can be made using the values in Table 5.1 and taking $c_T = 2036\text{m}\cdot\text{s}^{-1}$, $c_L = 4159\text{m}\cdot\text{s}^{-1}$ (see Kaye & Laby, 1986) and $\rho \approx 200\mu\Omega\cdot\text{cm}$. The results are given in Table 5.2 overleaf. Notice that the electron-phonon scattering rate is greater than the electron-electron scattering rate at high temperatures while at low temperatures the reverse is true. Notice also, that the dominance of electron-electron scattering extends to much higher temperatures than would be expected in the case of a pure crystal.

5.1.4 Spin-Orbit Scattering

One of the most surprising features of the theory of quantum interference in disordered materials is the effect of spin-orbit coupling. Hikami et al, 1980, calculated that the presence of spin-orbit coupling should not merely destroy the *constructive* interference as is the case for electron-phonon and electron-electron scattering but rather it should give rise to *destructive* interference. The correction to the resistivity is then

Scattering Mechanism		p	Phase Breaking Rate / s^{-1}			
			1K	10K	100K	300K
electron-phonon "clean"		1	-	-	$0.3\text{x}10^{15}$	$1\text{x}10^{15}$
electron-phonon "dirty"	low temperature - longitudinal	4	$5\text{x}10^{3}$	$50\text{x}10^{6}$	$0.5\text{x}10^{12}$	-
	- transverse	4	$0.2\text{x}10^{6}$	$2\text{x}10^{9}$	$20\text{x}10^{12}$	-
	high temperature - longitudinal	3	-	-	-	$20\text{x}10^{12}$
	- transverse	2	-	-	$0.2\text{x}10^{15}$	$2\text{x}10^{15}$
electron-electron "clean"		2	$3\text{x}10^{6}$	$0.3\text{x}10^{9}$	$30\text{x}10^{9}$	$0.3\text{x}10^{12}$
electron-electron "dirty"	two dimensions	1	$20\text{x}10^{9}$	$0.2\text{x}10^{12}$	$2\text{x}10^{12}$	$6\text{x}10^{12}$
	three dimensions	$1\frac{1}{2}$	$8\text{x}10^{7}$	$2\text{x}10^{9}$	$80\text{x}10^{9}$	$0.4\text{x}10^{12}$

Table 5.2 Order of magnitude estimates for the phase breaking rates in disordered Ta using free electron values from Table 5.1 and other values as noted in the text. In two dimensions the electon-electron scattering rate depends on the film thickness - here the thickness is taken to be 10Å. Note that the temperature $\hbar c/k_B l$ separating the high and low temperature regimes in "dirty" electron-phonon scattering is ~100K for scattering from transverse modes and ~210K for scattering from longitudinal modes.

positive rather than negative. Bergmann, 1982(d), explained this result using the physical picture introduced in Section 5.1.2.

Spin-orbit coupling will cause the spin of a diffusing electron to be slightly rotated in a collision with an impurity. After traversing the loop of a self-intersecting path, the electron will have undergone many such infinitesimal rotations. The final spin state of the electrons traversing the loop clockwise s_c will be related to the initial state s by a finite rotation R, that is,

$$s_c = R \cdot s. \tag{5.19}$$

An electron traversing the loop in the opposite direction will suffer the same infinitesimal rotations but in the opposite direction and sequence so that

$$s_{ac} = R^{-1} \cdot s. \tag{5.20}$$

R may be written (Feynman, 1971)

$$R = \begin{pmatrix} cos(\theta/2)e^{i(\phi+\psi)/2} & isin(\theta/2)e^{-i(\phi-\psi)/2} \\ isin(\theta/2)e^{i(\phi-\psi)/2} & cos(\theta/2)e^{-i(\phi+\psi)/2} \end{pmatrix} \tag{5.21}$$

where θ, ϕ and ψ are Euler angles giving the orientation of the final state relative to the initial state. The interference amplitude $A_c{}^*A_{ac} + A_cA_{ac}{}^*$ will now be modified by the scalar product $\langle s_c | s_{ac} \rangle = \langle R \cdot s | R^{-1} \cdot s. \rangle$. Writing $s = (a,b)$ gives

$$\begin{aligned}(R \cdot s\,)^*(R^{-1} \cdot s) = {} & cos^2(\theta/2)\left[aa^*e^{-i(\phi+\psi)} + bb^*e^{i(\phi+\psi)}\right] \\ & - (aa^* + bb^*)sin^2(\theta/2) \\ & - \tfrac{i}{2}\sin(\theta)\left[a^*b(e^{-i\phi} + e^{i\psi}) + ab^*(e^{i\phi} + e^{-i\psi})\right]\end{aligned} \tag{5.22}$$

If there is no spin-orbit coupling then the spin of the electron will be unchanged by the scattering process so that $\theta = \phi = \psi = 0$, and the scalar product $\langle s_c | s_{ac} \rangle$ is equal to $aa^* + bb^* = 1$. In this case the interference term is unmodified and the problem reduces to that considered in Section 5.1.2 as expected. In the presence of strong spin-orbit coupling the orientation of the final spin state will be random. The first and last terms in Equation 5.22 average to zero when integrated over 4π (the rotational periodicity of the electron) and the scalar product is therefore given by

$$\langle s_c | s_{ac} \rangle = \frac{1}{(4\pi)^3}\int_0^{4\pi} -\sin^2(\theta/2)d\theta \int_0^{4\pi} d\phi \int_0^{4\pi} d\psi \;=\; -\tfrac{1}{2} \tag{5.23}$$

Thus the interference amplitude is *reduced* by a factor of two and *opposite* in sign. This destructive interference of scattered waves reduces the probability of finding the electron at point O (Figure 5.2) and therefore increases the probability that the electron diffuses from A to B. The correction to the conductivity is now positive. As the temperature is increased an electron traversing the loop in the clockwise direction will not undergo the same infinitesimal rotations as an electron traversing the loop in the anticlockwise direction because of phase destructive scattering events. Thus the destructive interference is progressively destroyed as the temperature rises. At some temperature the orientation of the final spin states relative to the initial states will be entirely random, that is the scalar product $\langle s_c | s_{ac} \rangle = 1$, and the constructive interference arising from the interference amplitude $A_c{}^*A_{ac} + A_cA_{ac}{}^*$ will be revealed. In terms of the resistivity, this gives a positive TCR at low temperature where spin-orbit effects dominate turning to a negative TCR at higher temperatures. The temperature at which the maximum in the resistivity occurs will depend on the relative strengths of the spin-orbit and the phase destructive scattering.

5.1.5 Summary: Quantum Interference Effects

The full equation for the correction to the conductivity due to quantum interference in a disordered material, including the effect of spin-orbit scattering in two dimensions is (Hikami et al.,1980)

$$\delta\sigma_2^{QI} = L_{oo} \cdot \left[\tfrac{3}{2} ln\left(\tau_1^{-1}\right) - \tfrac{1}{2} ln\left(\tau_2^{-1}\right) - ln\left(\tau_o^{-1}\right)\right] \tag{5.24}$$

where τ_o^{-1} is the elastic scattering rate from impurities,

$$\begin{aligned} \tau_1^{-1} &= \tfrac{4}{3}\tau_{so}^{-1} + \tfrac{2}{3}\tau_s^{-1} + \tau_\phi^{-1}, \\ \tau_2^{-1} &= 2\tau_s^{-1} + \tau_\phi^{-1}, \\ L_{oo} &= \frac{e^2}{2\pi^2\hbar} \approx 1.23 \text{ x } 10^{-5}\ \Omega^{-1}, \end{aligned} \tag{5.25}$$

τ_{so}^{-1} is the spin-orbit scattering rate and the contribution to the phase breaking rate from spin-spin scattering is given explicitly. In three dimensions (Fukuyama & Hoshino, 1981)

$$\delta\sigma_3^{QI} = L_{oo} \cdot \frac{1}{\sqrt{D}} \cdot \left[3\sqrt{\tau_s^{-1} + \tau_{so}^{-1} + \tfrac{1}{4}\tau_\phi^{-1}} - \tfrac{1}{2}\sqrt{\tau_s^{-1} + \tau_\phi^{-1}}\right] + const. \tag{5.26}$$

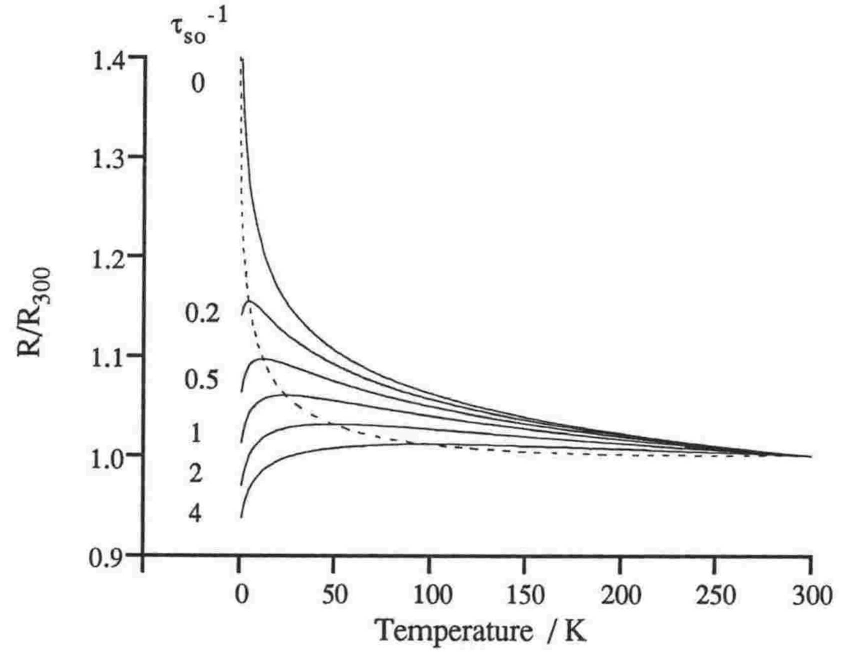

Figure 5.3 Quantum interference correction to the resistivity (normalised to the resistance at 300K) for different spin-orbit scattering rates (in $(\mathrm{ps})^{-1}$). Dotted line denotes the transition from weak localisation (above the line) to weak anti-localisation (below the line). Curves calculated using Equation 5.24 with $\tau_s^{-1} = 0.01(\mathrm{ps})^{-1}$ and $\tau_\phi^{-1} = 0.02T\,(\mathrm{ps})^{-1}$ (that is, electron-electron scattering in two dimensions - see Table 5.2).

where the constant is of the order of L_{oo} / l_o.

In general τ_s^{-1} and τ_{so}^{-1} are several orders of magnitude smaller than τ_ϕ^{-1} and do not contribute significantly to the conductivity. Equations ~~5.25~~ 5·24 and 5.26 reduce to Equations 5.5 and 5.7 and the resistivity *increases* as the temperature is lowered. However at low temperatures τ_ϕ^{-1} may become small enough that τ_{so}^{-1} and τ_ϕ^{-1} are of the same order of magnitude so that behaviour characteristic of weak antilocalisation is revealed (that is, the resistivity begins to *decrease* as the temperature is lowered - see Figure 5.3). A cross-over from a negative TCR to a positive TCR at low temperature is expected in disordered Ta since Ta is a strong spin-orbit scatterer.

The theory of weak localisation of QUIADs was originally derived in the limit of weak scattering, that is, $k_F l \gg 1$. Although it is not obvious from the discussion that has been given here, this limit arises because the expressions for $\delta\sigma^{QI}$ are derived from perturbation theory involving an expansion to only first order in $(k_F l)^{-1}$. For strong scattering materials, that is materials for which the above condition is not satisfied, higher order corrections may be required. Morgan et al., 1985, and Morgan & Hickey, 1985, analyse the problem for strong scatterers and Bloch states rather than weak scatterers and plane waves states and find that higher order terms may be neglected provided $k_F l > 1$ (rather than $k_F l \gg 1$).

To interpret the measured conductivity and its temperature dependence, the magnitude and temperature dependence of the normal conductance must also be considered. Howson, 1984, argues in the following manner. The total conductivity will be given by $\sigma = \sigma_B + \delta\sigma^{QI}$. By writing $n_e = k_F^3/3\pi^2$, $\tau/m = l/\hbar k_F$ and $l^{-1} = l_o^{-1} + l_{in}^{-1}$ (where l_{in} is the temperature dependent inelastic scattering length) Equation 5.1 for the Boltzmann conductivity may be separated into a temperature dependent and a temperature independent term:

$$\sigma_B(T) = \frac{e^2}{3\pi^2\hbar} \cdot \frac{k_F^{2} l_o l_{in}}{l_o + l_{in}} \approx \frac{2}{3} L_{oo} \, (k_F l_o)^2 \left(\frac{1}{l_o} - \frac{1}{l_{in}(T)}\right) \tag{5.27}$$

The total temperature independent term σ_o is then

$$\sigma_o = \frac{L_{oo}}{l_o} \left(\frac{2}{3} (k_F l_o)^2 - 1\right) \tag{5.28}$$

and the total temperature dependent term (in three dimensions)

$$\sigma(T) = L_{oo} \cdot \left[\frac{3}{\sqrt{D}} \sqrt{\tau_s^{-1} + \tau_{so}^{-1} + \frac{1}{4}\tau_\phi^{-1}} - \frac{1}{2\sqrt{D}} \sqrt{\tau_s^{-1} + \tau_\phi^{-1}} - \frac{2}{3}(k_F l_o)^2 \frac{1}{l_{in}(T)}\right] \tag{5.29}$$

Three cases arise; (1) for very weak scattering ($\rho < 50\mu\Omega\cdot$cm) the normal conductivity dominates causing the conductivity to decrease with increasing temperature, (2) for weak scattering ($50\mu\Omega\cdot\text{cm} < \rho < 150\mu\Omega\cdot$cm) quantum interference effects become important at low temperatures causing a low temperature maximum in the conductivity and (3) for strong scattering ($\rho > 150\mu\Omega\cdot$cm), quantum interference effects dominate the temperature dependence of the conductivity at all temperatures so that the conductivity decreases with increasing temperature. This is the origin of the Mooij correlation discussed in Chapter One.

5.1.6 Electron-Electron Interaction

The corrections to the conductivity discussed so far arise from the theory of quantum interference effects which is essentially a non-interacting theory. In this section the importance of electron-electron interaction in disordered media will be discussed.

In a pure crystal, it is conceivable that the electron cloud is sufficiently uniform that interactions between electrons merely alter the average field experienced by an individual electron. This picture oversimplifies the problem. Although the average electron density is uniform, there will be local fluctuations in density which will be felt throughout the electron cloud on account of the long range of the Coulomb interaction. A quantum mechanical analysis treating the Coulomb force as a small perturbation suggests a high probability for pairs of interacting electrons to make transitions involving small momentum changes. A strong singularity in the density of states near the Fermi level is also predicted. Coulomb repulsion makes it favourable for electrons to remain well separated so that there is an area surrounding each electron from which all other electrons are effectively excluded. Such a gap in the electron cloud (or 'correlation hole') acts as a positive charge, reducing the the potential of a given electron that is seen by all the other electrons. The singularity in the density of states disappears when the bare Coulomb potential is replaced by a short ranged or *screened* Coulomb potential. It is concluded finally that the predicted properties of pure crystals show no new features as a result of including the interaction between electrons - they are merely given by a renormalisation of the results found in the independent electron approximation.[20]

This is not so in a disordered material. Alt'shuler & Aronov, 1979(b) first showed that impurity scattering during the time of interaction causes a gap in the density of states[21] near the Fermi level even when screening is included in the analysis. This so-called "Coulomb' or 'correlation gap" leads to corrections to the temperature dependence of the conductivity as well as other electronic properties (Alt'shuler & Aronov, 1979(c), and Alt'shuler et al, 1980(b)). Although it was initially thought that electron-electron interactions and QUIAD's were competing mechanisms for the explanation of the observed properties of disordered materials at low temperatures, it is now thought that both mechanisms are important. In particular the total correction to the conductivity should be given by the sum of the individual corrections from electron-electron interactions and QUIAD's.

---

[20] For a more detailed discussion see Ziman, 1960.

[21] In a disordered material, the absence of periodicity means $\boldsymbol{k}$ is not a good quantum number, nor is a band structure meaningful. The density of states however, remains a valid description of the electron states (see for example Elliott, 1990).

Electron-electron interactions are treated using perturbation theory by evaluating the Kubo diagrams within the formalism of Green's functions. The diffusion or particle-hole channel describes the interaction between electrons which differ little in energy and momenta while the Cooper or particle-particle channel describes the interaction between electrons with a small total momentum. Both Hartree terms (which describe the effect of the electron cloud on a given electron as a change in the average field) and exchange terms (which describe correlation effects taking the Pauli exclusion principle into consideration) are calculated in each channel. The results for the corrections to the conductivity, omitting the derivations, will be presented below. For a comprehensive review of the theory see, for example, Alt'shuler & Aronov, 1985.

5.1.6.1 The Diffusion Channel

To evaluate the Hartree term it is sufficient to use a static screened Coulomb potential given by the bare Coulomb potential V_b times an exponential damping factor, that is

$$V_s = V_b e^{-\kappa \cdot r} = \frac{e^2}{r} e^{-\kappa \cdot r} \tag{5.30}$$

where κ is the inverse screening length. However, the finite duration of the interaction becomes important for the calculation of the exchange term. Instead of the static screened potential given above, a dynamically screened potential is required. The Fourier transform of the static potential is modified;

$$V(q) = \frac{4\pi e^2}{q^2 + \kappa_3^2} \rightarrow \frac{4\pi e^2}{q^2 + \kappa_3^2\left(\frac{Dq^2}{|\Delta E| + Dq^2}\right)} \tag{5.31a}$$

where $\kappa_3 = \kappa = \sqrt{e^2 N/\varepsilon_o}$ and ΔE is the energy transfer. The effective potential is now short ranged and dependent on the energy transfer. Note that in low dimensional systems, screening is much less effective since only the fraction of the electric flux which lies within the sample can be screened by the electron cloud. For example, in two dimensions Equation 5.31a above is modified to

$$\mathrm{V}(q) = \frac{2\pi e^2}{|q| + \kappa_2} \rightarrow \frac{2\pi e^2}{|q| + \kappa_2\left(\frac{Dq^2}{|\Delta E| + Dq^2}\right)} \tag{5.31b}$$

where $\kappa_2 = \frac{1}{2}e^2 N_2/\varepsilon_o$ (N_2 is the density of states in two dimensions) or $\kappa_2 = \frac{1}{2}\kappa^2 a$ in the quasi two dimensional case. The reduction in the efficiency of screening in reduced dimensions is partially responsible for the enhancement of interaction effects in thin films and wires relative to bulk samples.

The total correction to the conductivity in the diffusion channel, (D), in d dimensions $\delta\sigma_d^{(D)}$ is then calculated as

$$\delta\sigma_1^{(D)} = -\frac{e^2}{4\pi^2\hbar} C_1 \lambda_1 \left(\frac{k_B T}{hD}\right)^{-1/2},$$

$$\delta\sigma_2^{(D)} = \frac{e^2}{4\pi^2\hbar} \lambda_2 \, ln\left(\frac{k_B T \, \tau}{h}\right),$$

$$\delta\sigma_3^{(D)} = \frac{e^2}{4\pi^2\hbar} C_3 \lambda_3 \left(\frac{k_B T}{hD}\right)^{1/2}. \tag{5.32}$$

where $C_1 = -3\sqrt{2\pi^3}\,\zeta(-\frac{1}{2}) = 4.91$ and $C_3 = \sqrt{\pi/8}\,\zeta(\frac{1}{2}) = 0.915$. For the Hartree term $\lambda_d = -2F$ where F is the screening factor introduced in Equation 5.16 and is a function of the disorder. In a free electron model, the screening factor is

$$F = \frac{1}{x^2} ln(1 + x^2), \; x = \frac{2k_F}{\kappa} \tag{5.33}$$

(see Rosenbaum et al., 1981).[22]

For the exchange term $\lambda_d = \frac{4}{d}$. It was initially thought that the total correction to the conductivity would be given by the sum of the contributions from each of the terms, that is $\lambda_d = \frac{4}{d} - 2F$ provided $F \ll 1$. Finklestein, 1983, showed, in the case of two dimensions, that this approach caused a term in λ_d of $-\frac{1}{2}F$ to be counted twice. According to Alshuler & Aronov, 1983, this problem can be corrected by replacing $\lambda_d^{\text{Hartree}} = -2F$ by $-\frac{3}{2}\tilde{F}_{\sigma,d}$ giving $\lambda_d = \frac{4}{d} - \frac{3}{2}\tilde{F}_{\sigma,d}$ where

---

[22] In the purely two dimensional case (Alt'shuler et al. 1980(b)),

$$F = \frac{1}{\pi(x^2 - 1)^{1/2}} \cdot ln\left[\frac{x + \sqrt{x^2 - 1}}{x - \sqrt{x^2 - 1}}\right], x = \frac{\overset{2k_F}{\cancel{2p_F}}}{\kappa_2},$$

while Equation 5.33 is valid for three dimensions, thin films and wires.

$$\tilde{F}_{\sigma,1} = \frac{32}{F}\left[1 + \tfrac{1}{4}F - \left(1 + \tfrac{1}{2}F\right)^{1/2}\right],$$

$$\tilde{F}_{\sigma,2} = \frac{8\,(1 + \tfrac{1}{2}F\,)\,ln(1 + \tfrac{1}{2}F\,)}{F} - 4,$$

$$\tilde{F}_{\sigma,3} = -\frac{32}{3F}\left[1 + \tfrac{3}{4}F - \left(1 + \tfrac{1}{2}F\right)^{3/2}\right]. \qquad (5.34)$$

For $F \ll 1$, $\delta\sigma_d^{(D)}$ increases with increasing temperature. More generally, the sign of $\delta\sigma_d^{(D)}$ depends on the sign of the interaction constant λ_d and may either increase or decrease with temperature. The cross-over in dimensionality occurs when the sample size, a, is of the order of $L_T = \sqrt{D\hbar/k_BT}$ as for electron-electron scattering.

The electron-electron interaction can be thought of as another interference problem. Bergmann, 1987, shows how the Hartree contribution can be described as the scattering of electrons by electron holograms.

5.1.6.2 The Cooper Channel

The most dramatic consequence of electron-electron interaction in the Cooper channel is superconductivity. However, at temperatures greatly in excess of the transition temperature (that is, $T - T_c \gg T_c$) when the system is in the normal state, fluctuation induced formation of Cooper pairs (which is equivalent to electron-electron interaction in the Cooper channel) still gives important corrections to the conductivity. Moreover, the conductivity of non-superconductors is altered by interaction in the Cooper channel. Alt'shuler & Aronov, 1985, give the following results for the corrections to the conductivity $\delta\sigma_d^{(C)}$ in the Cooper channel for a sample of effective dimensionality d :

$$\delta\sigma_1^{(C)} = \frac{e^2}{2\pi^2\hbar}\cdot\frac{C_1}{ln(T_o/T\,)}\cdot\left(\frac{k_BT}{\hbar D}\right)^{-1/2},$$

$$\delta\sigma_2^{(C)} = -\frac{e^2}{2\pi^2\hbar}\,ln\left[\frac{ln(k_BT\tau/\hbar\,)}{ln(T_o/T\,)}\right],$$

$$\delta\sigma_3^{(C)} = -\frac{e^2}{2\pi^2\hbar}\cdot\frac{C_3}{ln(T_o/T\,)}\cdot\left(\frac{k_BT}{\hbar D}\right)^{1/2}, \qquad (5.35)$$

For a superconductor, T_o is the superconducting transition temperature T_c, while for a non-superconductor T_o is the Fermi temperature T_F.

Note that superconducting fluctuations directly above the transition, and the superconducting transition itself, are not considered here. In particular, Equation 5.29 does not include either the Maki-Thompson or the Aslamasov-Larkin corrections due to fluctuation superconductivity. The Aslamasov-Larkin correction is only important for superconductors near T_c and is discussed in the next section. The Maki-Thompson correction however, remains large far from T_c and is also important for non-superconductors. Although the Maki-Thompson correction will also be discussed in more detail in Chapter Six, the result for temperatures much greater than the transition temperature is given here for comparison with the Diffusion and Cooper corrections:

$$\delta\sigma_d^{(M\text{-}T)} = \frac{e^2}{2\pi^2\hbar}\cdot\beta(T)\cdot\begin{cases} 2\pi\sqrt{D\tau_\phi}\,, & d=1,\\ ln\left(\dfrac{k_B T\tau_\phi}{\hbar}\right), & d=2,\end{cases}$$

where

$$\beta(T) = \begin{cases} \dfrac{\pi^2}{6ln^2(T_o/T)}\,, & |ln(T_o/T)| \gg 1,\\ -\dfrac{\pi^2}{4ln(T_o/T)}\,, & -ln(T_o/T) \ll 1.\end{cases} \tag{5.36}$$

(Maki, 1968(a) &1968(b), Thompson, 1970 & 1971 and Larkin, 1980). In three dimensions, at temperatures far from the transition to superconductivity, calculation of the Maki-Thompson correction is complicated but is expected to be much smaller than $\delta\sigma_3^{(C)}$.

5.1.6.3 Summary

The electron-electron interaction corrections discussed in the preceding sections only become important at low temperatures. The diffusion, Cooper and Maki-Thompson corrections for a two dimensional sample are shown in Figure 5.4. Although the behaviour is qualitatively similar for bulk, three dimensional samples, the corrections are smaller by about two orders of magnitude.

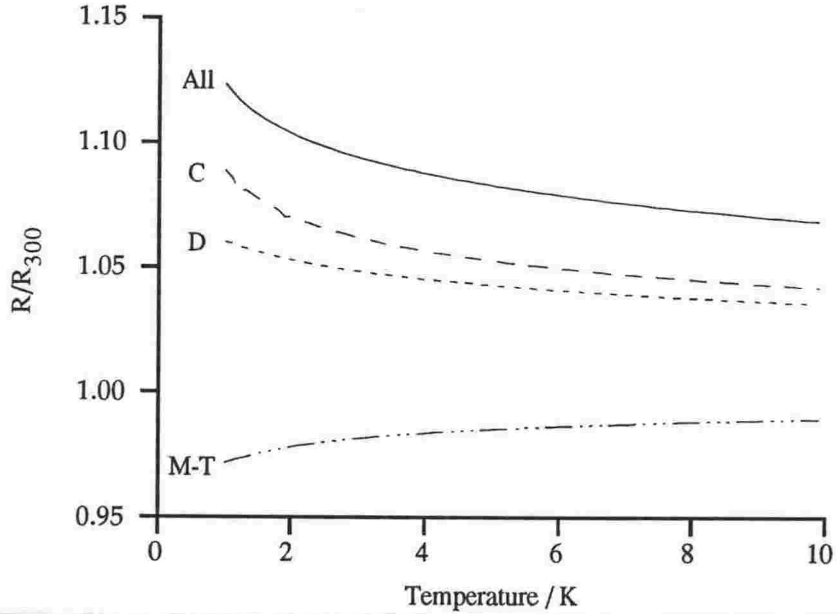

Figure 5.4 Electron-electron interaction correction to the resistance (normalised to the resistance at 300K) for a two dimensional sample - "M-T" - Maki-Thompson correction, "D" - diffusion correction, "C" - Cooper correction, "All" - total electron-electron interaction correction. Curves calculated using data from Table 5.1 and taking $T_c = 0.2$K

5.1.7 Summary

The theoretical predictions for the conductivity of disordered materials stem from three different aspects of the behaviour of electrons. Quantum interference at defects gives rise to weak localization and antilocalisation, the interaction between electrons gives electron-electron interaction effects and fluctuation induced formation of Cooper pairs gives superconducting fluctuations above the transition temperature. Each of these effects results in temperature dependent corrections to the conductivity. The magnitude and functional dependence of the corrections depends critically on the dimensions of the sample relative to some length scale characteristic of the relevant effect. Somewhat more problematic is the dependence on other, less well understood factors, such as the screening length in electron-electron interactions and the phase breaking mechanism (and its temperature dependence) in the theory of weak localisation.

5.2 Experimental Results

The experimental results of the measurement of the resistivity of Ta/Ge multilayers are presented and discussed in the following section. The analysis relies on the assumption that conduction occurs purely within the Ta layers. This assumption is reasonable since the resistivity of amorphous Ge is at least seven orders of magnitude larger than that of the multilayers in the temperature range investigated.[23] Moreover, tunnelling between the layers is not expected provided the Ge layers are rather thick.[24] It is also assumed that the conductivity is not significantly affected by either the small scale variations in layer thickness seen in TEM or by any Ta/Ge compounds that may form at the interfaces. Furthermore we assume that the electrical character of an individual Ta or Ge layer in a multilayer structure is equivalent to an "isolated" layer of the same composition. By making these assumptions the measured resistivity of the multilayers may be treated as that of *n* thin films of Ta connected in parallel. In reality each layer will be slightly altered by the presence of neighbouring layers. In Appendix IV we consider the alteration in the charge distribution near a Ta/Ge interface and conclude that the conduction properties of a Ta layer in a multilayer sample will be equivalent to an isolated Ta film provided the Ta and Ge layers are not extremely thin. The analysis also hinges on whether or not the Ta layers are continuous. Evidence from TEM suggests the Ta layers are indeed continuous down to thicknesses of the order of 10 - 15Å.[25] The fact that even the resistivity of nominally 5Å thick Ta layers is only twice that of the thicker layers supports the assumption that even ultra-thin Ta layers are electrically continuous.

5.2.1 Overview of the Results

The normalised resistance[26] of the multilayers as a function of temperature depends in a systematic way on the Ta layer thickness. A selection of the results for different Ta layer thicknesses are shown in Figure 5.5. Above 20K, the resistance of all the samples

---

[23] See Williams, 1990, for example.

[24] How thick is thick enough is rather a delicate question. Ruggiero et al., 1982, give a tunnelling length of 8Å for Ge, so 50Å to 100Å should be adequate.

[25] Layering is still evident in multilayer samples with Ta layers thiner than 10 - 15 Å but it is no longer clear that the Ta layers are continuous.

[26] As discussed in Chapter 4.3 the multilayer resistance can be measured more accurately than the resistivity.

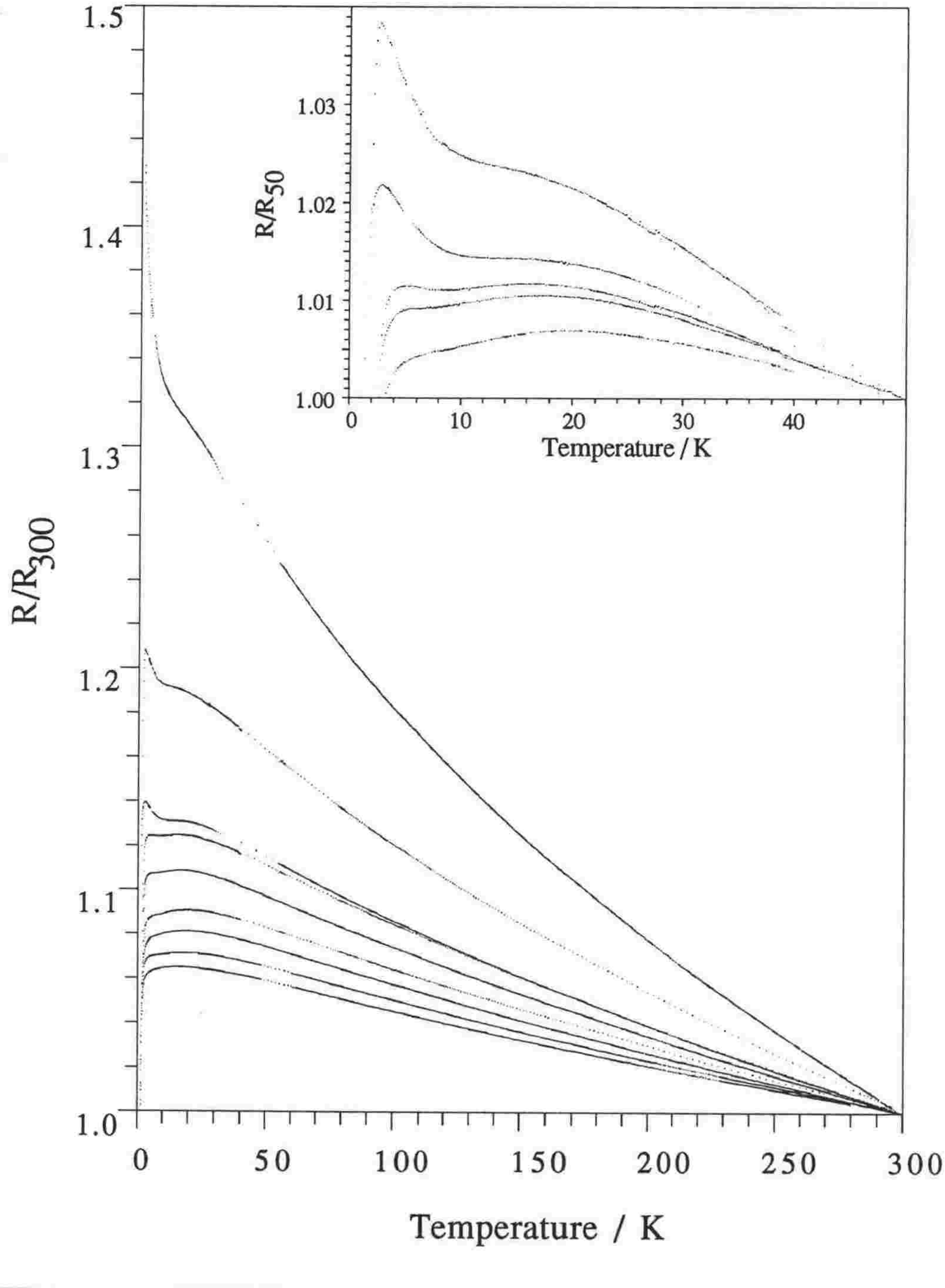

Figure 5.5 Resistance normalised to 300K for multilayers with Ta layers (in units of 10^{15}atoms·cm^{-2}) of (top curve to bottom curve): 2.7±0.2, 5.1±0.3, 6.0±0.3, 7.7±0.5, 9.7±0.6, 11.2±0.7, 17±1, 21±1 and 46±3. Inset shows low temperature resistance normalised to 50K for (top curve to bottom curve in units of 10^{15}atoms·cm^{-2}): 5.1±0.3, 6.0±0.3, 7.7±0.5, 9.7±0.6 and 11.2±0.7. The experimental points are plotted in each case.

increases as the temperature is lowered, the fractional increase being greater for thinner Ta layers. Below 20K, the resistance of thicker layers (>50Å) rises to a maximum and then slowly decreases. At very low temperatures a rapid transition to a superconducting state is seen. The behaviour of the resistance for Ta layers of intermediate thickness (10-40Å - see inset of Figure 5.5) is more complicated. A maximum in the resistance is still evident at about 15-20K but a second feature at low temperature (less than about 6K) causes a minimum below which the resistance increases with the lowering of the temperature. As the Ta layers are made thinner this second feature grows in importance, eventually dominating the low temperature resistance. For the very thinnest Ta layers studied (~5Å) a uniform increase of the resistance with falling temperature was observed with no transition to superconductivity down to the lowest measured temperatures.

What then, is the explanation for these observations? I wish to tentatively suggest the following interpretation. The high temperature region where the resistance decreases with increasing temperature is governed by weak localisation. The turnover to a positive TCR just below 20K marks a transition to weak localisation due to spin-orbit scattering, although superconducting fluctuations may also be important. Still lower in temperature, interaction effects become important causing the return to a positive TCR in samples with thinner layers. That this feature is largest for thin Ta layers, and not seen at all for thick layers is attributed to the strong dependence of interaction effects on the sample thickness. Interaction effects are expected to be small in thick three dimensional layers but should increase in magnitude as the layers become essentially two dimensional. The superconducting transition and its suppression in multilayers with very thin Ta layers will be discussed in Chapter Six.

5.2.2 Characteristic Length Scales of Conduction

In order to attempt a qualitative analysis of the results, it is important to have a clear idea of whether the Ta layers are thicker or thinner than the characteristic length scales of conduction.

With respect to normal conduction, the Ta layers will be three dimensional provided the Ta layer thickness a_{Ta} is very much greater than the mean free path l. From a free electron estimate (see Table 5.1) the mean free path is of the order of a few angstroms so the layers are indeed three dimensional in terms of normal conduction. This implies that the correct form of the diffusion coefficient $D = \upsilon_F l/d$ is $\frac{1}{3}\upsilon_F l$.

The Ta layers will be three dimensional with respect to quantum interference corrections provided the probability that the diffusing electron collides with the interface between phase breaking events is small, that is $a_{Ta} \gg L_\phi = \sqrt{D\tau_\phi}$. An estimate of L_ϕ

requires knowledge of the operative phase breaking mechanism, which itself may be either two or three dimensional in nature. Hence we must first consider the dimensionality of the phase breaking rate.

The characteristic length scale for phonons is $q_{ph}^{-1} = \hbar c/k_B T \approx (250/T)$Å. Thus for Ta layers thicker than ~10Å and at temperatures in excess of ~100K the phonons will be three dimensional. Beyond these limits a transition to two dimensional behaviour is possible. It is more likely however, that phonons extend throughout the entire multilayer rather than being confined solely to the Ta layers and therefore the appropriate phonon scattering rates in all cases should be those derived for three dimensions.

For electron-electron effects (this includes both scattering and interaction) the Ta layers will be three dimensional provided $a_{Ta} \gg L_T$ where L_T is given by Equation 5.17. If the diffusion constant is estimated using free electron values, then $L_T = (300/\sqrt{T}\,)$Å. This implies that very thin Ta layers ($a_{Ta} \gg 20$Å) will be two dimensional with respect to electron-electron effects over the entire temperature range 0-300K while thicker samples will cross-over from three dimensional behaviour at high temperatures to two dimensional behaviour at low temperatures. In the preceding section it was suggested that the resistivity feature at ~ 5K was caused by interaction effects and that a cross-over in dimensionality of the effect occurred as the Ta layer thickness was reduced below ~ 40Å. If we now calculate the Ta layer thickness at which $L_T(5\text{K}) = a_{Ta}$ we find $a_{Ta} \sim 100$Å. Bearing in mind that the calculated values of L_T are estimates only,[27] this result is not inconsistent with the interpretation of the low temperature feature as being due to a cross-over in dimensionality of electron-electron interaction effects.

We now return to the question of the magnitude of the phase breaking rate. In Figure 5.6, L_ϕ as a function of temperature is plotted assuming both electron-electron and electron-phonon scattering contribute to the phase breaking rate. Electron-phonon scattering is assumed to be in a three dimensional regime while electron-electron scattering may be either two or three dimensional. In practice the dimensionality of the electron-electron scattering makes little difference to L_ϕ except at very low temperatures, so only the case of three dimensional electron-electron scattering is plotted for clarity. Spin-spin scattering is assumed to be negligible. The thermal diffusion length L_T is also plotted for comparison. It can be seen that, although very thin samples will be two dimensional with respect to localisation effects, the majority of samples will be three dimensional at high temperatures crossing over to two dimensionality at low temperatures, the cross-over temperature depending on the Ta layer thickness.

---

[27] For example Bergmann, 1984, gives $L_T = \sqrt{Dh/2\pi k_B T}$. The cross-over in dimensionality of electron-electron effects should then be expected at $a_{Ta} \sim 50$Å rather than ~100Å. Also, the diffusion constant is likely to be lower in these samples than the free electron value, further reducing the Ta layer thickness at which the cross-over is predicted.

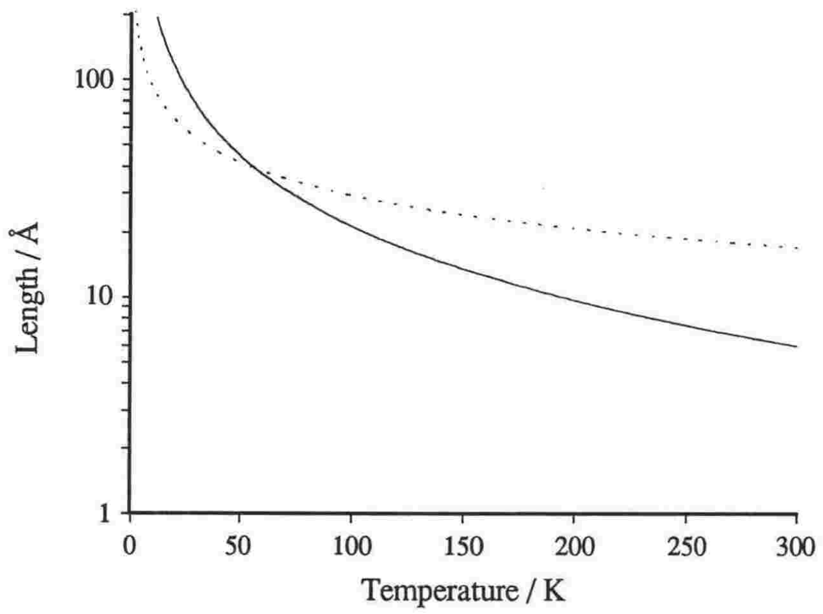

Figure 5.6 The predicted phase breaking length L_ϕ (solid curve) and diffusion length L_T (dashed curve) as a function of temperature.

The preceding dimensional analysis suggests that the range of Ta layer thicknesses examined in this study span the transition from two dimensional to three dimensional behaviour for quantum interference effects as well as for electron-electron effects. This makes the analysis more complicated, not only because it is unclear which theoretical predictions should be applied (two dimensional or three dimensional) but also because much of the data lies in intermediate regimes where neither two dimensional nor three dimensional predictions are strictly valid. In Table 5.3, calculated values of the constants introduced in Section 5.1 and the various characteristic lengths are presented.

5.2.3 Room Temperature Resistivity

Ta is known to form a number of different thin film phases - body centred cubic (bcc), tetragonal (β-Ta), and face centred cubic (fcc).[28] While the properties of the bcc

---

[28] See Baker, 1972.

Quantity	Symbol	Given by	Value
Speed of sound	c_T, c_L	Kaye and Laby, 1986	$2036\text{m}\cdot\text{s}^{-1}$, $4159\text{m}\cdot\text{s}^{-1}$
Transport mean free path	l_{tr}	from Table 5.1 with $\rho = 200\mu\Omega\cdot\text{cm}$	1.5 Å
Density of states	N	$\dfrac{mk_F}{\hbar^2\pi^2}$	$1.67 \times 10^{47}\ \text{J}^{-1}\cdot\text{m}^{-3}$
Diffusion constant	D	$\frac{1}{3}\,v_F l$	$1.2 \times 10^{-4}\ \text{m}^2\cdot\text{s}^{-1}$
Inverse phonon wave vector	q_{ph}^{-1}	$\dfrac{\hbar c_T}{k_B T}$, $\dfrac{\hbar c_K}{k_B T}$	$\left(\dfrac{155}{T}\right)$Å , $\left(\dfrac{318}{T}\right)$Å
Thermal diffusion length	L_T	$\sqrt{\dfrac{D\hbar}{k_B T}}$	$\left(\dfrac{300}{\sqrt{T}}\right)$Å
Localisation length	L_ϕ		(see Figure 5.6)
Screening length	κ^{-1}	$\sqrt{\dfrac{\varepsilon_0}{e^2 N}}$	0.45 Å
	F	Equation 5.33	0.44
	$\tilde{F}_{\sigma,2}$	Equation 5.34	0.41
	$\tilde{F}_{\sigma,3}$	Equation 5.34	0.43
Interaction constant - two dimensions	λ_2	$2 - \frac{3}{2}\tilde{F}_{\sigma,2}$	1.39
- three dimensions	λ_3	$\frac{4}{3} - \frac{3}{2}\tilde{F}_{\sigma,3}$	0.69

Table 5.3 Characteristic length scales of conduction and values of constants introduced in Section 5.1.

and fcc phases differ only slightly from bulk bcc Ta, β-Ta has a much higher resistance (180-220μΩ·cm) and a TCR opposite in sign and much reduced in magnitude (-150ppm·K^{-1})[29]. In addition Nestell et al., 1982, observed an amorphous phase with a resistivity of 220μΩ·cm and a very small TCR when they evaporated Ta onto liquid nitrogen cooled substrates. The Ta in this study (with the exception of the very thinnest layers and those with a high concentration of impurities) has a room temperature resistivity of (200±50)μΩ·cm and a TCR of the order of -200 ppm·K^{-1}. These results suggest the Ta is forming in an amorphous phase although the β-phase cannot be ruled out.

In Chapter 2 (see Table 2.2) the impurity concentration in the Ta layers for each evaporation was estimated from the deposition parameters and was found to range from a few parts per million to over 20 atomic percent. Such a large variation is somewhat worrisome as a large percentage of impurities could conceivably alter the properties of the Ta layers making comparison between samples prepared in different evaporations of questionable validity. In Figure 5.7 the resistivity is plotted as a function of Ta layer thickness for estimated impurity concentrations of less than 0.1%, between 0.1 and 1% and more than 1%. Although the scatter in the results makes the interpretation of this data ambiguous, it appears that samples with higher estimated concentrations of impurities have a higher resistivity. For this reason the following analysis focusses on those samples for which the impurity concentration is estimated to be less than a few percent.

It also appears that the resistivity increases as the Ta layers becomes thinner. The gradual upturn in the resistivity with decreasing Ta layer thickness is clearest in Figure 5.7(c) where ρ varies as $1/a_{Ta}$. There are two possible explanations - either the normal conductance is reduced in thinner layers or the quantum corrections to the conductivity vary with the layer thickness. Scattering of electrons from film surfaces (or interfaces) will degrade the normal conductivity. As the sample (or layer) thickness is reduced, the probability of surface scattering increases relative to the probability of collisions within the layer, with the result that the conductivity decreases. For an ordered film, where electrons have long mean free paths, this might occur at a thickness of several hundred angstroms, but for the samples in this study the critical thickness is of the order of a few angstroms. The normal conductivity is also affected by the degree of disorder (since the level of disorder determines l_o). As the layers are made thinner it is possible that they become more disordered. Quantum interference effects also depend on the film thickness and the degree of disorder via the phase breaking and elastic scattering rates. Unfortunately it is not possible to separate the variation in the normal conductance with

---

[29] Originally Read & Altman, 1965, found a TCR of ±100ppm·K^{-1} but Schwartz et al., 1972, showed that a positive TCR indicates the presence of some fraction of Ta in the bcc phase.

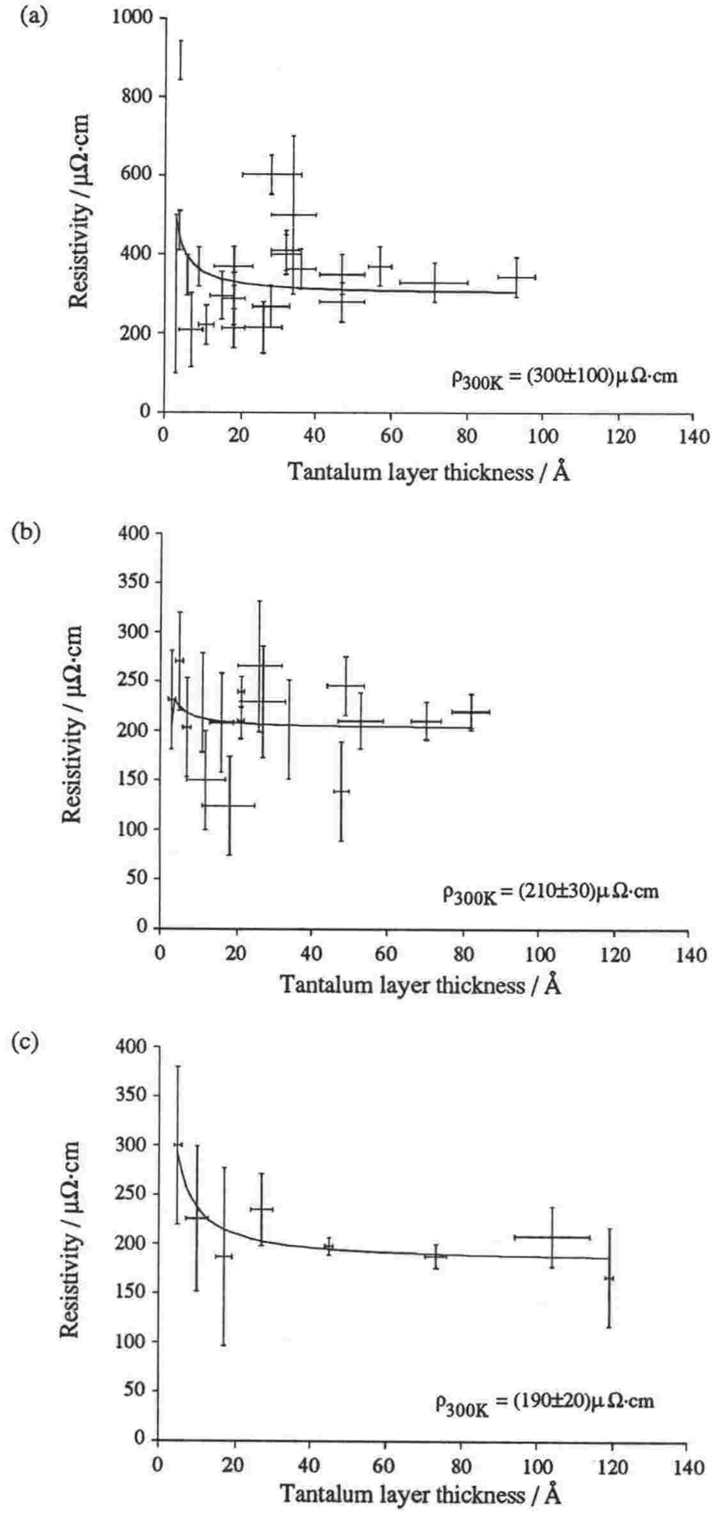

Figure 5.7 Room temperature resistivity as a function of Ta layer thickness and estimated impurity concentration (a) greater than 1% (b) between 0.1% and 1% and (c) less than 0.1%. Curves are fits to the data of the form $\rho \approx 1/a_{Ta}$.

layer thickness from that due to quantum interference effects from the resistance data alone.

Shown in Figure 5.8 is the room temperature coefficient of resistance,

$$\mathrm{TCR(300K)} = \frac{1}{R(300\mathrm{K})} \cdot \left.\frac{dR}{dT}\right|_{300\mathrm{K}}, \tag{5.41}$$

which shows a similar trend, that is, a gradual upturn with reducing Ta layer thickness. There is less scatter in this data because the calculation of the TCR does not require knowledge of the Ta layer thickness. Notice also that the TCR is slightly larger for samples with higher esimated impurity concentrations. The data show that the dependence on layer thickness cannot be attributed to surface scattering since surface scattering is a temperature independent scattering process to a first approximation, so that as the layers become thinner, and surface scattering becomes increasingly important, the TCR should tend towards zero.[30] This is clearly not so here and another explanation must be sought. In the theory of weak localisation, the TCR depends on the phase breaking rate. If the phase breaking rate is independent of the sample dimensions (as is the case for mechanisms in a three dimensional regime) then the TCR should also be independent of thickness. Conversely, a phase breaking rate which depends on the sample dimensions should give rise to a TCR which also depends on the sample dimensions.

5.2.4 High Temperature Results

In this section the high temperature (100-300K) results are discussed in terms of the theoretical predictions presented in Section 5.1. In this temperature range the measured conductivity increases with temperature. It will be assumed that the temperature dependence of the normal conductance is negligible compared to that of the quantum interference corrections. Spin-spin and spin-orbit scattering will be neglected since temperature dependent phase breaking mechanisms become much larger at high temperatures than these temperature independent mechanisms. Referring to Table 5.2, it can be seen that above 100K the electron-phonon scattering rates (either in the "clean" limit or from transverse modes in the "dirty" limit) far exceed those for electron-electron scattering. Note that interaction effects are not important at high temperatures.

It is not possible to determine the phase breaking rate and its temperature

---

[30] See for example Chopra, 1969.

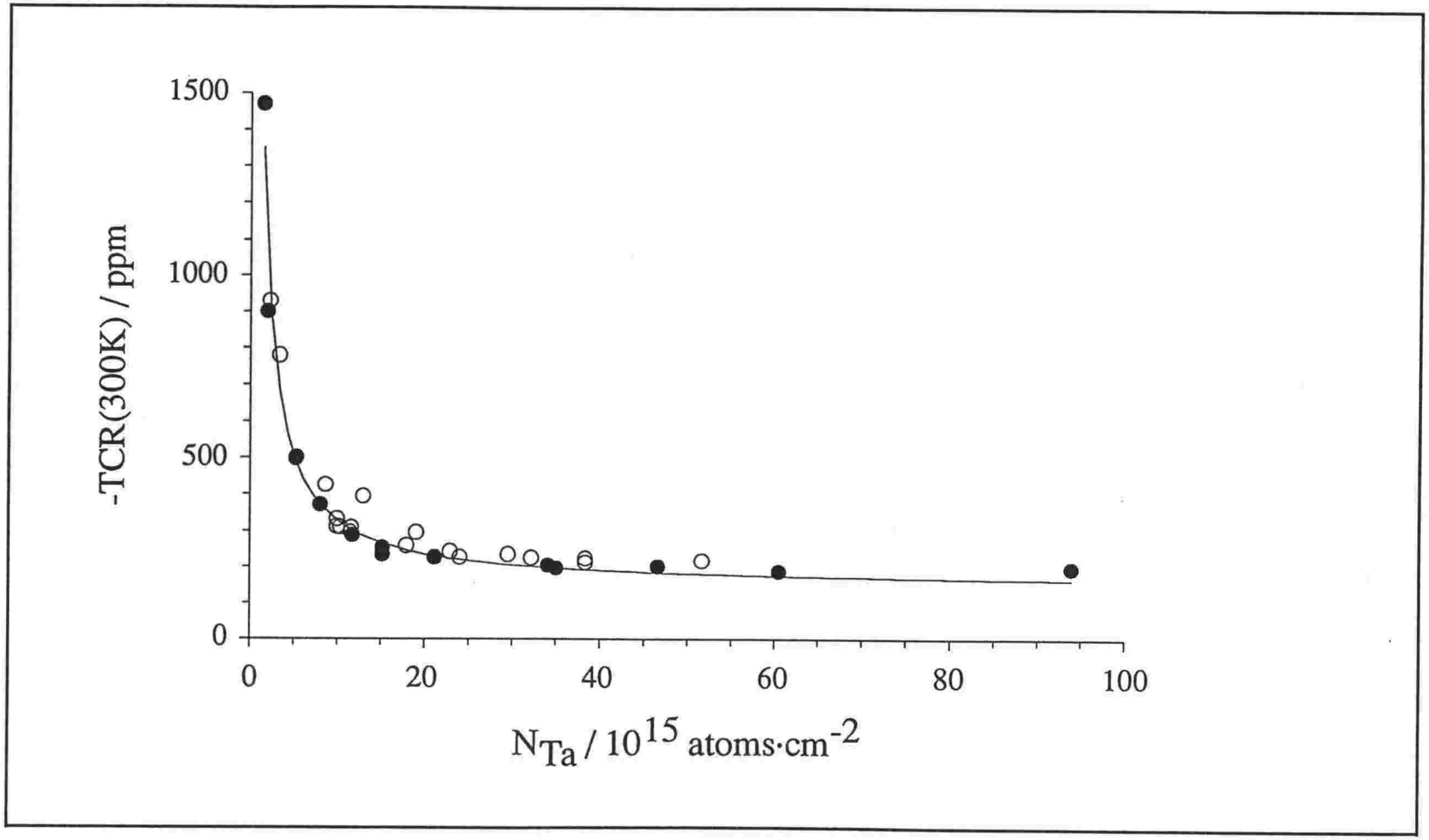

Figure 5.8 Temperature coefficient of resistance (TCR) at 300K. Solid symbols - samples with estimated impurity concentrations of less than 0.1%, open symbols - samples with estimated impurity concentrations of between 0.1 and 1%. Uncertainties in the data points are less than the size of the symbol. Solid curve is $\alpha_{300} \propto N_{Ta}^{-1}$ fitted to the solid symbols.

dependence unequivocally from the resistance data. However, by assuming a form for the temperature dependence of the phase breaking rate, and then assessing how well this rate describes the data, some progress may be possible. As a preliminary step the data were fitted to weak localisation theory, with a phase breaking rate given by Equation 5.18 (i.e. $\tau_\phi^{-1} = \beta T^p$) where β and p are allowed to vary. The data were not consistent with the logarithmic prediction for two dimensions (Equation 5.24) but the three dimensional square root prediction (Equation 5.26) fitted the data rather well. A selection of the fits to the data of the form

$$\frac{1}{R} = a + bT^{p/2}. \tag{5.42}$$

is shown in Figure 5.9. Figure 5.10 shows the difference between the fitted curve and the measured points for three different samples. There appears to be systematic variations of the fitted curve from the experimental points of the order of several hundred ppm as well as some scatter in this smooth variation of the order of 50ppm. The large scale variation suggests either that the true temperature dependence varies somewhat from that which has been assumed or that there are small thermal gradients between the samples and the thermometer. The small scale scatter is attributed to the limit of the accuracy of the resistance measurement (estimated in Chapter Four to be about ~~30~~75ppm). A number of parameters may be estimated from the fits. The quantity β/D , from which the diffusion length L_ϕ may be deduced, is calculated as

$$\frac{\beta}{D} = \left(\frac{b\ \ell/w}{n_{Ta}a_{Ta}L_\infty}\right)^2 = \frac{1}{L_\phi{}^2T^p} \tag{5.43}$$

where ℓ/w describes the dimensions of the resistance path and other symbols are as previously defined. The elastic mean free path l_o can be calculated from Equation 5.28 by taking the free electron value for k_F, and the average distance an electron travels between phase breaking events l_ϕ [31] may be estimated from $L_\phi = \frac{1}{2}\sqrt{l_\phi l_o}$. The results of the fits to all the samples with estimated impurity concentrations of less than a few percent are summarised in Table 5.4.

Are these results reasonable? The picture used to introduce weak localisation was of an electron diffusing through a disordered lattice via numerous elastic collisions with impurities. Every so often the electron suffers a phase destructive scattering event. Although the value of l_o given above is surprisingly small (less than the interatomic

---

[31] Note that, in contrast, L_ϕ is the average *displacement* of the electron between phase destructive scattering events.

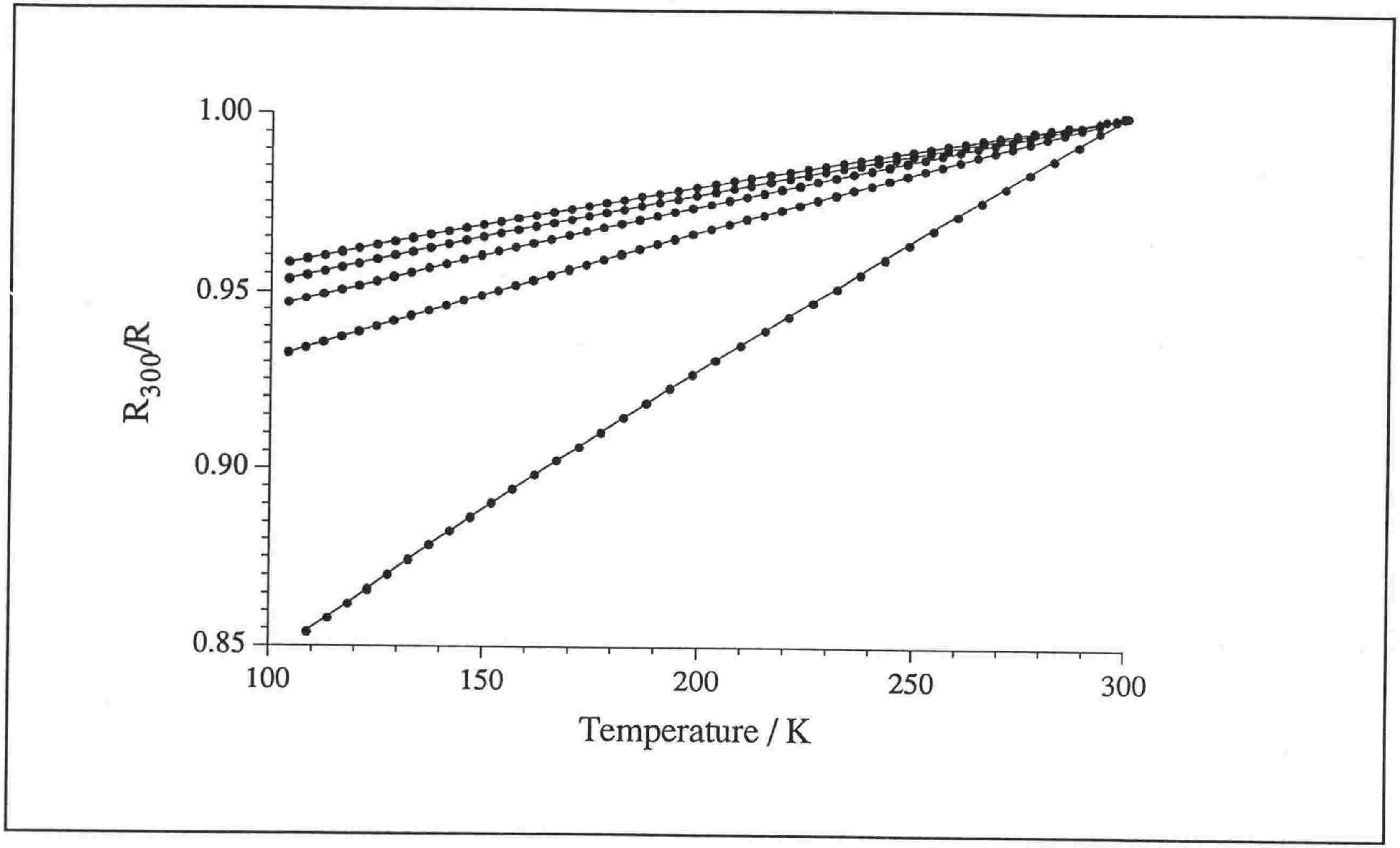

Figure 5.9 Raw data (normalised to 300K) fitted to Equation 5.42. Solid symbols are data points (only a few data points are shown for clarity) and solid lines are fitted curves. Ta layer thickness (top curve to bottom curve) in units of 10^{15} atoms·cm^{-2}: 46.6±0.9, 21.1±0.2, 17.9±0.2, 10.0±0.1 and 2.7±0.2.

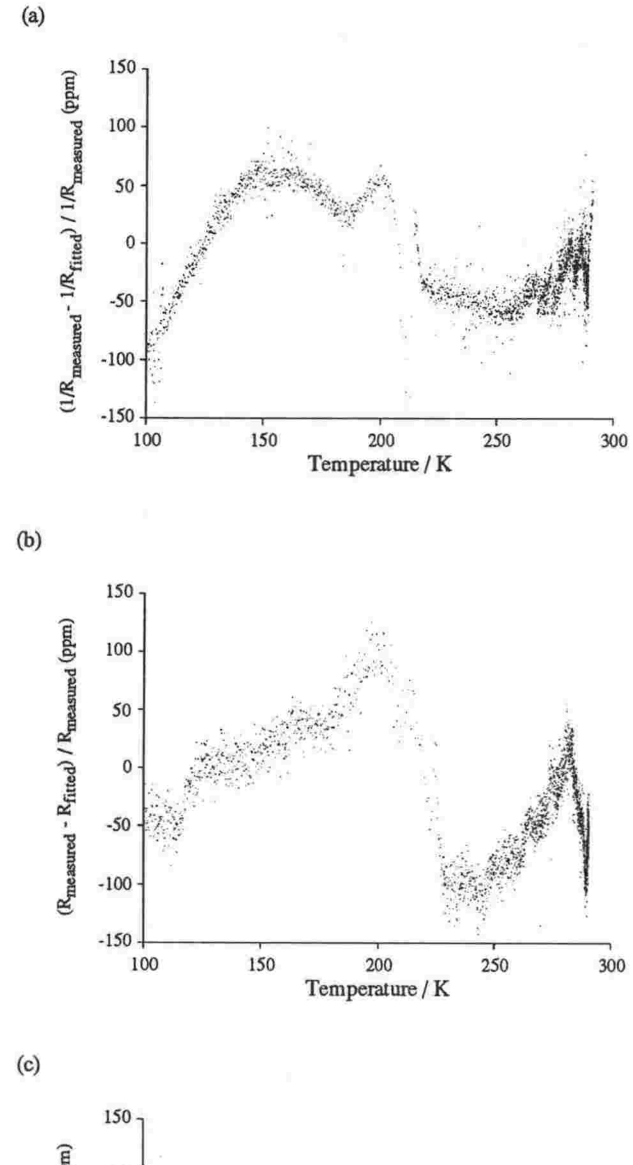

Figure 5.10 Deviation of measured high temperature resistance from fitted function $1/R = a + bT^{p/2}$ (that is, assuming a phase breaking rate $\tau_\phi^{-1} = \beta T^p$ within the theory of weak localisation) for three different samples: (a) 37/2G6, $N_{Ta} = (6.0\pm0.3)\text{x}10^{15}$ atoms·cm^{-2} (b) 36/1G3, $N_{Ta} = (11.5\pm0.5)\text{x}10^{15}$ atoms·cm^{-2} (c) 33/3G3, $N_{Ta} = (31\pm2)\text{x}10^{15}$ atoms·cm^{-2}.

Quantity		Value
p		1.6±0.2
β / D		$(0.8\pm0.2) \times 10^{15}$ $K^{-p}\cdot s^{-1}$
β	assuming $D = 1.2 \times 10^{-4}$ $m^{2}\cdot s^{-1}$	$(90\pm60) \times 10^{9}$ $K^{-p}\cdot s^{-1}$
L_ϕ	300K	(3±1) Å
	100K	(7±2) Å
l_o		~ 1.5 Å
l_ϕ	300K	~ 25 Å
	100K	~ 140 Å

Table 5.4 Summary of results from fitting data to Equation 5.42

spacing[32]), the distance travelled between phase destructive scattering events is much greater than that travelled between elastic scattering events as expected (that is, $l_o \ll l_\phi$). Furthermore, the calculated value of L_ϕ is consistent with the fact that three dimensional rather than two dimensional weak localisation predictions are found to give a better description of the resistivity data. The value found for p would appear to favour electron-electron scattering in the three dimensional regime as the phase destructive mechanism (see Table 5.2). The agreement must be coincidental however, as is is inconceivable that electron-electron scattering determines the high temperature dependence of the resistivity with no contribution from electron-phonon scattering. Moreover the measured value of β is many orders of magnitude larger than that predicted for electron-electron scattering in three dimensions.

The results given above were an average over many samples. A closer examination shows that p is a function of the Ta layer thickness (see Figure 5.11). The next step was

---

[32] The average interatomic spacing assuming a density of 16.6g·cm^{-3} is approximately 2.6Å. The density of the Ta in this study is likely to be less than this value giving an even larger interatomic spacing.

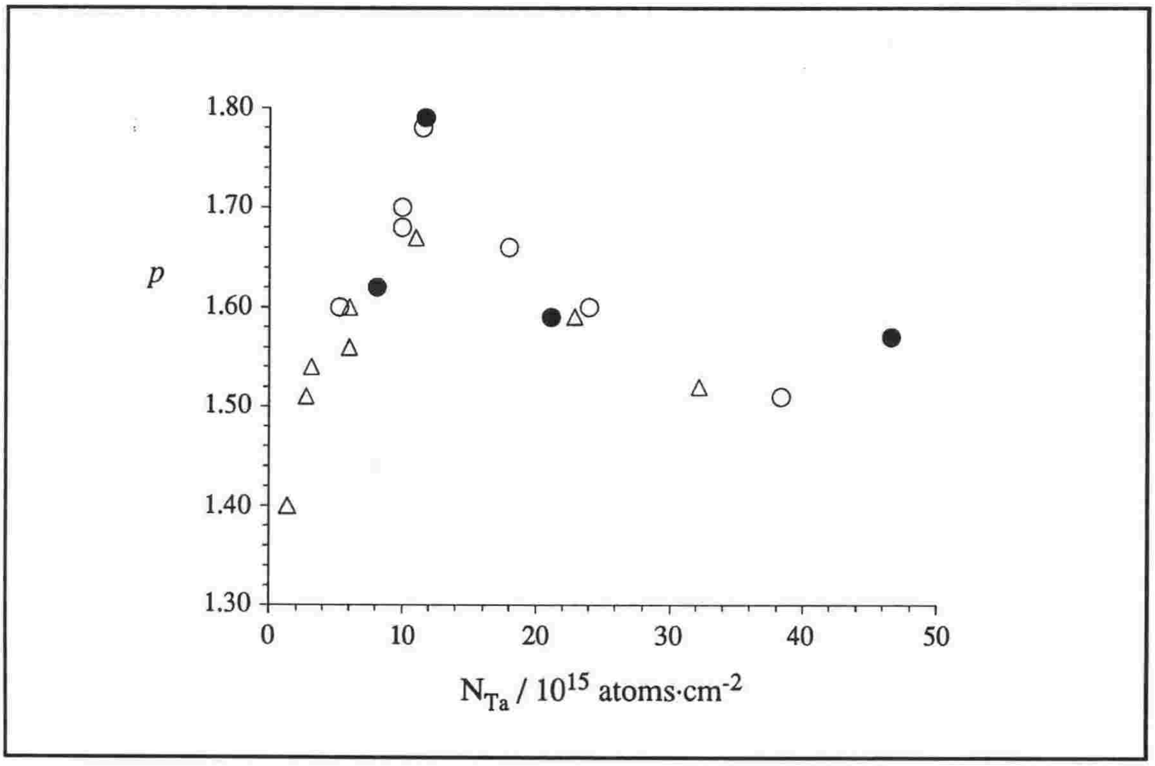

Figure 5.11 Value of p (the temperature exponent of the phase breaking rate) deduced from fits to data 100-300K for samples with estimated impurity concentrations of less than 0.1% (solid symbols), between 0.1 and 1% (open circles) and more than 1% (open triangles). Uncertainties are of the order of the size of the symbol.

to try fitting the results assuming that the phase breaking rate is governed by a combination of two mechanisms with different dependences on temperature and possibly also on the Ta layer thickness. Since p~1.6 phase breaking rates combining the T dependence of the phase breaking rate due to electron-phonon scattering in the "clean" limit and the T^2 dependence due to scattering from transverse phonons in the "dirty" limit are plausible although there is no special justification for combining the rates in this manner.

Setting $\tau_\phi^{-1} = \tau_{\phi,1}^{-1} + \tau_{\phi,2}^{-1}$ where $\tau_{\phi,1}^{-1} = \gamma T$ and $\tau_{\phi,2}^{-1} = \eta T^2$ and again fitting the data to Equation 5.26 (that is, the three dimensional weak localisation prediction) gives equally good fits to the data as the previous fits where the phase breaking rate was taken as $\tau_\phi^{-1} = \beta T^p$ (compare Figures 5.10 and 5.12). Values of the "clean" and "dirty" scattering rates deduced from the fits are shown in Figure 5.13.

Both the "dirty" electron-phonon scattering rate from transverse phonons and the "clean" electron-phonon scattering rate appear to vary approximately linearly with N_{Ta}^{-1} for layers thicker than ~10Å. The scattering rates are of the order of 1-2 x 10^{15} s^{-1} at

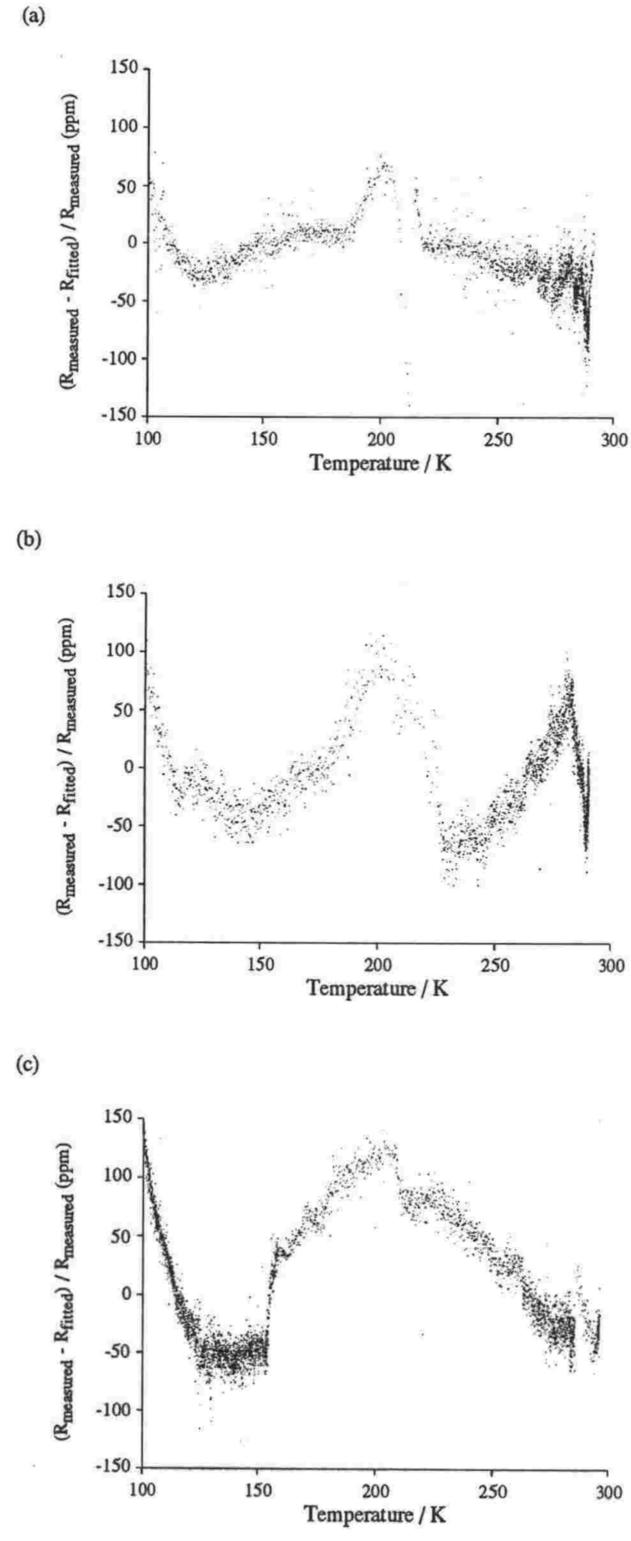

Figure 5.12 Deviation of measured high temperature resistance from fitted function $1/R = a + b\sqrt{cT+T^2}$ (that is, assuming a phase breaking rate $\tau_\phi^{-1} = \gamma T + \eta T^2$ within weak localisation theory) for three different samples: (a) 37/2G6, $N_{Ta} = (6.0\pm0.3)\text{x}10^{15}$ atoms·cm^{-2} (b) 36/1G3, $N_{Ta} = (11.5\pm0.5)\text{x}10^{15}$ atoms·cm^{-2} (c) 33/3G3, $N_{Ta} = (31\pm2)\text{x}10^{15}$ atoms·cm^{-2}.

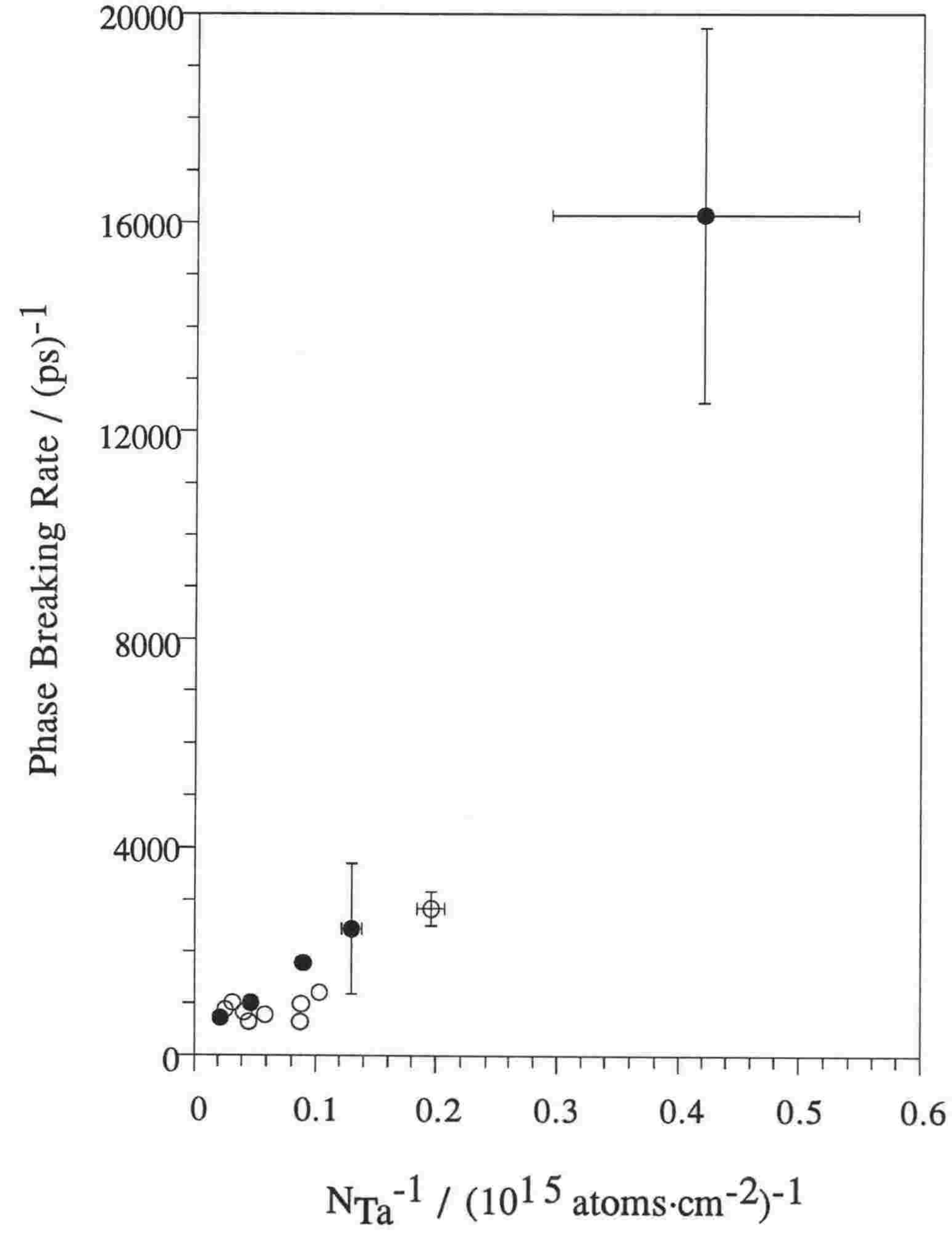

Figure 5.13a "Clean" electron-phonon scattering rate from transverse phonons $\tau_{\phi,1}^{-1} = \gamma T$ at T = 300K. Solids symbols correspond to samples with estimated impurity concentrations of less than 0.1% and open symbols to samples with estimated impurity concentrations of between 0.1 and 1%.

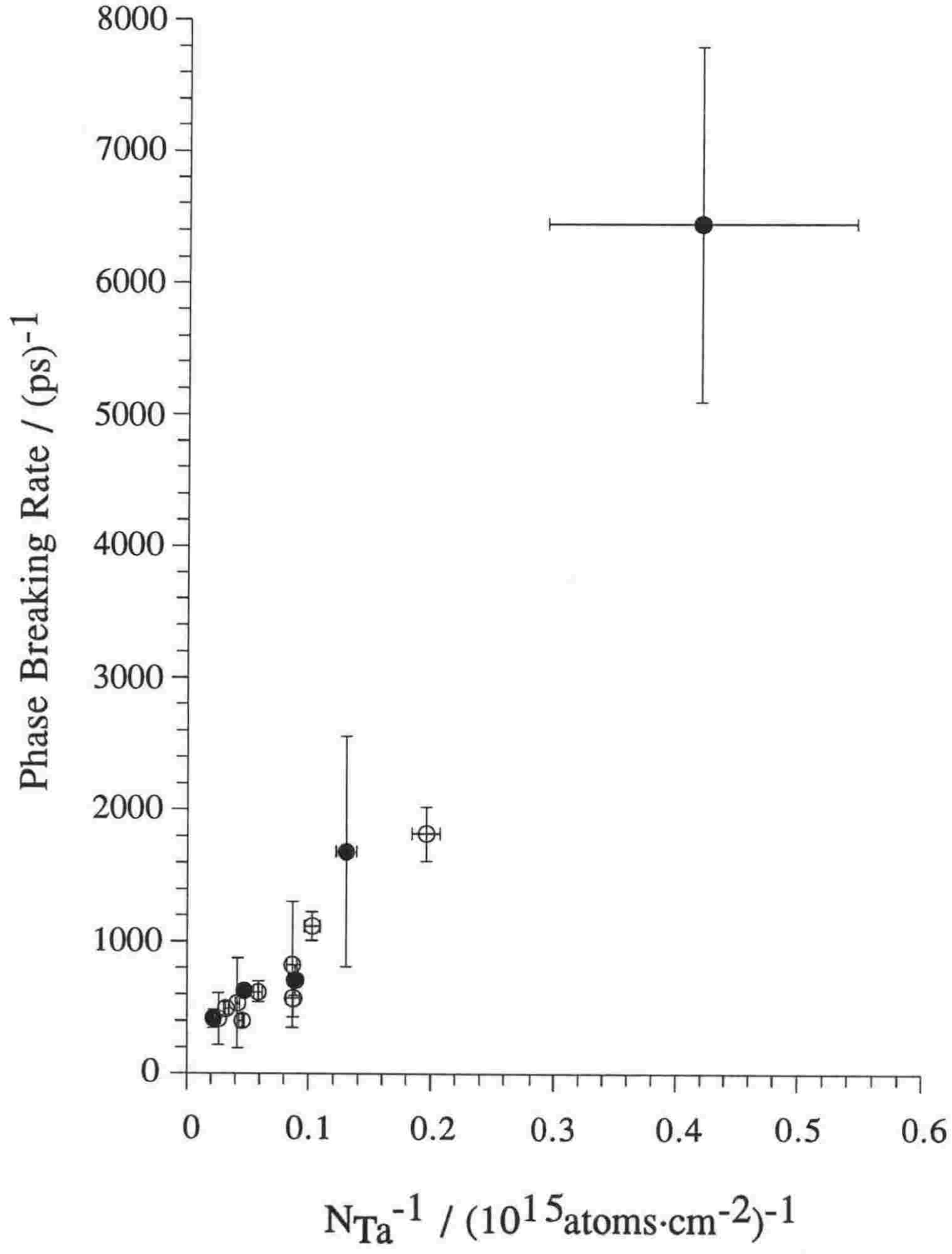

Figure 5.13b "Dirty" electron-phonon scattering rate from transverse phonons $\tau_{\phi,2}^{-1} = \eta T^2$ at T = 300K. Solids symbols correspond to samples with estimated impurity concentrations of less than 0.1% and open symbols to samples with estimated impurity concentrations of between 0.1 and 1%.

300K agreeing well with the predicted values (see Table 5.2). The variation with N_{Ta}^{-1} (or equivalently a_{Ta}) is a little puzzling however. The "dirty" electron-phonon scattering rate from transverse phonon modes given by Equation 5.12b is independent of the sample size. It does however depend on the degree of disorder via the total scattering length l as does the "clean" electron-phonon scattering rate. Referring to Figure 5.7 we see that $\rho_{300} \approx a_{Ta}^{-1}$ and since $a_{Ta} \propto N_{Ta}$ we find $l \propto N_{Ta}$ provided $\rho_{300} \propto l^{-1}$ and hence we might expect $\tau_{\text{el-phT}}^{-1} \propto N_{Ta}^{-1}$ as observed. It should be noted that the diffusion constant D has been set equal to the free electron value in order to calculate the phase breaking rate. Such a procedure is not strictly valid and may account for some of the variation of the calculated scattering rates with layer thickness.

For layers thinner than ~10Å the scattering rates increase rapidly. Although the functional form predicted for weak localisation in three dimensions fits the variation of the resistance as a function of temperature for these very thin layers, the condition $L_\phi \ll a_{Ta}$ is not well satisfied. The explanation for the abrupt change in the behaviour as a_{Ta} is made smaller than ~10Å may simply be the result of the weak localisation correction entering a regime which is neither two nor three dimensional. Alternatively it is possible that the very thinnest layers are not continuous although the measured conductivity is not consistent with hopping between islands or clusters of Ta atoms.

Note that the description of the variation of the two phase breaking mechanisms can also explain the variation of p with N_{Ta} shown in Figure 5.11.

The theory of quantum interference effects assumes "s"-band conduction. In transition metals such as Ta, "d"- band conduction may also be important. In the case of crystalline transition metals the effective mass of electrons in the "d"-band is much larger than that in the "s"-band so that "d"-band electrons do not contribute significantly to the conductivity. It has been argued that when the mean free path of the "s" electrons becomes very short (as is the case in disordered metals) the "s" and "d"-band conductivities may become comparable in magnitude. If this is the case then the conduction may be best described by a two band model with a conductivity $\sigma = \sigma_s + \sigma_d$. If both σ_s and σ_d are described by Equation 5.26 (three dimensional weak localisation correction) but with a different phase breaking rate for each band then the conductivity should depend on temperature as $\sigma = a + bT^{p/2} + cT^{q/2}$ where a, b, c, p, and q are constants. The conductivity of the multilayers is described reasonably well by such a temperature relation with $p = 1$ and $q = 2$ although the single band models discussed above fit the data better.

To conclude, the high temperature resistivity of the Ta layers can be described by weak localisation theory. The phase breaking rate deduced from the resistivity data depends on the layer thickness and has a temperature dependence lying between T and T^2.

5.2.4 Low Temperature Results

Now let us turn to the low temperature behaviour of the resistance above the superconducting transition. At low temperatures conduction by "d"-band electrons is not expected to significantly effect the temperature dependence of the conductivity. This is because the temperature dependence of the "d"-band conductivity results from thermal smearing of the "d"-band density of states and thermal expansion effects, both of which will be negligible at low temperatures (see Howson and Gallagher, 1988). However, quantum interference effects (including spin-orbit and possibly spin-spin scattering) interaction effects and superconducting fluctuations are all likely to be important at low temperatures. The resistivity data cannot be interpreted by treating the unknown parameters in the theoretical predictions as fitting parameters because they are simply too numerous. Instead, a number of simplifications must first be made.

By writing the phase breaking rate as $\tau_\phi^{-1} = \beta T^p$ and assuming spin-spin scattering is negligible, Equation 5.24, giving the quantum interference correction to the conductance per square in two dimensions, reduces to

$$\delta\sigma_2^{QI} = \alpha_{QI}\frac{e^2}{2\pi^2\hbar}lnT + const. \tag{5.44}$$

where $\alpha_{QI} = p$ for weak spin-orbit scattering and $\alpha_{QI} = -p/2$ in the limit of strong spin-orbit scattering. Abrikosov and Gorkov, 1962, predict that the the spin-orbit scattering rate in a metal should vary as

$$\tau_{so}^{-1} = \tau_o^{-1}\,(\alpha_{FS}Z)^4 \tag{5.45}$$

(where α_{FS} is the fine structure constant and Z the atomic number) and this value is often quoted in relation to the weak antilocalisation correction to the conductivity[33]. Hickey et al., 1986, however point out that this calculation is only first order in the interaction and as such ignores that part of the spin-orbit interaction that causes spin-flip. Since the spin-orbit scattering rate entering localisation theory is the spin-flip scattering rate due to spin-orbit interaction, they argue that a second order calculation is required and therefore (in a free electron estimate) $\tau_{so}^{-1} \propto Z^8$ in the context of weak localisation theory. They note however that the spin-orbit interaction is sensitive to the exact electronic structure and there is therefore considerable doubt about the applicability of a free electron estimate. Notwithstanding these objections we note that Ta has a high atomic number so spin-orbit scattering should be strong in our samples.

---

[33] See for example Gershenzon et al., 1982, McGinnis & Chaikin, 1985, Santhanam et al., 1987, and Meikap et al., 1993.

In two dimensions, interaction effects in the diffusion channel also give a logarithmic correction to the conductivity, that is,

$$\delta\sigma_2{}^D = \alpha_D \frac{e^2}{2\pi^2\hbar} lnT + const. \tag{5.46}$$

where $\alpha_D = \frac{1}{2}\lambda_2$ (see Equation 5.33). The value of α_D, estimated from free electron theory, is 0.70 (see Table 5.3).

If superconducting fluctuations and interaction in the Cooper channel can be ignored then the conductivity of a purely two-dimensional sample will vary logarithmically with temperature. The total temperature dependent correction to the conductivity may be written

$$\delta\sigma_2(T) = \alpha \frac{e^2}{2\pi^2\hbar} lnT \tag{5.47}$$

where $\alpha = \alpha_D$ if interaction effects determine the correction to the conductivity, $\alpha = \alpha_{QI}$ if quantum interference effects dominate and $\alpha = \alpha_D + \alpha_{QI}$ if both are important.

Two regions of approximately logarithmic behaviour are seen in the conductivity of the multilayers. These regions are shown schematically in Figure 5.14 below. The first region (region I) is seen for thin Ta layers between about 2 and 5K. In this region, the resistance increases as the temperature is lowered, that is $\alpha > 0$. In the second region (region II), which is seen for thicker layers between 5 and 15K, the resistance decreases as the temperature is lowered, that is $\alpha < 0$.

Values of the coefficients of logarithmic variation α from fits similar to those shown in Figure 5.15 are listed in Table 5.5. Note that knowledge of the Ta layer thickness is not required for the determination of α so that α may be determined with some precision. The measured values of α vary with Ta layer thickness but in all cases they are of the same order of magnitude as the theoretical predictions. In region II the measured values of α range from -0.8 for the very thickest layers to -0.2 for samples with Ta layers of the order of 25Å. For samples with thinner Ta layers, logarithmic behaviour of the conductivity is not seen in region II. In region I, α decreases from 0.8 for the very thinnest layers to 0.3 for Ta layers of thickness ~ 25Å. These results can be interpreted in the following manner.

For the thickest Ta layers, electron-electron interactions are in a three dimensional regime and hence rather weak. In addition electron-electron interaction becomes less important as the temperature is raised. Thus in region II quantum interference effects

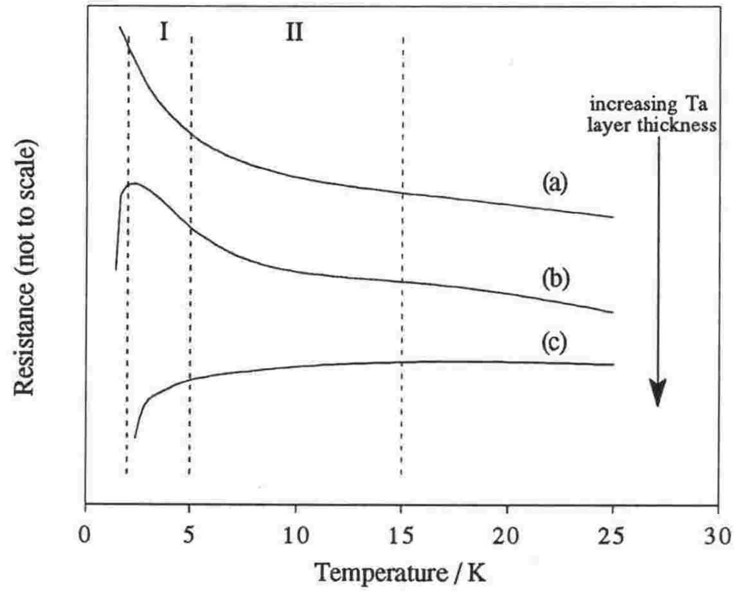

Figure 5.14 Schematic representation of the low temperature resistivity as the Ta layer thickness is varied. Thin layers - curves (a) and (b) - show logarithmic behaviour of the conductivity with a negative TCR in region I, while thicker layers - curve (c) - show logarithmic behaviour of the conductivity in region II.

determine the temperature dependence of the conductivity. The value of α measured for thicker layers lies in the region -0.7 to -0.8 suggesting that spin-orbit scattering is strong and that $p = 1.5$, that is the phase breaking mechanism is electron-electron scattering in a three dimensional regime.

As the Ta layers are made thinner the layer thickness becomes comparable with the diffusion length L_T and both electron-electron scattering and electron-electron interaction approach a two-dimensional regime. The expected value of α is now given by $\alpha = -p/2 + 0.67 = 0.17$. While the magnitude of α certainly decreases for thinner layers, α does not tend towards 0.17 in the limit of thin layers. In fact the logarithmic behaviour of the conductivity in region II disappears. However, the conductivity of thin Ta layers varies logarithmically with temperature in region I with α increasing from 0.3 to 0.8 as the layer thickness is reduced. These values of α could be due to either electron-electron interaction alone, or both electron-electron interaction and quantum interference effects. Note that $x = 2k_F/\kappa$ must be positive so that in the free electron model, the screening factor F must lie between 0 and 1 (see Equation 5.33). Allowed

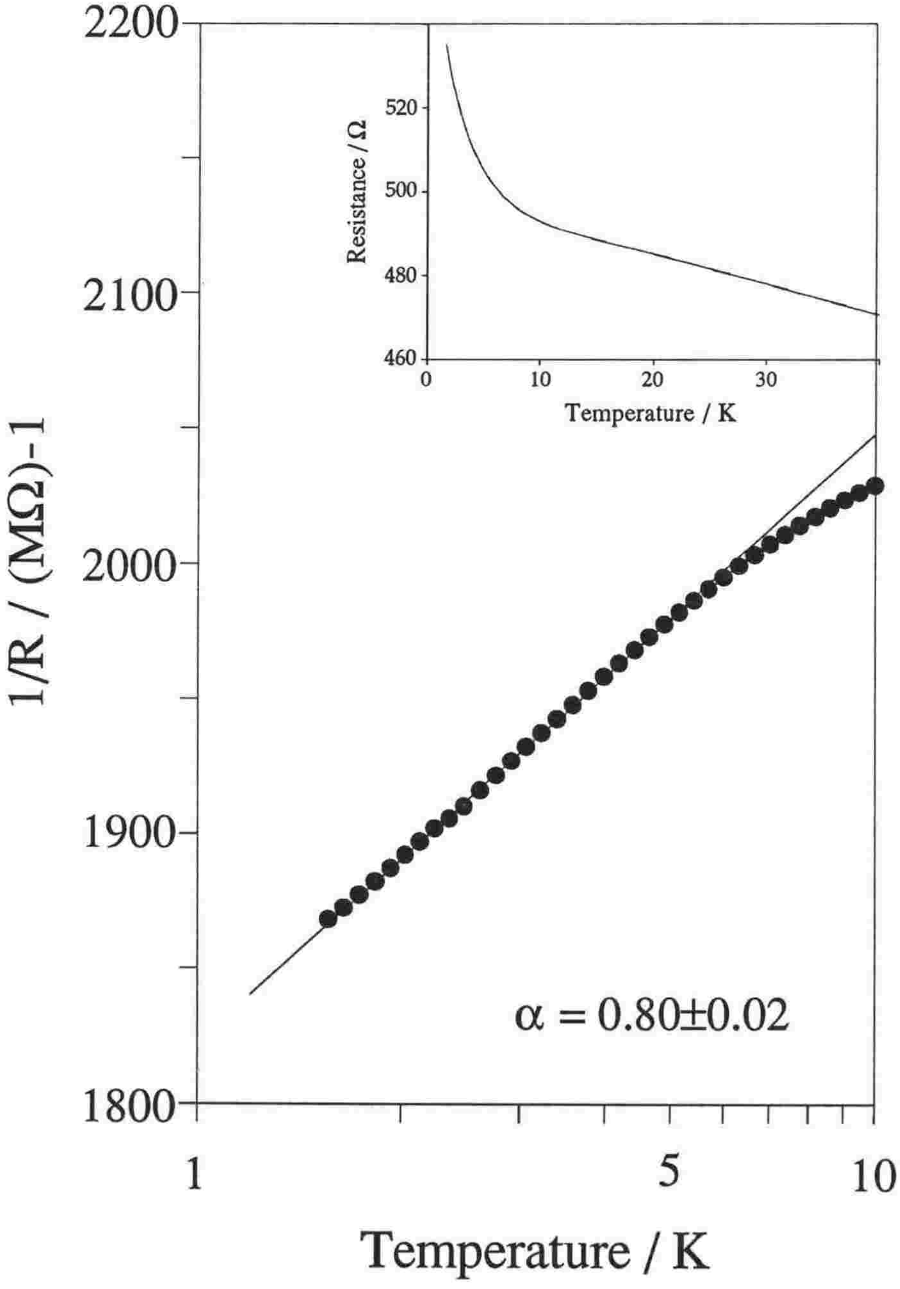

Figure 5.15a Low temperature region of logarithmic variation of the conductivity for a sample with thin Ta layers (sample 50/3G6, $N_{\mathrm{Ta}} \sim 2.5 \times 10^{15}$ atoms·cm^{-2}). Experimental points are shown as solid symbols (only a few data points are shown for clarity) and the logarithmic fit as a solid line. Deviations from logarithmic behaviour are evident below 2K and above 5K. Inset shows resistance as a function of temperature (experimental points) for reference.

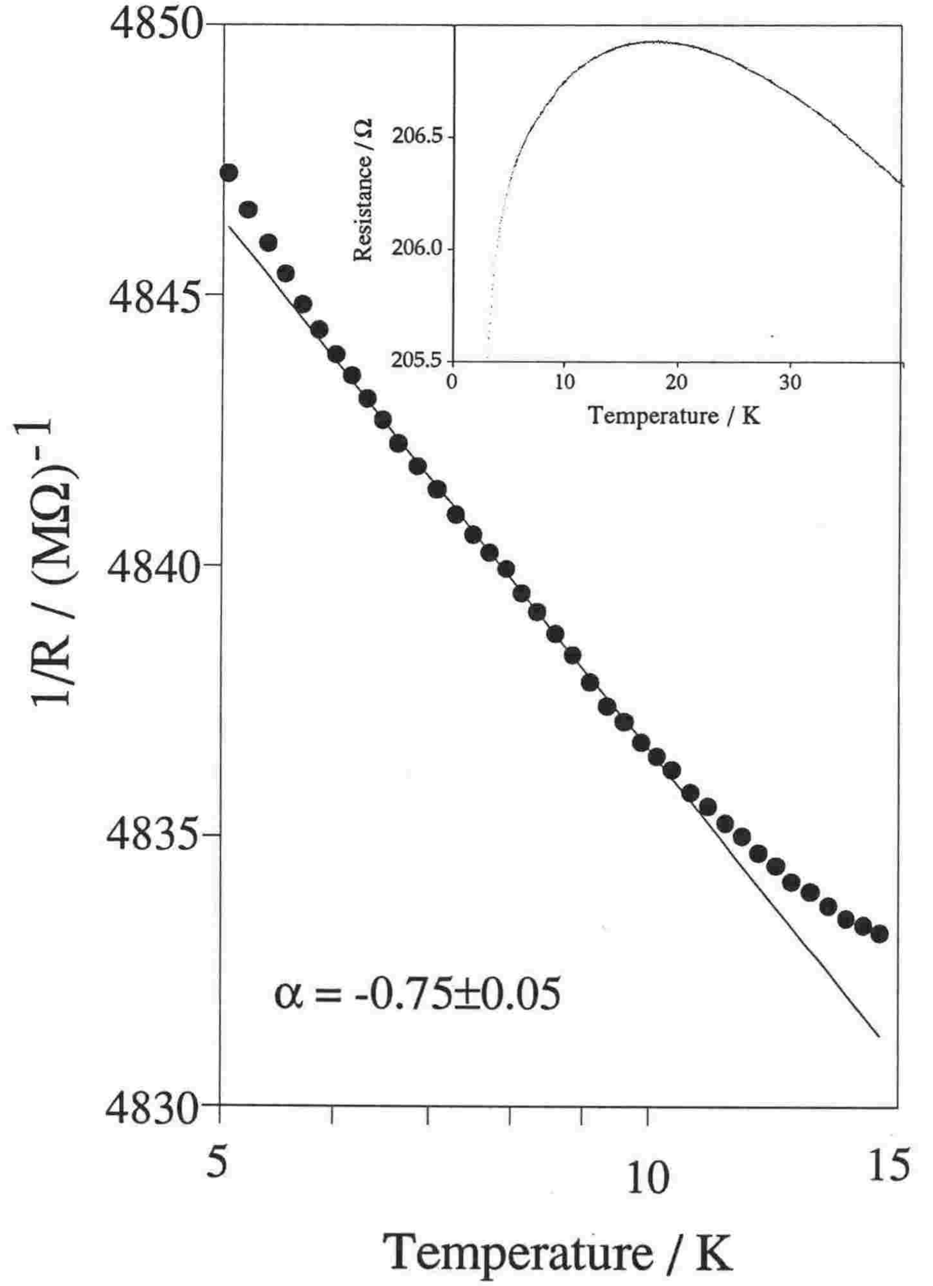

Figure 5.15b Low temperature region of logarithmic variation of the conductivity for a sample with thick Ta layers (sample 33/3G3, N_{Ta} = (31±2) x 10^{15} atoms·cm^{-2}). Experimental points are shown as solid symbols (only a few data points are shown for clarity) and the logarithmic fit as a solid line. Deviations from logarithmic behaviour are evident below 6K and above 10K. Inset shows resistance as a function of temperature (experimental points) for reference.

Sample	N_{Ta}	α	
	10^{15} atoms·cm^{-2}	Region I	Region II
50/3G6	~2.5	0.80±0.02	-
37/1G6	2.7±0.2	0.80±0.03	-
21/3G5	3.3±0.2	0.50±0.02	-
43/2G6*	4.0±0.4	0.35±0.01	-
32/1G3	4.6±0.3	0.46±0.02	-
28/1G3	5.1±0.3	0.41±0.02	-
29/1G3	5.1±0.3	0.39±0.02	-
37/2G6	6.0±0.3	0.35±0.02	-
29/3G6	11.2±0.7	-	-0.20±0.05
36/1G3	11.5±0.5	0.33±0.02	-
33/1G3	11.6±0.7	0.31±0.02	-
28/3G6	17±1		-0.34±0.05
30/1G6	21±1		-0.23±0.03
33/2G3	22±1		-0.46±0.03
33/3G3	31±2		-0.75±0.05
30/2G6	33±2		-0.84±0.05
18/1G2	35±2		-0.6±0.1
30/3G6	46±3		-0.84±0.08
18/2G2	60±4		-0.7±0.1

Table 5.5 Values of the coefficients of logarithmic variation α at low temperature (see Equation 5.47).

values for α_D therefore lie in the range 0.35 to 1. Ascribing the behaviour of the conductivity in region I to electron-electron interaction alone, implies that the strength of interaction increases as the layers become thinner (and hence fully two-dimensional) as expected. The value of α_D is in reasonable agreement with the predicted free electron value. Why the temperature dependence due to quantum interference effects should no longer be evident, however, is not clear. If, on the other hand, both electron-electron interaction and quantum interference effects determine the value of α, then assuming spin-orbit scattering is strong, and the phase breaking mechanism is two-dimensional electron-electron scattering, (that is, $p = 1$) then $\alpha_{QI} = 1/2$ and $0.8 < \alpha_D < 1.3$. Such an interpretation therefore requires unphysical values of α_D. (Note that assuming $p > 1$ requires even larger values of α_D). Moreover electron-electron scattering is predicted to be the dominant scattering mechanism at low temperatures (see Table 5.2). It is not possible to separate the contribution to the logarithmic dependence resulting from quantum interference effects from that due to interaction effects from the resistance data alone.

Fitting the measured conductance to a logarithmic variation as a function of temperature gives qualitative information about the conduction processes. We have found that electron-electron interaction effects lie in a two-dimensional regime for the thinnest layers crossing over to a three dimensional regime for thicker layers, that spin-orbit scattering is strong and that the *temperature dependence* of the phase breaking rate at low temperature is consistent with electron-electron scattering as the dominant mechanism. To determine the magnitude of the various scattering rates, we turn to the exact relation for the conductivity. Unfortunately, even when fitting the full theoretical predictions to the data there is considerable ambiguity in determining each required parameter independently. In order to avoid regions where the Ta layer thicknesses are neither fully two nor three dimensional with respect to electron-electron effects (that is regions where $a_{Ta} \sim L_T$) only the thickest Ta layers are studied. Moreover, only temperatures above 10K are considered in an attempt to exclude regions where superconducting fluctuations and electron-electron interaction effects dominate. It is then possible that quantum interference effects alone determine the variation of the conductivity with temperature. The high temperature results suggest that the phase breaking length, L_ϕ, which determines the dimensionality with respect to quantum interference effects, is of the order of 10-80Å between 10 and 30K (see Table 5.4). However, owing to the importance of electron-electron scattering at low temperature the phase breaking rate is expected to increase more rapidly at lower temperatures than this simple extrapolation would imply (see Table 5.2), and L_ϕ may be somewhat smaller as a consequence. The question of the dimensionality is left open and the conductivity data fitted in terms of quantum interference effects firstly in two dimensions, and secondly in three dimensions, assuming in each case that spin-spin scattering may be neglected.

For two-dimensional quantum interference effects the total resistance is related to the temperature as

$$\frac{1}{R} = a + b\left[\frac{3}{2}\ ln\left(1 + \frac{4}{3}cT^p\right) - \frac{p}{2}\ lnT\right] \tag{5.48}$$

(see Equation 5.24) where $b = nwL_{oo}/\ell$, $c = \beta/\tau_{so}{}^{-1}$ and a is treated as a free fitting parameter. Note that β and τ_{so}^{-1} are not determined independently. A first estimate for c may be made from the position of the minimum in the conductance. To ensure b is approximately equal to the expected value it proved necessary to set p equal to 2.5±0.1. The fitted values of c were then of the order of $3\text{x}10^{-4}$. The temperature dependence of the deduced phase breaking rate cannot be explained in terms of the models presented in Section 5.1.3.

The expression for quantum interference effects for three dimensional samples (Equation 5.26) may be rewritten as

$$\frac{1}{R} = a + b\left[3\sqrt{\frac{1}{c} + \frac{1}{4}T^{p}} - \frac{1}{2}T^{p/2}\right] \tag{5.49}$$

by taking $\tau_{\phi}^{-1} = \beta T^{p}$ and $\tau_{s}^{-1} = 0$. Here $b' = nwa_{Ta}\sqrt{\beta / D}L_{oo} / \ell$, and c and a are as before. Note that in this case τ_{so}^{-1} and β may be determined independently provided the diffusion coefficient is known. The data were best fitted by setting p to 1.5±0.2. Values deduced by fitting Equation 5.49 to the measured data for sample 30/3G6 are given in Table 5.6 and the experimental data and fitted curve are shown in Figure 5.16b.

Fitting Parameters	b'	$1.4\text{x}10^{-5}\ \Omega\cdot\text{K}^{-3/4}$
	c	$6.6\text{x}10^{-3}\ \text{K}^{-3/4}$
	p	1.5
Calculated Values	$\sqrt{\beta / D}$	$(1.1\pm0.1)\text{x}10^{8}\ \text{m}^{-1}\cdot\text{K}^{-3/4}$
	L_{ϕ}	$(97\pm9)T^{-5/2}$ Å
	β (assuming $D = 1.2\text{x}10^{-4}\ \text{m}^{2}\cdot\text{s}^{-1}$)	$1.5\text{x}10^{12}\ \text{s}^{-1}\cdot\text{K}^{-3/2}$
	$\tau_{so}^{-1} = \beta / c$	$2\text{x}10^{14}\text{s}^{-1}$

Table 5.6 Values of conduction parameters deduced from fits to three dimensional quantum interference theory for low temperature resistance data (10-30K) for sample 30/3G6.

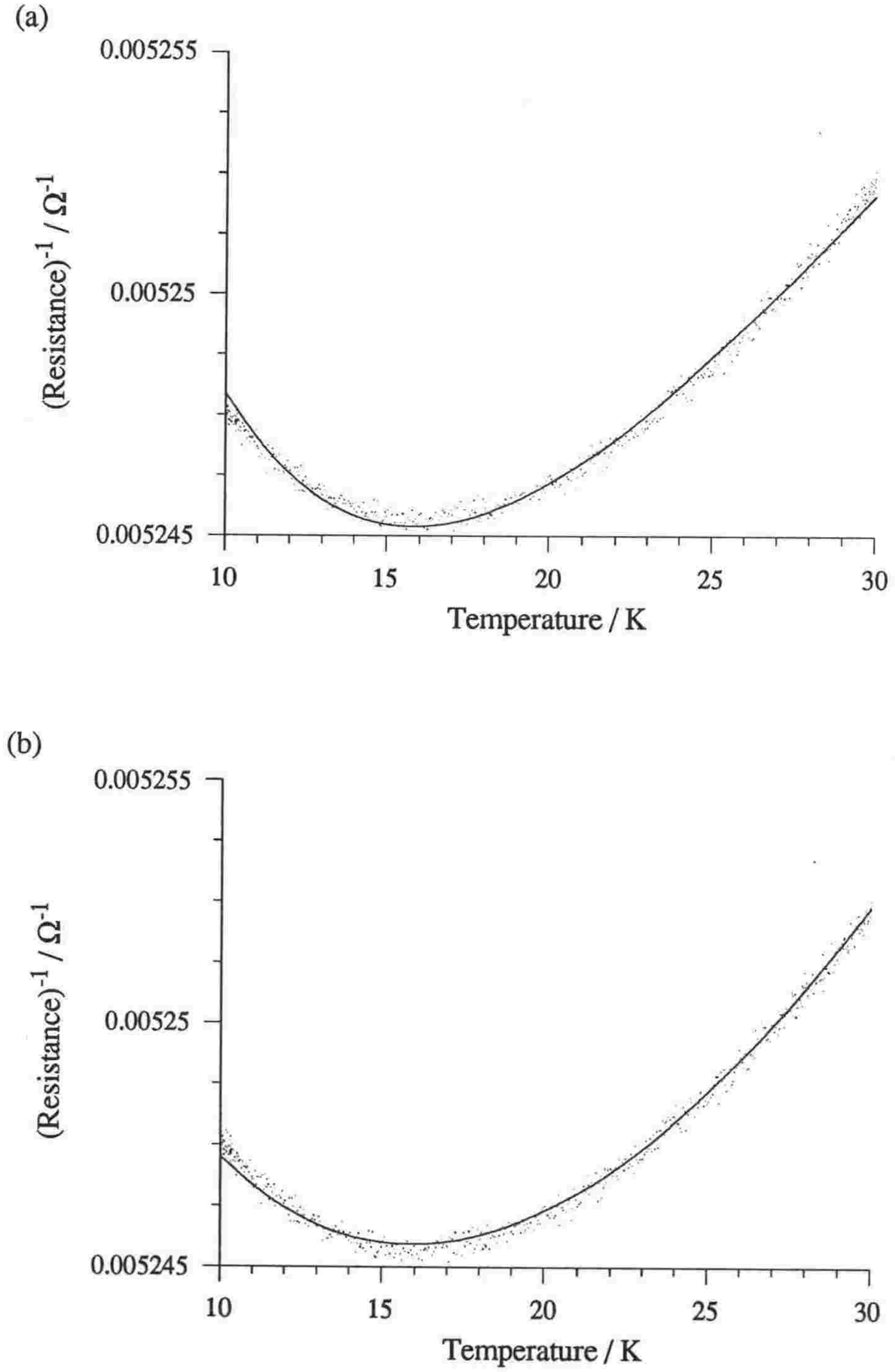

Figure 5.16 Low temperature data (sample 30/3G6) fitted to weak localisation theory including spin-orbit scattering. Fit to (a) two dimensional prediction and (b) three dimensional prediction. Theoretical curves shown as solid lines and experimental points as dots.

The curve fitted to the theory in two-dimensions (Equation 5.48) is shown for comparison. Both curves give a reasonable description of the data. The phase breaking length calculated from the fitting parameters is of the order of 10-20Å suggesting samples in the temperature range 10-30K with layers thicker than 70Å should be more nearly three than two dimensional. By taking the free electron value for the diffusion constant, β and τ_{so}^{-1} may be estimated. The spin-orbit scattering rate is of the same order of magnitude as the value deduced from Equation 5.45 but the value of β is orders of magnitude larger than expected from Equation 5.16 or indeed any of the predictions for the phase breaking rate discussed in Section 5.1.3. We feel that the most likely cause of these discrepancies is the fact that we have ignored superconducting fluctuations (Equation 5.36). An order of magnitude estimate of the correction to the conductivity from superconducting fluctuations suggests that the correction will be significant particularly on the low temperature side of the fitting region. However, without knowledge of the superconducting transition temperature it was not possible to fit the data to a combination of weak localisation corrections (including spin-orbit scattering) and superconducting fluctuation corrections.

5.2.5 Conclusion

To conclude this section on the interpretation of the resistance of the multilayers we make the following observations. The variation of the resistance as a function of temperature as well as Ta layer thickness can be understood in terms of the theory of quantum interference at defects together with the enhancement of the electron-electron interaction in disordered media. At high temperatures quantum interference effects dominate and the resistance increases as the temperature is lowered in complete contrast to the resistance of ordered Ta. At low temperatures the phase breaking rate governing the quantum interference correction decays to reveal the effect of spin-orbit scattering and causing a maximum to appear in the resistance between 15-20K. At still lower temperatures the interaction between electrons begins to affect the resistance. For thick three dimensional layers the effect is rather small but as the layer thickness is decreased and screening of the interaction is confined to a two dimensional plane, interaction between electrons causes a rapid increase in the resistance.

Quantitative analysis, although complicated by the number of competing conduction mechanisms and the fact that many samples were neither fully two nor three dimensional, has yielded some interesting results. At high temperatures the phase breaking rate appears to be dominated by electron-phonon scattering with a temperature dependence which lies between the "clean" and "dirty" limits. At low temperatures the origin of phase destructive events is not so clear. While the temperature dependence of the phase breaking rate would seem to point to electron-electron scattering as the underlying mechanism, the magnitude is much larger than current theories predict. The magnitude of the correction to the resistance for thin two-dimensional layers due to electron-electron interactions however is comparable with theoretical predictions. As expected the electron-electron interaction correction for thicker layers was too small to be separated from other effects.

Chapter Six

Superconductivity

The resistance of all the samples in the present study, with the exception of those with very thin Ta layers, shows a sharp drop at temperatures below 2K associated with the onset of superconductivity. Preliminary measurements suggest that Ta/Ge multilayers hold considerable promise as a system for investigating both the interplay between superconductivity and localisation, and superconductivity in layered materials.

A particularly interesting question has arisen recently relating to the interplay between localisation, which confines electrons to small regions of space, and superconductivity, which is characterised by correlations between electrons over large distances. A superconductor to insulator transition at $T = 0$ is predicted to occur when the normal state sheet resistance has a universal value of the order of the quantum resistance for paired electrons $R_Q = h/(2e)^2 \approx 6.45\mathrm{k}\Omega/\square$. Measurements of homogeneous thin films of lead and bismuth films by Haviland et al, 1989, have raised the possibility that the threshold for the superconductor - insulator transition may be material dependent. It is therefore of some interest to broaden the range of materials that have been studied in this context. Ta, when prepared in a Ta/Ge structure, provides a good system for studying the superconductor-insulator transition because we have shown that the Ta forms electrically continuous layers even at thicknesses of only a few atomic layers.

The discovery of high temperature ceramic superconductors, in which electrons are effectively confined to copper oxide planes, has aroused substantial interest in the effect on the superconducting transition temperature of interlayer coupling between effectively two-dimensional layers. Ta/Ge multilayers present an ideal opportunity to study a model, layered, two-dimensional system in which the important parameters can be continuously varied in the fabrication process. Preliminary measurements suggest that increasing the coupling between Ta layers by decreasing the Ge layer thickness increases the transition temperature above that seen for an isolated Ta layer of the same total thickness. There is also evidence that the transition from isolated to coupled layers as the thickness of the intermediate Ge layers is decreased can be followed in the form of the fluctuation conductivity.

In this chapter we briefly discuss some exploratory measurements of the transition from superconductor to insulator as a function of disorder and the fluctuation conductivity above T_c.

6.1 Influence of Structural Disorder on T_c

Disorder induced localisation of electrons and diffusion enhanced Coulomb repulsion jointly act to cause a decrease in the transition temperature. T_c is predicted to decreased roughly in proportion to the resistance per square both for weak[1] ($k_F l \gg 1$) and strong[2] ($k_F l \sim 1$) disorder. That disorder (as characterised by the resistance per square) should reduce T_c explains a number of observations for the multilayer samples: the reduction in the superconducting transition from the bulk crystalline value, the decrease in T_c as the samples age and the variation of T_c with the resistance per square. Each of these points is discussed briefly below.

In the bulk crystalline state Ta has a superconducting transition temperature of 4.39K but when prepared in an amorphous or disordered state the superconducting transition temperature is much lower, in line with the predictions of Maekawa and Fukuyama, 1981. Read & Altman, 1965, for example report $T_c \sim 0.5$K for β-Ta films while Aguado Bombin & Neal, 1976, measure transition temperatures between 1.5 and 4.5K for bcc and fcc films. The full superconducting transition was not seen for multilayers in this study (we discuss here only those samples with thick Ge layers) but the upper bound of 1.3K for T_c in this study is not inconsistent with the value given by Read & Altman giving further evidence[3] that the films are either amorphous or β-Ta rather than bcc or fcc.

In Section 4.6 resistance measurements made six months apart on the same samples showed that a decrease in the superconducting transition temperature accompanies the increase in the resistivity as impurities diffuse into the Ta layers. The depression of T_c seen as the samples age, is consistent with the predictions of Maekawa and Fukuyama if it is assumed that ageing causes the impurity concentration in the Ta layers to increase. Because the full transition was not seen, it is difficult to assess the variation of T_c with the resistance per square of the multilayers. The value of the resistance at 1.4K normalised to

---

[1] Maekawa and Fukuyama, 1981.

[2] Anderson et al., 1983.

[3] It was noted in Chapter 5 that the room temperature resistivity and TCR of the films more closely resembles that of amorphous Ta or β-Ta than bcc or fcc Ta.

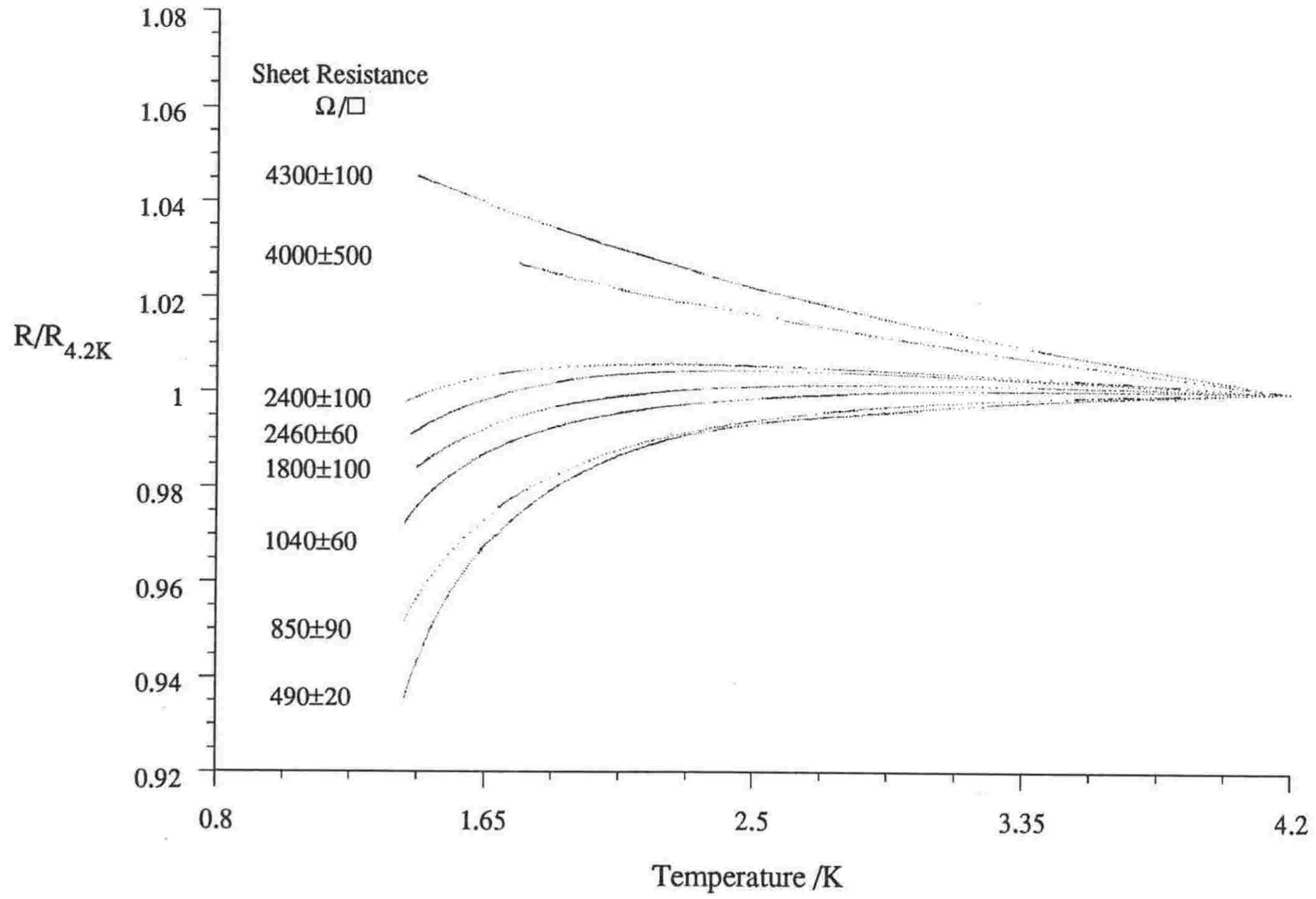

Figure 6.1 Onset of superconductivity for multilayers with thick Ge layers. The superconducting transition temperature increases as a function of the sheet resistance. For samples with a sheet resistance of more than 4000Ω/□ there is no evidence of a superconducting transition.

that at 4.2K (that is $R_{1.4K}/R_{4.2K}$) is smaller for lower values of the resistance per square (see Figure 6.1) suggesting that T_c may indeed decrease in proportion to the resistance per square as predicted by Maekawa and Fukuyama but measurements to lower temperatures are clearly needed before more quantitative conclusions can be drawn.

6.2 Superconductor - Insulator Transition

Referring again to Figure 6.1 there is a clear correlation between the sheet resistance and the behaviour of the resistance when extrapolated to zero kelvin - it would appear that samples with a low sheet resistance will be superconducting while samples with a high sheet resistance will be insulating. The critical sheet resistance separating these two regimes is of the order of 2500Ω/□.

Pang, 1989, describes a simple physical picture of localised electrons that are able to form Cooper pairs only if they have an energy greater than some critical value. The resistance per square at $T = 0$ then depends on the position of the Fermi level relative to this critical energy which in turn depends on the degree of disorder. In this picture the resistance at absolute zero can have only three possible values: infinity (corresponding to fully localised states), R_c (where R_c is given exactly by the quantum resistance per square for Cooper pairs R_Q) or zero (corresponding to superconductivity).

Haviland et al., 1989, have measured the low temperature resistance of homogeneous thin films of Bi and Pb. They find that for Bi films the $T = 0$ superconductor to insulator transition occurs at a sheet resistance very close to R_Q while for Pb the transition occurs for $R_c \approx 9.5\mathrm{k}\Omega/\square$. This raises the possibility that R_c is material dependent.

Fisher et al., 1990, describe a model that predicts similar behaviour to Pangs model but finds the critical resistance R_c separating insulating from superconducting behaviour is $R_c = c_d R_Q$ where c_d is a dimensionless constant, not necessarily equal to one. Sørensen et al., 1992, use Monte Carlo simulations to calculate the critical resistance R_c and find it depends on the details of the electron-electron interaction. For short range repulsion $c_d = 7\pm2$ while for long range Coulomb interaction $c_d = 1.8\pm0.3$.

From the measurements shown in Figure 6.1 for the Ta/Ge multilayers, we draw the tentative conclusion that $R_c \approx 2500\Omega/\square$ (or $c_d \approx 0.4$) although measurements to much lower temperatures are required. Note that measurements to lower temperatures are likely to increase, rather than decrease, the value of R_c deduced from experimental results since the precursor of superconductivity may not necessarily be evident at 1.3K.

6.3 Superconducting Fluctuations Above T_c

The superconducting transition of multilayers with rather thick insulating Ge layers separating the Ta layers occurs (if at all) below the lowest temperature accessible in this study. However, by reducing the thickness of the Ge spacing layers, the transition temperature is increased, bringing it into the temperature range of these experiments. The transitions for a series of samples all with Ta layers (28±5)Å thick but with various Ge layer thicknesses, are shown in Figure 6.2. Not only does the transition shift to higher temperatures for thinner Ge layers but the width of the transition also decreases sharply.

Lawrence and Doniach, 1971, have described the behaviour of layered compounds using a model in which adjacent layers are coupled by Josephson tunnelling. They make predictions for the fluctuation conductivity above T_c as a function of the separation of the superconducting layers. Before discussing these predictions we briefly review fluctuation conductivity for uniform compounds.

Fluctuation conductivity describes the experimentally observed rounding of the superconducting transition. It arises because, although, the formation of Cooper pairs at temperatures above the transition temperature is energetically unfavourable, some fraction of the electrons are nevertheless able to form pairs as a result of fluctuations. Once formed, the Cooper pairs will not be affected by scattering processes until the pairing is broken. The enhancement of the conductivity from the acceleration of fluctuation induced Cooper pairs is termed the direct or Aslamasov-Larkin contribution (Aslamasov & Larkin, 1968(a)&(b)). It is proportional to the density and lifetime of superconducting fluctuations modes and is given by (Thompson, 1970) as

$$\delta\sigma_2^{(\text{A-L})} = \frac{1}{16}\cdot\frac{e^2}{\hbar}\cdot t_r^{-1} \qquad (6.1a)$$

in two dimensions, and

$$\delta\sigma_3^{(\text{A-L})} = \frac{1}{32}\cdot\frac{e^2}{\hbar\xi}\cdot t_r^{-1/2} \qquad (6.1b)$$

in three dimensions, where t_r is the reduced temperature

$$t_r = \frac{T - T_c}{T_c} \qquad (6.2)$$

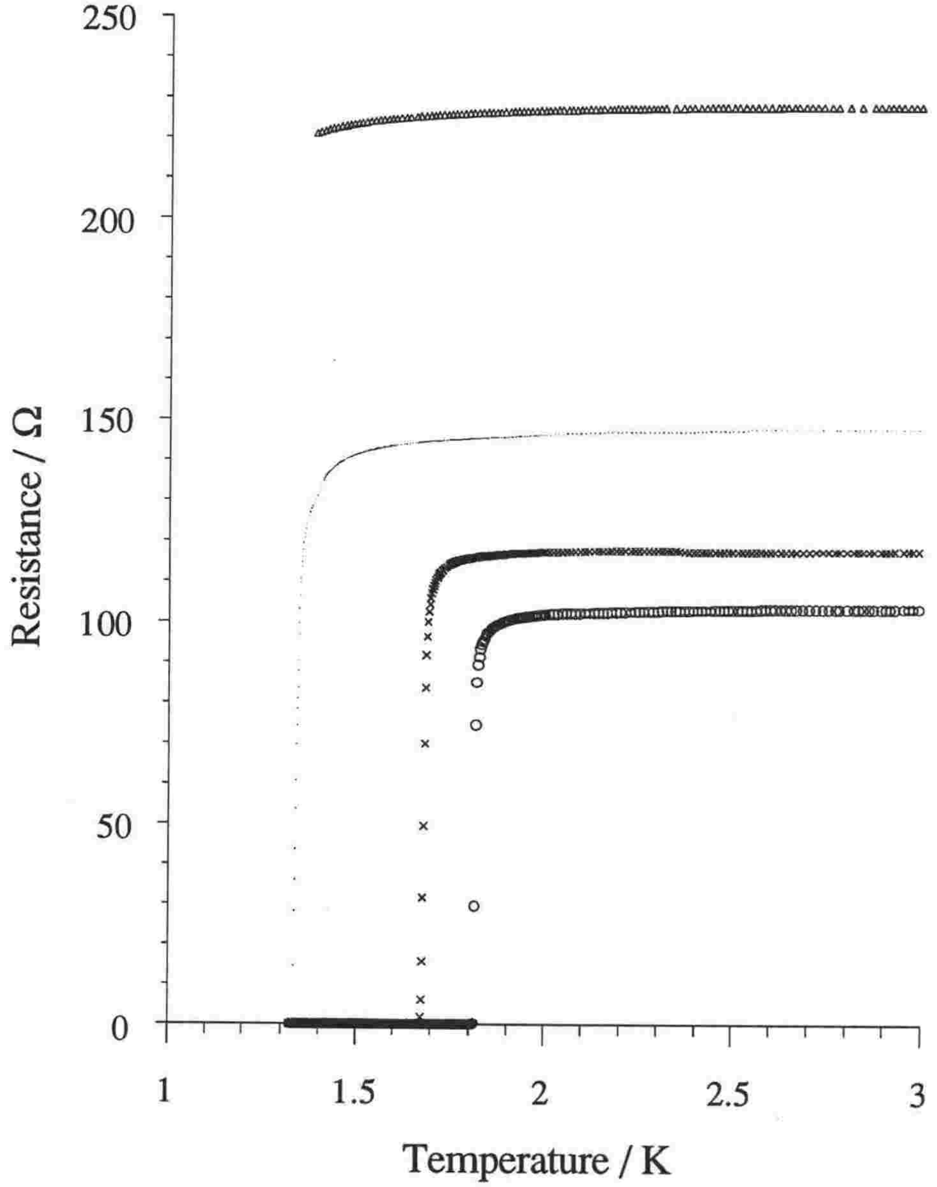

Figure 6.2 Superconducting transition of multilayers with Ta layers of thickness (28±5)Å and Ge layers of thickness: triangles (50±1)Å, dots (31.2±0.9)Å, crosses (20.8±0.6)Å and circles (13.9±0.4)Å. As the Ge layer thickness decreases the superconducting transition temperature becomes sharper and moves to higher temperatures.

VICTORIA UNIVERSITY OF WELLINGTON

and ξ is the temperature independent coherence length. The length scale that determines the cross-over from two dimensions to three dimensions is the coherence length $\xi(T) = \xi t_r^{-1/2}$.

In addition to the direct Aslamasov-Larkin correction, there is an indirect contribution to the conductivity termed the Maki-Thompson correction (Maki 1968(a)&(b) and Thompson, 1970).[4] The Maki-Thompson correction can be understood as the contribution to the conductivity from pairs of electrons of opposite momentum formed by the decay of a superconducting fluctuation. These pairs of electrons of opposite momentum continue to be accelerated in much the same way as Cooper pairs until one of the electrons is scattered into a new energy state in an inelastic collision (see Bergmann, 1984). In three dimensions the Maki-Thompson correction merely changes the Aslamasov-Larkin correction by a constant factor. In two dimensions, the magnitude of the Maki-Thompson correction depends on the inelastic scattering rate but is likely to be much smaller than the Aslamasov-Larkin correction provided $t_r < 0.01$.

We now return to the Lawrence-Doniach model for layered superconductors. If the period s is large compared to the coherence length perpendicular to the layers then the fluctuation conductivity reduces to that of a single film. For small s the fluctuation conductivity has the three dimensional form (Equation 6.1b above) but modified by a factor that depends on the layer spacing and a tunnelling limit. Note that as T_c is approached the coherence length increases so that all samples will enter this second regime provided the temperature is close enough to T_c.

For disordered Ta the temperature dependent coherence length is estimated to be of the order of $(200/\sqrt{T - T_c})$Å so that in the temperature region of interest for fluctuation conductivity ($t_r \ll 1$) the Ta layer thicknesses are much smaller than the coherence length, that is $a_{\mathrm{Ta}} \ll \xi(T)$. Thus for isolated Ta layers (that is thick Ge layers, large s) samples should be two dimensional. As the Ge layers are made thinner (s smaller) there should be a transition to three dimensional behaviour, seen only close to T_c at first, but then evident over a larger temperature range as s is further reduced.

In Figure 6.3, $(1/R - 1/R_{4.2K})^{-1}$ is plotted as a function of temperature for three of the samples in Figure 6.2 ($R_{4.2K}$ is the resistance at 4.2K). If the behaviour near the transition is two dimensional then such a plot will be linear, while three dimensional behaviour gives a square root dependence. The sample with the thickest Ge layers (T_c = 1.33K) shows a linear dependence from 1.4 - 1.8K (that is $0.05 < t_r < 0.35$) with a slope similar to that predicted by Equation 6.1a. Below 1.4K the results are ambiguous but probably due to sample inhomogeneity. The sample with the thinnest Ge layers (T_c =

---

[4] This is the correction discussed in Section 5.1.5.2 except that here, temperatures near T_c, rather than greatly in excess of T_c, are considered.

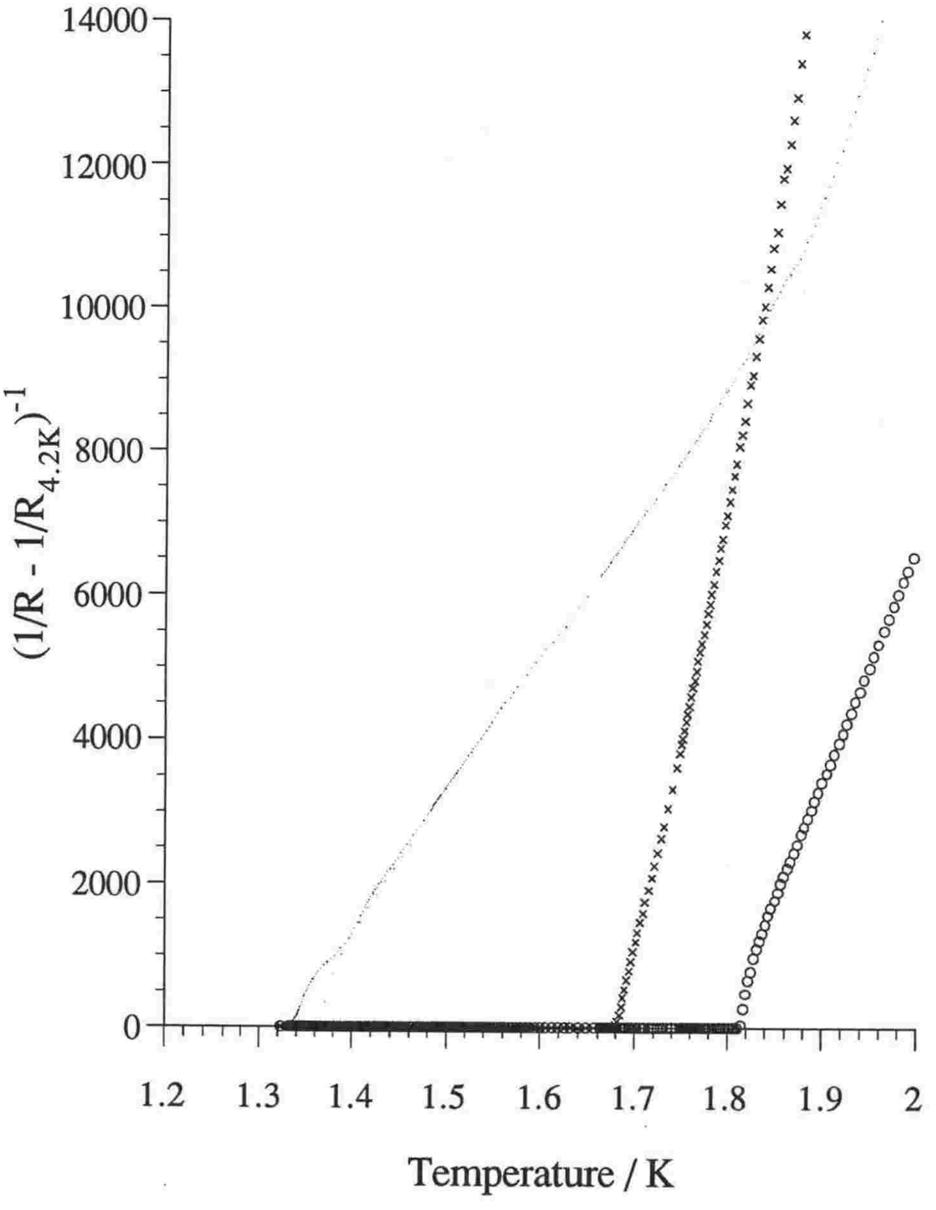

Figure 6.3 Superconducting transition for multilayers with Ta layers of thickness (28±5)Å and thin Ge layers of thickness: dots (31.2±0.9)Å, crosses (20.8±0.6)Å and circles (13.9±0.4)Å. The sample with the thickest Ge layers shows behaviour characteristic of decoupled layers (except very near the transition) while the sample with the thinnest Ge layers shows behaviour characteristic of coupled layers near the superconducting transition changing to decoupled layer behaviour further from the transition.

1.81K) shows two dimensional, linear variation below ~2K changing to square root behaviour near T_c. The slope in the linear region is greater than predicted by Equation 6.1a by a factor of ~7. It is concluded that the behaviour of the samples with the thinnest and thickest Ge layers shows good qualitative agreement with the predictions of Lawrence and Doniach. The superconducting transition of the sample with Ge layers of intermediate thickness is quite different to either two or three dimensional predictions and cannot be explained within this model.

A number of Ta/Ge alloys are known to be superconducting with transition temperatures in the range 1.8 - 2.5K[5] and a natural question is whether alloying rather than layer coupling effects are responsible for the results discussed in this section. While the possibility of alloying cannot be definitively ruled out it is very difficult to explain the observed dependence of the transition temperature on the Ge layer thickness in terms of alloy formation. Note also that the conductivity of amorphous Ge is too low to explain the enhancement of T_c in terms of conventional proximity effect models.

6.4 Conclusions

Superconductivity in Ta/Ge multilayers has been shown to display some interesting features worthy of further investigation. The ability to prepare homogeneous thin layers of Ta recommend the multilayer system to an investigation of the disorder induced superconductor - insulator transition. An initial estimate for the lower bound of the $T=0$ sheet resistance at the critical point is tentatively set at 2500Ω/□. By varying the Ge layer thickness this system can also be used to investigate coupling between quasi two dimensional layers. Measurements in this study suggest that the transition from coupled to decoupled layers can be followed in the form of the fluctuation conductivity. We also see the interesting result that coupling between layers appears to increase T_c above that seen for the thickest isolated Ta layers.

---

[5] Ghosh & Douglass, 1977, have investigated a range of sputter deposited Ta_xGe_{1-x} alloys and find transition temperatures lying in the range 1.8 to 2.5K while Knoedler & Douglass, 1979, measured a transition temperature of 1.8 to 2.4K (depending on deposition conditions) for sputtered $TaGe_2$. We have confirmed these results by making a number of thin film Ta/Ge alloys approximately 1000Å thick, prepared by simultaneously evaporating tantalum and germanium onto stationary substrates in a similar manner to that employed in the fabrication of the multilayers. The resistance of three alloys was measured and in each case a sharp superconducting transition was seen in the temperature range 1.5 to 2.5K.

Chapter Seven

Discussion and Conclusion

This thesis presents the results of an experimental study of electron conduction processes in disordered Ta/Ge multilayers. The measurement of the in-plane resistance alone has revealed behaviour rich with interesting features. In this chapter the most important results are summarised, and discussed in the light of recent results by other workers.

We have described a method of fabrication which produces well defined layers even when the constituent layers are only a few atoms thick, allowing us to probe essentially two dimensional layers as well as thicker bulk-like layers. From our measurements it is concluded that the Ta layers are either amorphous Ta or β-Ta. That we cannot distinguish between the two possibilities does not impinge on the interpretation of the resistivity, the only important conclusion in this context being that the Ta layers are disordered. The interpretation of the resistance relies in most cases on the assumption that the multilayers can be treated as n isolated layers in parallel. We do not see any effects which cannot be explained on the basis of this model, except possibly in the cases of the very thinnest Ta layers (<10Å). The discussion of the resistance of the multilayers is conveniently divided into three regions: high and low temperature results and the superconducting transition. We will discuss each of these regions in turn below.

At high temperatures (100-300K) the resistance of disordered Ta increases as the temperature is lowered as expected for a high resistivity non-simple disordered metal from consideration of the Mooij correlation. The high temperature results have been interpreted in terms of weak localisation theory and information about the governing parameter (the phase breaking rate τ_ϕ^{-1}) has been extracted from the data. Measurement of the resistance as a function of temperature alone is not sufficient to deduce the magnitude of the phase breaking rate but some conclusions about the temperature dependence of τ_ϕ^{-1} may be made. We find τ_ϕ^{-1} varies at a rate in between a linear and a quadratic dependence on temperature. A linear dependence is expected for electron-phonon scattering in the "clean" limit ($q_{ph}^{-1} < l$) while a quadratic dependence is expected in the "dirty" limit ($q_{ph}^{-1} > l$). For the samples in this study the mean free path is limited by the interatomic spacing while the inverse phonon wave vector is estimated to be of the order of a few angstroms, hence $q_{ph} \sim l$ and the samples are neither in the "clean" nor "dirty" limits. It is therefore not unreasonable that the temperature dependence of the phase breaking rate lies between that expected for electron-phonon scattering in the "clean" and "dirty" limits. Only a handful of studies of the high temperature resistivity of metallic glasses have been quantitatively interpreted in terms of weak localisation theory. Howson, 1984, studied titanium alloys ($Cu_{50}Ti_{50}$ and $Ti_{50}Be_{40}Zr_{10}$) with room temperatures resistivities of the order of 200μΩ·cm and found the conductivity was proportional to the square root of the temperature, that is $\tau_\phi^{-1} \propto T$, consistent with "clean" electron-phonon scattering. Howson & Greig, 1986, find the same behaviour for copper alloys ($Cu_{50}Zr_{50}$ and $Cu_{50}Hf_{50}$) with a similar room temperature resistivity. Mitzutani et al., 1988, discuss a high resistivity AgCuGe alloy (ρ = 500μΩ·cm) in terms of weak localisation theory and find that a log-log plot of the conductivity as function of temperature has a slope of slighty less than unity. This implies $\tau_\phi^{-1} \propto T^p$ where p is slightly less than 2, most nearly consistent with "dirty" limit electron phonon scattering. A systematic study of the high temperature resistivity of a variety of disordered glasses is clearly called for.

The low temperature behaviour of the resistivity is less easily interpreted. We have shown however, that the form of the resisitivity is a strong function of the Ta layer thickness reflecting the importance of dimensionality on electron conduction on disordered materials. For the thinnest Ta layers the resistivity increases at all temperatures as the temperature is lowered. Below ~5K the conductivity decreases logarithmically, most probably as a result of two-dimensional electron-electron interaction effects. At higher temperatures quantum interference effects dominate. As the Ta layer thickness is increased the logarithmic behaviour below ~5K gradually disappears suggesting that electron-electron interaction effects are becoming weaker as a result of entering a 3D regime. The decreasing strength of electron-electron interactions alone cannot explain the turnover to a negative TCR at about 15-20K seen for thicker Ta layers. Nor can the turnover in the resistance be explained in terms of spin-orbit scattering rates orders of magnitude larger than either predictions. In summary, we have found that interaction effects, weak localisation and superconducting fluctuations are all important at low temperatures in disordered Ta. To interpret the data more quantitatively requires more information. Measurements to lower temperatures would be useful to determine the superconducting transition temperature entering the expressions for superconducting fluctuations and for electron-electron interaction effects. Magnetoresistance measurements would also help to separate the various contributions to resistivity.

An in-depth study of the superconducting properties of Ta/Ge multilayers lies beyond the scope of this thesis. Nevertheless a number of interesting features have been identified, providing a basis for further work in this area. The ability to prepare ultra-thin homogeneous layers of disordered Ta make the Ta/Ge multilayer system ideal for studying the disorder-induced superconductor-insulator transition. Measurements to 1.4K place a lower bound of 2500 Ω/□ on the $T = 0$ sheet resistance at which the superconductor-insulator transition occurs. Measurements to much lower temperatures are needed to define this critical resistance more accurately, thereby allowing comparisons between this work and that of other authors. It may then be possible to address the question of whether the critical resistance is a universal constant or whether it is material dependent.

The superconductivity of the multilayer structure itself also proved of interest. For samples with rather thick Ge layers, the transition lies below the lowest temperatures that were measured in this study. However, reducing the thickness of the intermediate insulating Ge layers systematically raises the transition temperature of the multilayers into the measured temperature region. In addition, we find that the reduction in the Ge layer thickness changes the form of the fluctuation conductivity above the superconducting transition from a two dimensional form to a three dimensional form. We believe these effects can be explained in terms of the onset of Josephson-like coupling between the Ta layers. Our data also raise the intriguing possibility that n coupled Ta layers of thickness a_{Ta} may have a higher superconducting transition temperature than a single film with the same structure but of thickness na_{Ta}, a point worthy of further investigation.

Superconductivity in superconductor/insulator multilayer systems has been studied previously. Ruggiero et al.1980 & 1982 saw evidence of a transition from isolated two-dimensional layers to coupled quasi-three-dimensional films in both the form of the fluctuation conductivity and the upper critical field. Jin et al, 1987, found a systematic dependence of T_c on the Ge layer thickness in NbTi/Ge multilayers and saw 3D-like behaviour of the upper critical field in a multilayer with 19Å thick Ge layers. Steel et al., 1993, studied the superconducting transition in MoGe/Ge multilayers via the perpendicular (rather than the in-plane) resistance as a function of both temperature and magnetic field and found evidence of interlayer vortex decoupling. None of these studies discuss the possibility of enhanced superconducting transition temperatures as a result of interlayer coupling. Luby et al, 1992, however find $T_c = 2.72\text{-}4.21\text{K}$ for W/Si multilayers, whereas the superconducting transition temperature of bulk W is only 0.012K. Similarly Cherradi et al., 1989, found $T_c \sim 1\text{K}$ for Au/Si multilayers while Nakajima et al, 1989, found T_c of ~ 7K in Mo/Si multilayers although T_c for bulk Mo is 0.92K and Au is not superconducting at all. These authors attempt to explain their results in terms of the formation of amorphous metal-silicide phases. The results presented in this thesis differ from these results in that we have observed a strong dependence of T_c on the germanium layer thickness which would appear to contradict any explanation involving alloy formation.

Appendix I

Thermometer Calibration

Cryogenic Calibrations Ltd. define a rhodium-iron reference scale 0.5 - 273K derived from measurements on a reference rhodium-iron thermometer. The reference scale tabulates the temperature T in terms of Z_R,

$$Z_R = \frac{R_T - R_{4.2221}}{R_{273.16} - R_{4.2221}} \tag{I.1}$$

where R_T is the resistance of the reference thermometer. Cryogenic Calibrations Ltd. then define a similar function Z for the Rh-Fe thermometer to be calibrated and list the resistance R, the temperature T and the deviation from the reference function ΔZ (where $\Delta Z = Z_R - Z$) for 38 calibration points. The calibration can be used to find the temperature which corresponds to the measured resistance of the Rh-Fe thermometer by calculating Z from the measured resistance using the function defined in the calibration, estimating ΔZ from a plot of ΔZ versus R drawn from the calibration points, calculating Z_R and then determining the temperature from the reference tables.

By expressing both the reference function and ΔZ as polynomials, the process of converting a measurement of the thermometer resistance to a temperature can be handled by computer. The reference function, that is T_{ref} as a function of Z_R, may be expressed as two polynomials - one of 10th order describing the temperature range above 27K and one of 11th order describing temperatures below 27K:

$$T_{\text{ref}} = \left\{ \begin{array}{ll} \sum_{n=0}^{11} a_n x^n, & T_{\text{ref}} < 27\text{K}, \\ \sum_{n=0}^{10} b_n x^n, & T_{\text{ref}} > 27\text{K} \end{array} \right\} \tag{I.2}$$

n	Below 27K a_n	Above 27K b_n
0	9.0148855	85.368599
1	11.892611	83.147298
2	5.619332	45.086034
3	2.262668	37.121044
4	0.512088	18.012208
5	0.107552	8.79496
6	0.288768	-4.02224
7	-0.208704	0.887168
8	-1.22816	0.977024
9	-0.630528	-4.553984
10	0.477184	2.341888
11	0.340992	-

Table I.1 Coefficients for evaluating the reference function.

where

$$x = \left\{ \begin{array}{ll} 25(Z_R - 0.02), & T_{\text{ref}} < 27\text{K}, \\ \dfrac{2 ln Z_R + 3}{3}, & T_{\text{ref}} > 27\text{K} \end{array} \right\} \tag{I.3}$$

and the calculated coefficients a_n and b_n are as given in Table I.1. The deviation, ΔZ, of the thermometer from the reference function was fitted to sixth order polynomials in each of three temperature ranges. Thus

$$\Delta Z = \left\{ \begin{array}{ll} \sum_{n=0}^{6} c_n R^n, & T_{\text{ref}} < 27\text{K}, \\ \sum_{n=0}^{6} d_n R^n, & 27\text{K} \le T_{\text{ref}} < 100\text{K}, \\ \sum_{n=0}^{6} e_n R^n, & 100\text{K} \le T_{\text{ref}} < 273\text{K}. \end{array} \right\} \tag{I.4}$$

The coefficients c_n, d_n and e_n are given in Table I.2.

n	Below 27K c_n	27 - 100K d_n	Above 100K e_n
0	$9.4159031\text{x}10^{-3}$	$-1.2028475\text{x}10^{-1}$	$-8.8194593\text{x}10^{-3}$
1	$-3.1387560\text{x}10^{-2}$	$1.5313202\text{x}10^{-1}$	$6.1350269\text{x}10^{-3}$
2	$4.5634204\text{x}10^{-2}$	$-8.0825661\text{x}10^{-2}$	$-9.6031471\text{x}10^{-4}$
3	$-3.4165411\text{x}10^{-2}$	$2.3006459\text{x}10^{-2}$	$7.2160102\text{x}10^{-5}$
4	$1.2793991\text{x}10^{-2}$	$-3.6697466\text{x}10^{-3}$	$-2.7467274\text{x}10^{-6}$
5	$-2.0127470\text{x}10^{-3}$	$3.0907397\text{x}10^{-4}$	$4.2200826\text{x}10^{-8}$
6	$5.7746577\text{x}10^{-5}$	$-1.0712047\text{x}10^{-5}$	$-3.6462991\text{x}10^{-11}$

Table I.2. Coefficients for evaluating ΔZ for rhodium-iron resistance thermometer (calibration number 18417) using Equation I.4.

Using this method of computing the temperature from the resistance of the rhodium-iron thermometer used in this study, the Cryogenics Calibrations Ltd. calibration can be reproduced to within 3mK below 27K, within 5mK from 27K to 100K and within 7mK from 100K to 273K.

Appendix II

Current Controller

The circuit diagrams for the current controller discussed in Section 4.4 are shown in Figures II.1 - II.3. The controller is connected between the printer port of the computer and the printer itself. A manual switch allows the controller to be by-passed during printing. When the controller is operative, information sent to the printer port is not printed. Instead it is used to set the direction of the current through the samples and to turn the current on and off. A constant current source supplies a current I_{in} to the controller. The state of the output current I_{out}, relative to I_{in}, is determined by the most recent signal sent to the printer port. Effectively, the controller examines the last two bits of a binary signal and sets internal switches connecting the input current to the output leads accordingly. The last bit determines whether the current is on or off. If the last bit is 1 (that is, HIGH) the current is on, otherwise the current is off (last bit 0 or LOW). The second to last bit determines the direction of the current. If the second to last bit is 1 (that is, HIGH) the current is reversed, otherwise the output current is in the same direction as the input (last bit 0 or LOW). Thus a "0" (binary 00) sent to the printer port sets $I_{out} = 0$, a "1" (binary 01) sets $I_{out} = I_{in}$ and "3" (binary 11) sets $I_{out} = - I_{in}$. LEDs indicate the status of the current. The controller requires an external power supply of +5V DC.

The circuit was designed and built by Bob Halford and Grant Parratt of the Physics Department Electronics Workshop.

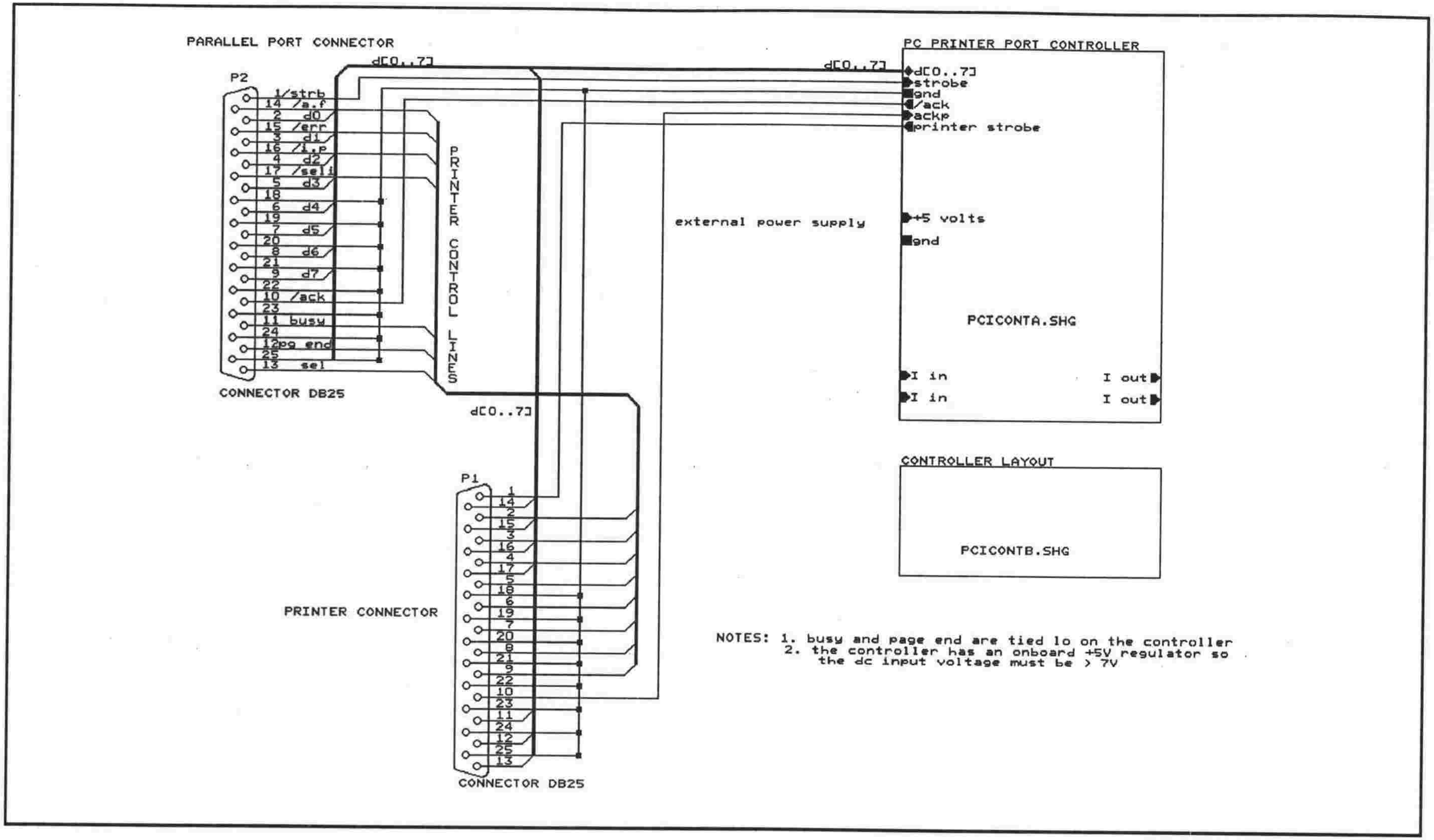
PARALLEL PORT CONNECTOR
P2
1 /strb
14 /a.f
2 d0
15 /err
3 d1
16 /i.p
4 d2
17 /sel i
5 d3
18
6 d4
19
7 d5
20
8 d6
21
9 d7
22
10 /ack
23
11 busy
24
12 pg end
25
13 sel
CONNECTOR DB25
d[0..7]
PRINTER CONTROL LINES
d[0..7]
P1
1 14 2 15 3 16 4 17 5 18 6 19 7 20 8 21 9 22 10 23 11 24 12 25 13
CONNECTOR DB25
PRINTER CONNECTOR
external power supply
d[0..7]
PC PRINTER PORT CONTROLLER
d[0..7]
strobe
gnd
/ack
ackp
printer strobe
+5 volts
gnd
PCICONTA.SHG
I in
I in
I out
I out
CONTROLLER LAYOUT
PCICONTB.SHG

NOTES: 1. busy and page end are tied lo on the controller
2. the controller has an onboard +5V regulator so
the dc input voltage must be > 7V

Figure II.1 Current contoller interconnection.

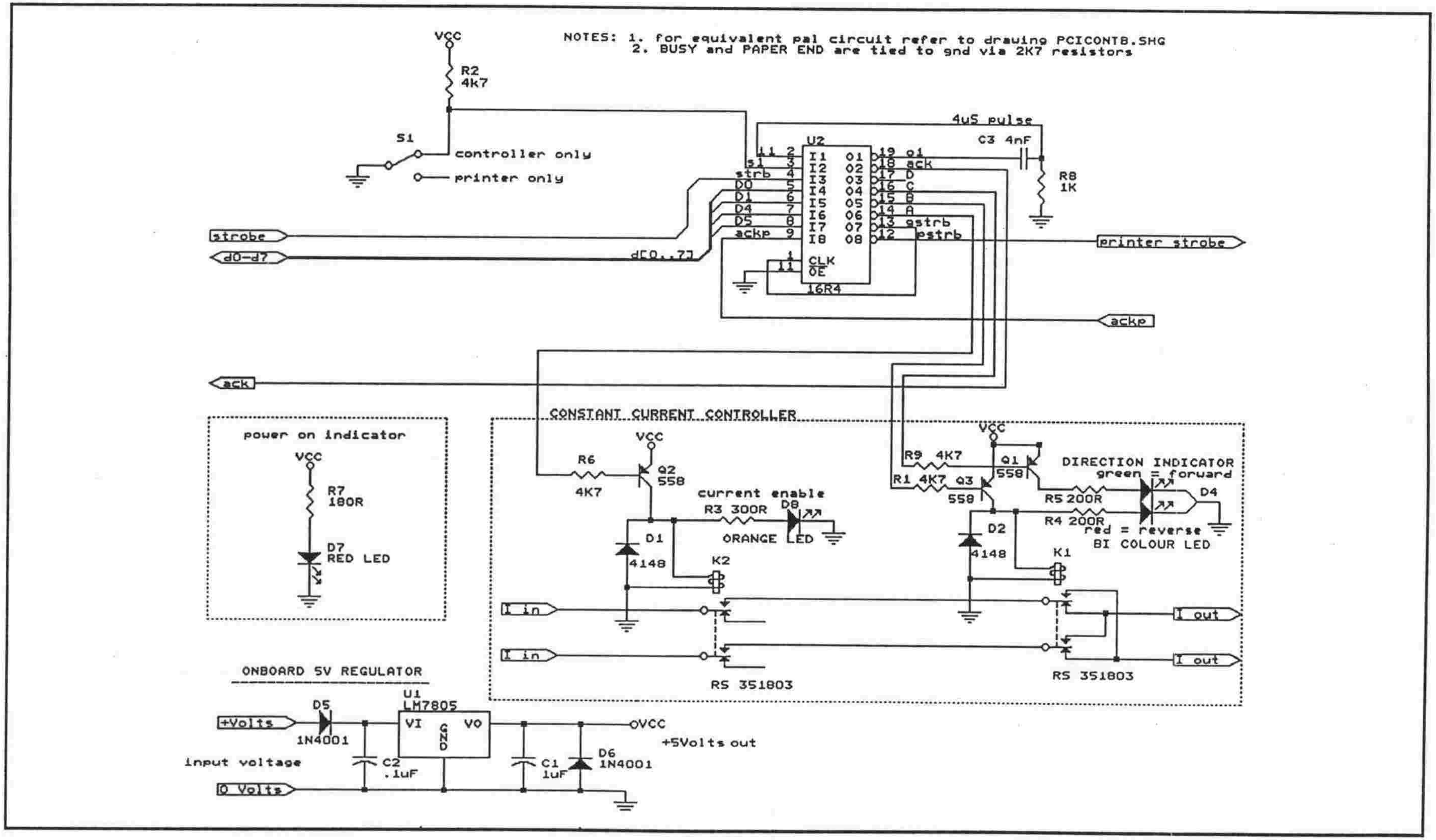
NOTES: 1. for equivalent pal circuit refer to drawing PCICONTB.SHG
2. BUSY and PAPER END are tied to gnd via 2K7 resistors
VCC
R2
4k7
S1
controller only
printer only
U2
I1 I2 I3 I4 I5 I6 I7 I8
O1 O2 O3 O4 O5 O6 O7 O8
CLK
OE
16R4
s1 strb D0 D1 D4 D5 ackp
q1 ack D C B A gstrb pstrb
4uS pulse
C3 4nF
R8
1K
strobe
d0-d7
d[0..7]
printer strobe
ackp
ack
CONSTANT CURRENT CONTROLLER
R6
4K7
Q2
558
current enable
R3 300R
D8
ORANGE LED
D1
4148
K2
I in
I in
RS 351803
R9 4K7
R1 4K7
Q1
558
Q3
558
DIRECTION INDICATOR
green = forward
R5 200R
R4 200R
red = reverse
BI COLOUR LED
D4
D2
4148
K1
I out
I out
RS 351803
power on indicator
R7
180R
D7
RED LED
ONBOARD 5V REGULATOR
U1
LM7805
VI
GND
VO
D5
1N4001
+Volts
input voltage
0 Volts
C2
.1uF
C1
1uF
D6
1N4001
+5Volts out

Figure II.2 Current controller.

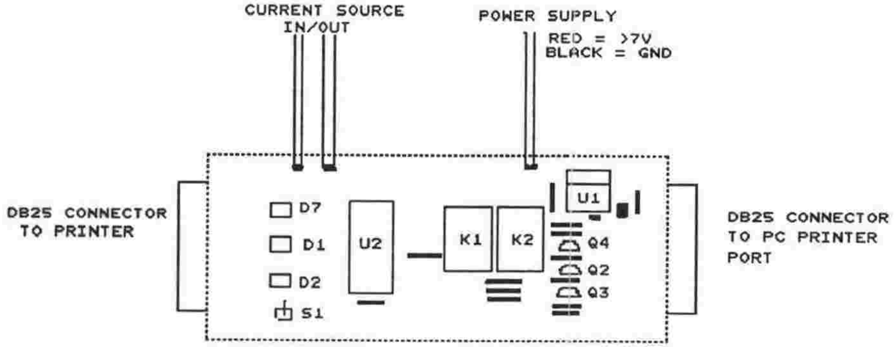
CURRENT SOURCE
IN/OUT
POWER SUPPLY
RED = >7V
BLACK = GND
DB25 CONNECTOR
TO PRINTER
D7
D1
D2
S1
U2
K1
K2
U1
Q4
Q2
Q3
DB25 CONNECTOR
TO PC PRINTER
PORT

NOTE : 1. controller built on matrix board

Figure II.3 Current controller layout.

Appendix III

Probability of Self-Intersection in a Random Walk

There is a finite probability that during a time t, a diffusing particle will revisit some position in space (that is, a finite probability of self-intersection in a random walk). If the particle can be described as a wave with wavelength λ and velocity υ then the volume swept out in time $\mathrm{d}t'$ is of the order of $\upsilon \cdot \lambda^2 \cdot \mathrm{d}t'$. If $R(t)$ is the displacement from the origin as a function of time then the root mean square displacement R_{rms} is

$$\begin{aligned} R_{rms} &= \int_0^t R(t)^2 \mathrm{d}t \\ &= (6Dt)^{1/2} \end{aligned} \tag{III.1}$$

and the particle moves within a sphere of volume of the order of $R^3_{rms} \sim (Dt)^{3/2}$. The probability that the diffusing particle will revisit some point in space during a time t is therefore

$$P_{\text{self-intersection}} \sim \int_0^t \frac{\upsilon \cdot \lambda^2 \cdot \mathrm{d}t'}{(Dt')^{3/2}}. \tag{III.2}$$

Appendix IV

Variation in Potential at a Ta/Ge Interface

The variation in potential across a contact between a metal and an extrinsic semiconductor is the familiar problem from electronics of a Schottky barrier[1]. The usual solution is to calculate the potential $V(x)$, where x is measured perpendicular to the interface, from the known charge distribution $\rho(x)$ via Poisson's equation;

$$-\nabla^2 V = -\frac{\mathrm{d}^2 V}{\mathrm{d}x^2} = \frac{4\pi\rho(x)}{\in} \quad . \tag{IV.1}$$

This is the method we shall adopt here, although the solution turns out to be different to that for a Schottky barrier owing to the difference between the density of states in amorphous Ge and that in extrinsic semiconductors. For simplicity we shall consider an abrupt infinite planar Ta/Ge interface. We shall assume that the Ta and Ge layers are infinitely thick and that bulk behaviour prevails far from the interface. Before any progress can be made a qualitative picture of the density of states in amorphous Ge must be chosen. We use that given by Mott & Davis[2] (see Figure IV.1a) with the additional simplification that gap states due to dangling bonds can be represented by two delta functions, one above and one below the Fermi energy. A representation of the electronic structure of isolated Ge with delta function dangling bond states is shown in Figure IV.1b together with a simple representation for Ta.

When the amorphous Ge layer is brought into contact with the Ta layer there will be a redistribution of charge until the Fermi energies on either side of the interface are level. The band bending effects this gives rise to are illustrated in Figure IV.1c. Four regions can be identified. In region 1, that is $x > x_2$, the behaviour is characteristic of isolated amorphous Ge. There is no excess charge and the potential is constant. As the interface is approached band bending causes dangling bond states to lie below the Fermi level. Thus in region 2, that is $x_1 < x < x_2$, the charge density is constant and given by the

---

[1] See for example, Jaros, 1989.

[2] Mott & Davis, 1971.

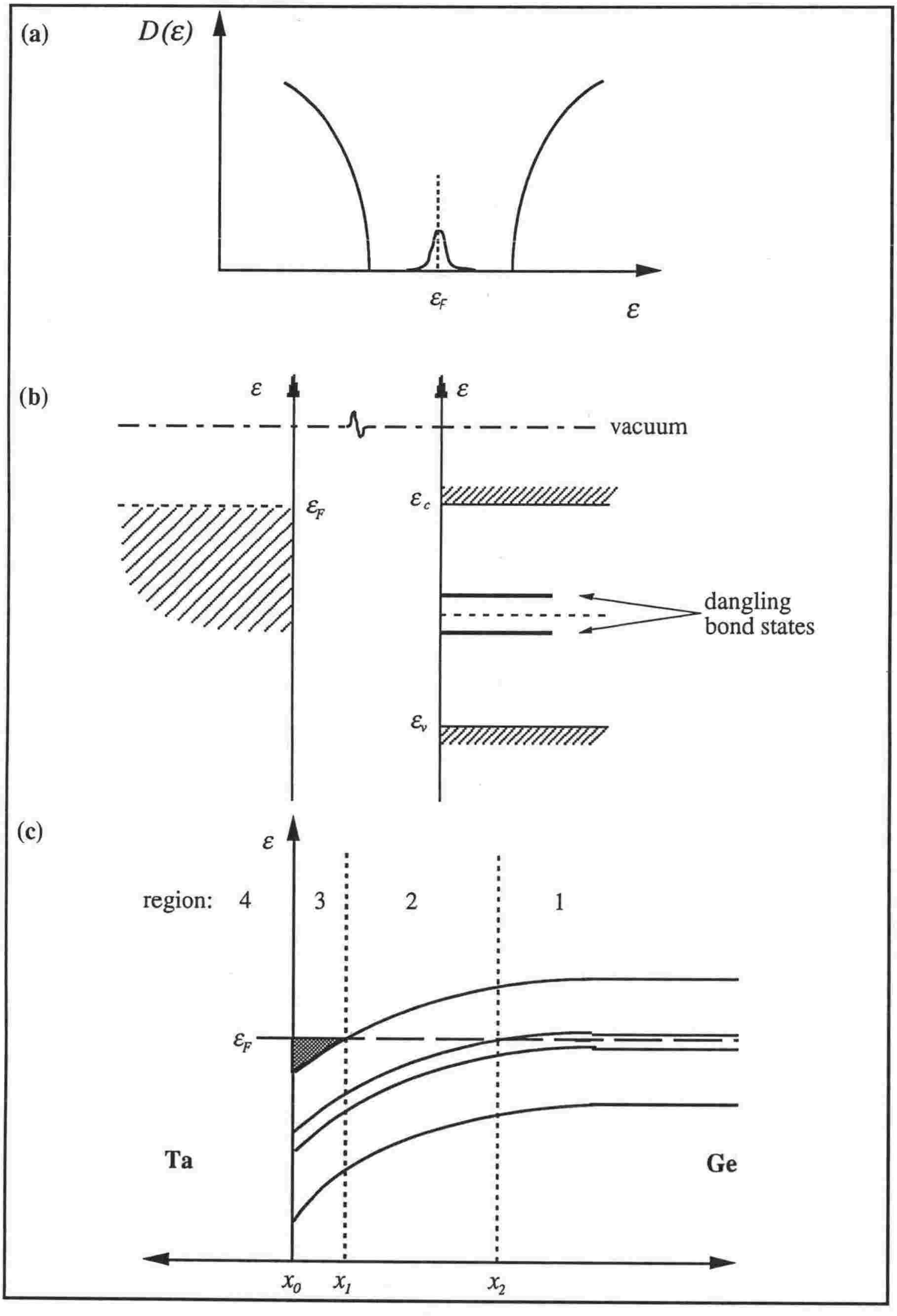
(a)
$D(\varepsilon)$
ε_F
ε
(b)
ε
ε
vacuum
ε_F
ε_c
dangling bond states
ε_v
(c)
ε
region: 4 3 2 1
ε_F
Ta
Ge
x_0
x_1
x_2

Figure IV.1 (a) Density of states of amorphous Ge given by Mott & Davis, 1971. (b) Band diagram for isolated Ta and Ge - energies are given relative to the vacuum. (c) Equilibrium band diagram for Ta/Ge interface.

density of dangling bonds, ρ_d, multiplied by the charge of an electron, $-e$. At x_1 the conduction band edge ε_c dips below the Fermi level ε_F and electrons from the Ta layer spill across the interface, filling the conduction band to an energy $\delta\varepsilon(x)$ above the conduction band edge ε_c. This extra charge density is given by

$$\rho_c(x) = -e\int_{\varepsilon_c}^{\varepsilon_c+\delta\varepsilon(x)} g_c(\varepsilon)\, d\varepsilon \qquad \text{(IV.2)}$$

where $g_c(\varepsilon)$ is the conduction band density of states. Provided $\delta\varepsilon(x)$ is small the density of states may be approximated by

$$g_c(\varepsilon) = \frac{m_c^{3/2}}{\hbar^3\pi^2}\sqrt{2|\varepsilon-\varepsilon_c|} \qquad \text{(IV.3)}$$

where $m_c{}^3$ is the determinant of the conduction band effective mass tensor. We may relate $\delta\varepsilon(x)$ to the potential $V(x)$ relative to the potential at $x = \infty$ and the band gap E_g as

$$\delta\varepsilon(x) = \varepsilon - \varepsilon_c = \varepsilon - \varepsilon_F + \varepsilon_F - \varepsilon_c = -V(x). \qquad \text{(IV.4)}$$

By substituting Equation (IV.3) into (IV.2), performing the integration and then simplifying using (IV.4) we find

$$\rho_c(x) = \frac{-em_c^{3/2}}{3\hbar^3\pi^2}\left(2|eV(x) + 2E_g|\right)^{3/2} .$$

Any potential gradients in the Ta layer (region 4, $x < x_o$) will be negligible due to the high electron density ($\sim 3\times10^{24}$ cm^{-3}). Thus Poisson's equation for the case under consideration is given by

$$V''(x) = \left\{\begin{array}{ll} 0, & x > x_2, \\ \dfrac{4\pi e}{\epsilon}\rho_d, & x_1 < x < x_2, \\ \dfrac{4\pi e}{\epsilon}\left(\rho_d + \dfrac{m_c^{3/2}}{3\hbar^3\pi^2}\left(2|eV(x) + 2E_g|\right)^{3/2}\right), & 0 < x < x_1, \\ 0, & x < 0. \end{array}\right\} \qquad \text{(IV.5)}$$

For $x > x_2$ and $x < 0$, i.e. regions 1 & 4, $V(x)$ is constant. Since we have chosen to measure potential relative to the potential in region 1 we take $V_1(x) = 0$ and $V_4(x) = V_c$ where V_c is the contact potential between Ta and Ge (see Figure IV.1b). In region 2, integration yields a quadratic form for the potential $V_2(x)$. Requiring $V_2(x)$ and its derivative to be continuous at x_2 gives $V_2(x)$ explicitly as

$$V_2(x) = \frac{4\pi e \rho_d}{\in} \left(x - x_2\right)^2 \ .$$

The distance $(x_2 - x_1)$ can be found by noting that $V_2(x) = E_g/2e$ at x_1. Hence

$$(x_2 - x_1)^2 = \frac{\in E_g}{8\pi e^2 \rho_d} \ . \qquad \text{(IV.7)}$$

To find the potential in region 3, that is $x_0 < x < x_1$, requires the solution of a non-linear differential equation (refer to Equation IV.5). This has been done numerically using a fourth-order Runge-Kutta method.[3] The values used to calculate the potential shown in Figure IV.2 are given in the figure caption. The distance x_1 (~ 3.1Å) is relatively insensitive to ρ_d but it does depend on the choice of E_g. For example, choosing E_g = 0.4eV increases x_1 to ~4.5Å. The choice of the contact potential V_c is also important. For $V_c < \frac{1}{2}E_g$, region 3 does not exist (or equivalently $x_1 = 0$) while $V_c = 2V$ implies that x_1 lies between 3 and 6Å depending on the choice of E_g. The true value for V_c is very difficult to estimate since it will depend critically on the nature of the interfaces which are not well characterised.

It should be stressed that this is not a rigorous calculation. Firstly, the calculated potential varies very rapidly on an interatomic scale. Consequently the use of a macroscopic Poisson's equation is of questionable validity. Secondly, the model used for the density of states of amorphous Ge is a convenient simplification only. Particularly troublesome is the assumption that $g_c(\varepsilon) \propto \sqrt{|\varepsilon - \varepsilon_c|}$ for values of ε-ε_c up to several tenths of an eV when the expected range of validity is of the order of a few meV. Furthermore, the localised nature of the dangling bond states has been ignored.

Up to now it has been assumed that V_c is positive and electrons from the Ta layer penetrate a distance x_1 into the Ge layer. It is conceivable that V_c is negative. In this

---

[3] See for example Bronson, 1973.

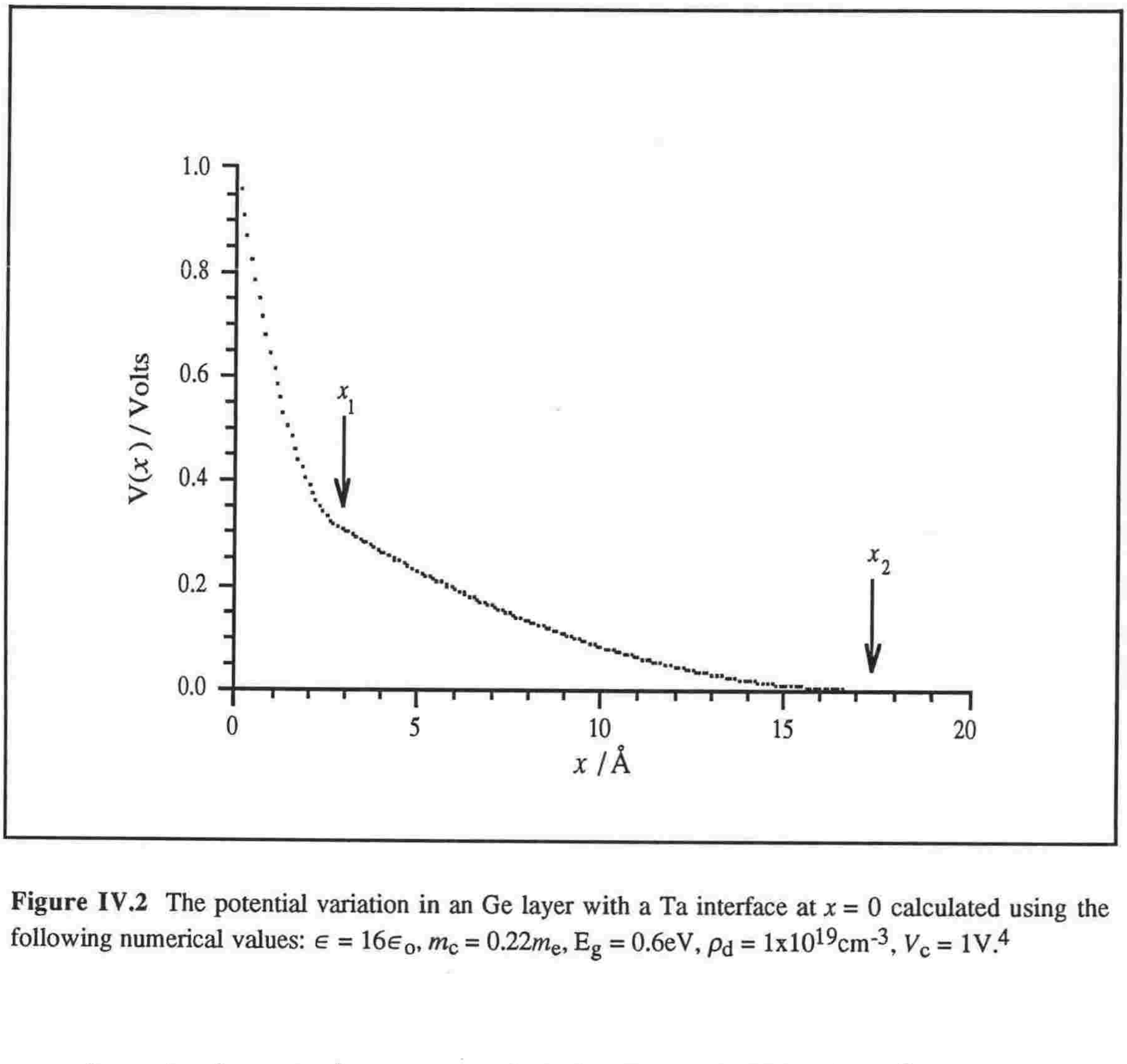

Figure IV.2 The potential variation in an Ge layer with a Ta interface at $x = 0$ calculated using the following numerical values: $\epsilon = 16\epsilon_0$, $m_c = 0.22m_e$, $E_g = 0.6$eV, $\rho_d = 1\text{x}10^{19}\text{cm}^{-3}$, $V_c = 1$V.[4]

case, the region $0 < x < x_1'$ represents a depletion layer of width $x_1' \gg x_1$.[5]

We now turn to the question of how the potential variation near the interfaces affects conduction in the multilayers. Provided the Ge layers are sufficiently thick (i.e. $a_{Ge} > 2x_2$) the multilayers can be considered as a series of discrete layers. If $V_c < \frac{1}{2}E_g$ then the variation in potential will be due exclusively to dangling bond states lying above the Fermi level. Since these are localised states, they are not expected to contribute significantly to the conductivity of the multilayers. If $V_c > \frac{1}{2}E_g$ then there is a space charge region near the interface which may be highly conducting. Using the values given in Figure IV.2 the charge density in this region is no greater than 10^{21}cm^{-3}: three orders of magnitude less than that in the Ta layer. Hence the effect on the conductivity is expected to be small.

---

[4] We take the crystalline values for ϵ and m_c. The energy gap E_g is that given by Mott & Davis, 1971 for a room temperature deposited film. The dangling bond density is taken from Buckley, 1979.

[5] The carriers available for transfer to the Ta layer will be those carriers in the conduction band of Ge. The conduction band will be filled according to Fermi - Dirac statistics to a level of the order of 1meV at 300K. This is much less than the level to which electrons from the Ta layer spill over into the conduction band of Ge (~0.7eV) for a positive value of the contact potential. Thus $\rho_c(x)$ will be several orders of magnitude smaller in the case of a negative contact potential, and hence $V(x)$ will be a more slowly varying function of x. As a result the width of the depletion layer x_1' will be greater than the width of the charged layer x_1 seen in the case previously examined.

It is concluded that the effect on the conductivity of preparing disordered Ta as a multilayer rather than an isolated layer is probably negligible although they may need to be taken into consideration when the Ta and Ge layers are extremely thin.

References

Abrahams, E., P. W. Anderson, D. C. Licciardello and T. V. Ramakrishnan, 1979, *Phys. Rev. Lett.*, 42, 673.

Abrikosov, A. A. and L. P. Gorkov, 1962, *Zh. Eksp. Teor. Fiz.*, 42, 1088, (*Sov. Phys. - JETP*, 15, 752.

Aguado Bombin, R. M. and W. E. J. Neal, 1976, *Appl. Phys. Lett.*, 28, 410.

Alt'shuler, B. L. and A. G. Aronov and D. E. Kmel'nitskiĭ, 1982, *J. Phys. C: Solid State Phys.*, 15, 7367.

Alt'shuler, B. L. and A. G. Aronov, 1979(a), *Pis'ma Zh. Eksp. Teor. Fiz.*, 30, 514, (*JETP Lett.*, 30, 482).

Alt'shuler, B. L. and A. G. Aronov, 1979(b), *Solid State Commun.*, 30, 115.

Alt'shuler, B. L. and A. G. Aronov, 1979(c), *Zh. Eksp. Teor. Fiz.*, 77, 2028, (*Sov. Phys. - JETP*, 50, 968).

Alt'shuler, B. L. and A. G. Aronov, 1981, *Solid State Commun.*, 38, 11.

Alt'shuler, B. L. and A. G. Aronov, 1983, *Solid State Commun.*, 46, 429.

Alt'shuler, B. L. and A. G. Aronov, 1985, *Electron-Electron Interaction In Disordered Conductors*, Elsevier Science Publishers.

Alt'shuler, B. L., A. G. Aronov and D. E. Kmel'nitskiĭ, 1981, *Solid State Commun.*, 39, 619.

Alt'shuler, B. L., A. G. Aronov and P. A. Lee, 1980(b), *Phys. Rev. Lett.*, 44, 1288.

Alt'shuler, B. L., D. E. Kmel'nitskiĭ, A. I. Larkin and P. A. Lee, 1980(a), *Phys. Rev. B*, 22, 5142.

Anderson, P. W., 1958, *Phys. Rev.*, 109, 1492.

Anderson, P. W., B. I. Halperin and C. M. Varma, 1972, *Phil. Mag.*, 25, 1.

Anderson, P. W., E. Abrahams and T. V. Ramakrishnan, 1979, *Phys. Rev. Lett.*, 43, 718.

Anderson, P. W., K. A. Muttalib and T. V. Ramakrishnan, 1983, *Phys. Rev. B*, 28, 117.

Ashcroft, N. W. and N. D. Mermin, 1976, *Solid State Physics*, Saunders College, Philadelphia.

Aslamasov, L. G. and A. I. Larkin, 1968(a), *Phys. Lett.*, 26A, 238.

Aslamasov, L. G. and A. I. Larkin, 1968(b), *Sov. Phys. - Solid State*, 10, 875.

Audouard, A., A. Kazoun, J. M. Broto, G. Marchal and A. Fert, 1990, *Phys. Rev. B,* 42, 2728.

Baker, P. N., 1972, *Thin Solid Films,* 14, 3.

Beaglehole, D., private communication.

Bergmann, Gerd, 1971, *Phys. Rev. B,* 3, 3797.

Bergmann, Gerd, 1982(a), *Phys. Rev. Lett.,* 48, 1046.

Bergmann, Gerd, 1982(b), *Z. Phys. B,* 48, 5.

Bergmann, Gerd, 1982(c), *Phys. Rev. B,* 25, 2937.

Bergmann, Gerd, 1982(d), *Solid State Commun.,* 42, 815.

Bergmann, Gerd, 1983, *Phys. Rev. B,* 28, 2914.

Bergmann, Gerd, 1984(a), *Solid State Commun.,* 49, 775.

Bergmann, Gerd, 1984(b), *Phys. Rep.,* 107, 1.

Bergmann, Gerd, 1984(c), *Phys. Rev. B,* 29, 6114.

Bergmann, Gerd, 1987, *Phys. Rev. B,* 35, 4205.

Biswas, R. G., T. E. Whall, N. L. Mattey, S. M. Newstead, E. H. C. Parker and M. J. Kearney, 1993, *J. Phys.: Condens. Matter,* 5, L201.

Bohr, N., 1913, *Phil. Mag.,* 25, 10.

Bronson, R., 1973, *Schaum's Outline of Modern Differential Equations* McGraw-Hill, New York.

Buckley, R. G., 1979, *Ph.D. Thesis,* Victoria University of Wellington.

Chakravarty, S. and A. Schmid, 1986, *Phys. Rep.,* 140, 193.

Cherradi, N., A. Audouard, G. Marchal, J. M. Broto and A. Fert, 1989, *Phys. Rev. B,* 39, 7424.

Chopra, K. L., 1969, *Thin Film Phenomena,* McGraw-Hill Book Company, New York.

Chu, W. K., J. W. Mayer and M.-A. Nicolet, 1978, *Backscattering Spectrometry,* Academic Press, New York.

Climent-Font, A., 1991, *Nucl. Instr. and Meth. in Phys. Res.,* B61, 541.

Coote, G. E. and R. J. Sparks, 1981, *New Zealand Journal of Archaelogy,* 3, 21.

Cote, P. J. and L. V. Meisel, 1981, in *Topics in Applied Physics, Volume 46: Glassy Metals I,* eds.H.-J. Güntherodt and H. Beck, Springer-Verlag, New York.

CRC Handbook of Chemistry and Physics, 1971, 52nd Edition, ed. R. C. Weast, Chemical Rubber Company, Ohio.

Doolittle, L., 1985, *Nucl. Instr. and Meth. in Phys. Res.,* B9, 344.

Elliott, S. R., 1990, *Physics of Amorphous Materials, 2nd Edition,* Longman Scientific and Technical, England.

Faber, T. E. and J. M. Ziman, 1965, *Phil. Mag.,* 11, 153.

Feynman - Lectures III, 1971, eds. R. P. Feynman, R. B. Leighton and M. Sands, Addison - Wesley, London.

Finkel'steĭn, A. M., 1983, *Zh. Eksp. Teor. Fiz.*, 84, 168, (*Sov. Phys. - JETP*, 57, 97).

Fisher, M. P. A., P. A. Matthew, G. Grinstein and S. M. Girvin, 1990, *Phys. Rev. Lett.*, 64, 587.

Fukuyama, H. and K. Hoshino, 1981, *J. Phys. Soc. Japan*, 50, 2131.

Fukuyama, H., 1980, *J. Phys. Soc. Japan*, 49, 644.

Gallagher, B. L., D. Greig and M. A. Howson, 1984, *J. Phys. F: Met. Phys.*, 14, L225.

Garland, J. W., K. H. Bennemann and F. M. Mueller, 1968, *Phys. Rev. Lett.*, 21, 1315.

Gershenzon, M. E., B. N. Gubankov and Yu. E. Zhuravlev, 1982, *Zh. Eksp. Teor. Fiz.* 83, 2348, (*Sov. Phys. - JETP*, 56, 1362).

Ghosh, A. K. and D. H. Douglass, 1977, *J. Low Temp. Phys.*, 27, 487.

Gor'kov, L. P., A. I. Larkin and D. E. Kmel'nitskiĭ, 1979, *Pis'ma Zh. Eksp. Teor. Fiz,.* 30, 248, (*JETP Lett.*, 30, 228).

Hartman, T. E., 1965, *J. Vac. Sci. & Technol.*, 2, 239.

Haviland, D. B., Y. Liu and A. M. Goldman, 1989, *Phys. Rev. Lett.*, 62, 2180.

Hickey, B. J., D. Greig and M. A. Howson, 1986, *J. Phys. F: Met. Phys.*, 16, L13.

Hickey, B. J., D. Greig and M. A. Howson, 1987, *Phys. Rev. B*, 36, 3074.

Hikami, S., A. I. Larkin and Y. Nagaoka, 1980, *Prog. Theor. Phys.* 63, 707.

Homewood, V. J., 1990, *Ph.D. Thesis*, Victoria University of Wellington.

Howson, M. A. and B. L. Gallagher, 1988, *Phys. Rep.*, 170, 265.

Howson, M. A. and D. Greig, 1986, *J. Phys. F: Met. Phys.*, 16, 989.

Howson, M. A., 1984, *J. Phys. F: Met. Phys.*, 14, L25.

Imry, Yoseph, 1980, *Phys. Rev. Lett.*, 44, 469.

Jackson, A. G. and T. W. Haas, 1967, *J. Vac. Sci. & Technol.*, 4, 42.

Jaros, M., 1989, *Physics and Applications of Semiconductor Microstructures*, Clarendon Press, Oxford.

Jin, B. Y. and J. B. Ketterson, 1986, *Phys. Rev. B*, 33, 8797.

Jonson, M. and S. M. Girvin, 1979, *Phys. Rev. Lett.*, 43, 1447.

Kagan, Yu and A. P. Zhernov, 1966, *Zh. Eksp. Teor. Fiz.*, 50, 1107, (*Sov. Phys. - JETP* 23, 737).

Kaveh M. and N. F. Mott, 1981(a), *J. Phys. C*, 14, L177.

Kaveh M. and N. F. Mott, 1981(b), *J. Phys. C*, 14, L183.

Kaveh M. and N. F. Mott, 1982(a), *J. Phys. C*, 15, L697.

Kaveh M. and N. F. Mott, 1982(b), *J. Phys. C,* 15, L707.

Kawabata, A., 1980(a), *Solid State Commun.,* 34, 431.

Kawabata, A., 1980(b), *J. Phys. Soc. Japan,* 49, 628.

Kaye, G. W. C. and T. H. Laby, 1986, *Tables of Physical and Chemical Constants and Some Mathematical Functions, 15ed.,* Longman, London and New York.

Kern, W. and G. L. Schnable, 1987, in *The Chemistry of the Semiconductor Industry,* eds. S. J. Moss and A. Ledwith, Blackie & Son Ltd., Glasgow and London.

Kittel, C., 1986, *Introduction to Solid State Physics, 6th Edition,* John Wiley and Sons Ltd., New York.

Kittel, C. and H. Kroemer, 1980, *Thermal Physics, 2nd Edition,* W. H. Freeman and Company, New York.

Knoedler, C. M. and D. H. Douglass, 1979, *J. Low Temp. Phys.,* 37, 189.

Koshino, S., 1960, *Prog. Theor. Phys.,* 24, 1049.

Larkin, A. I., 1980, *Pis'ma Zh. Eksp. Teor. Fiz.,* 31, 239, (*JETP Lett.,* 31, 219).

Lawrence, W. E. and S. Doniach, 1971, *Proceedings of the 12th International Conference on Low-Temperature Physics, Kyoto,* ed. Eizo Kanda, Academic Press, Tokyo, 361.

Lee, P. A. and T. V. Ramakrishnan, 1985, *Rev. Mod. Phys.,* 57, 287.

Levi, B. G., 1993, *Physics Today,* 46, 17.

Lin, J. J. and N. Giordano, 1987, *Phys. Rev. B,* 35, 545.

Lindelof, P. E. and Shiguang Wang, 1986, *Phys. Rev. B,* 33, 1478.

Lindqvist, P. and Ö. Rapp, 1988, *J. Phys. F: Met. Phys.,* 18, 1979.

Long, N. J., 1989, *Master's Thesis,* Victoria University of Wellington.

Maekawa, S. and H. Fukuyama, 1981, *J. Phys. Soc. Japan,* 51, 1380.

Maissel, L. I. and P. M. Schaible, 1965, *J. Appl. Phys.,* 36, 237.

Maki, K., 1968(a), *Prog. Theor. Phys.,* 39, 897.

Maki, K., 1968(b), *Prog. Theor. Phys.,* 40, 193.

Markiewicz, R. S. and L. A. Harris, 1981, *Phys. Rev. Lett.,* 46, 1149.

Mathieu, H. J., M. Datta and D. Landolt, 1985, *J. Vac. Sci. & Technol.,* 3, 331.

Mattheiss, L. F., 1970, *Phys. Rev. B.,* 1 , 373.

McGinnis, W. C. and P. M. Chaikin, 1985, *Phys. Rev. B,* 32, 6319.

McLachlan, D. S., 1983, *Phys. Rev. B,* 28, 6821.

Meikap, A. K., A. Das and S. Chatterjee, 1993, *J. Low Temp. Phys.,* 90, 281.

Meikap, A. K., A. R. Jana, S. K. De and S. Chatterjee, 1990, *Phys. Stat. Sol. (b),* 160, 473.

Mizutani, U., 1983, *Prog. in Mater. Sci.,* 28, 97.

Mizutani, U., 1993, *Phys. Stat. Sol. (b),* 176, 9.

Mizutani, U., K. Sato, I. Sakamoto and K. Yonemitsu, 1988, *J. Phys. F: Met. Phys.*, 18, 1995.

Mizutani, U., M. Tanaka and H. Sato, 1987, *J. Phys. F: Met. Phys.*, 17, 131.

Mooij, J. H., 1973, *Phys. Stat. Sol. A*, 17, 321.

Morgan, G. J. and B. J. Hickey, 1985, *J. Phys. F: Met. Phys.*, 15, 2473.

Morgan, G. J., M. A. Howson and K. Šaub, 1985, *J. Phys. F: Met. Phys.*, 15, 2157.

Mott, N. F., 1972, *Phil. Mag.*, 26, 1249.

Mott, N. F. and E. A. Davis, 1971, *Electronic Processes in Non-crystalline Materials*, Clarendon Press, Oxford.

Nakajima, H., M. Ikebe, Y. Muto and H. Fujimori, 1989, *J. Appl. Phys.* 65, 1637.

Naugle, D. G., 1983, *J. Phys. Chem. Sol.*, 45, 367.

Neerinck, D., K. Temst, M. Baert, E. Osquiguil, C. van Haesendonck, Y. Bruynseraede, A. Gilabert and I. K. Schuller, 1991, *Phys. Rev. Lett.*, 67, 2577.

Neerinck, D., K. Temst, M. Dhalle, C. van Haesendonck, Y. Bruynseraede, A. Gilabert, I. K. Schuller, T. Krekels and G. van Tendeloo, 1990, *Physica B*, 165&166, 473.

Ness, J. M., W. M. Stobbs and T. F. Page, 1986, *Phil. Mag. A*, 54, 679.

Nestell Jr, J. E., K. J. Scoles and R. W. Christy, 1982, *J. Appl. Phys.*, 53, 8993.

Ovadyahu, Z., Yuval Gefen and Yoseph Imry, 1985, *Phys. Rev. B*, 32, 781.

Pang, Tao, 1989, *Phys. Rev. Lett.*, 62, 2176.

Rainer, D. and Gerd Bergmann, 1985, *Phys. Rev. B*, 32, 3522.

Rathnayaka, K. D. D., A. B. Kaiser and H. J. Trodahl, 1986(a), *Phys. Rev. B*, 33, 889.

Rathnayaka, K. D. D., H. J. Trodahl and A. B. Kaiser, 1986(b), *Solid State Commun.*, 57, 207.

Read, Mildred and C. Altman, 1965, *Appl. Phys. Lett.*, 7, 51.

Rosenbaum, K., T. F. Andres, G. A. Thomas and P. A. Lee, 1981, *Phys. Rev. Lett.*, 46, 568.

Ross, F. M. and W. M., Stobbs, 1991, *Phil. Mag. A*, 63, 37.

Rossiter, P. L., 1987, *The Electrical Resistivity of Metals and Alloys*, Cambridge University Press.

Ruggiero, S. T., T. W. Barbee, Jr. and M. R. Beasley, 1980, *Phys. Rev. Lett.*, 45, 1299.

Ruggiero, S. T., T. W. Barbee, Jr. and M. R. Beasley, 1982, *Phys. Rev. B*, 26, 4894.

Sacharoff, A. C. and R. M. Westervelt, 1985, *Phys. Rev. B*, 32, 662.

Santhanam, P. and D. E. Prober, 1984, *Phys. Rev. B,* 29, 3733.

Santhanam, P., S. Wind and D. E. Prober, 1987, *Phys. Rev. B,* 35, 3188.

Schmid, A. Z., 1974, *Physik,* 271, 251.

Schulte, A., A. Eckert, G. Fritsch and E. Lüscher, 1984, *J. Phys. F : Met. Phys.,* 14, 1877.

Schwartz, Newton, W. A. Reed, P. Polash and Mildred H. Read, 1972, *Thin Solid Films,* 14, 333.

Self, P. G. and M. A. O'Keefe, 1988, in *High-Resolution Transmission Electron Microscopy and Associated Techniques,* eds. P. Buseck, J. Cowley and L. Eyring, Oxford University Press, Oxford.

Shearwood, C. and D. Greig, 1991, *J. Phys.: Condens. Matter,* 3, 2937.

Steel, D. G., W. R. White and J. M. Graybeal, 1993, *Phys. Rev. Lett.,* 71, 161.

Strausser,Y. E., 1968, *Proc. 4th Int. Vac. Cong., Part 2,* 469, Institute of Physics, London.

Strongin, Myron, R. S. Thompson, O. F. Kammerer and J. E. Crow, 1970, *Phys. Rev. B* 1, 1078.

Sørensen, E. S., M. Wallin, S. M. Girvin and A. P. Young, 1992, *Phys. Rev. Lett.,* 69, 828.

Tang, C., S. Alexander and R. Bruinsma, 1990, *Phys. Rev. Lett.,* 64, 772.

Tapping, R. L., R. D. Davidson, T. E. Jackman and J. A. Davies, 1988, *Surf. Interface Anal.,* 11, 441.

Thompson, R. S., 1970, *Phys. Rev. B,* 1, 327.

Thompson, R. S., 1971, *Physica,* 55, 296.

Thouless, D. J., 1977, *Phys. Rev. Lett.,* 39, 1167.

Treatise on Materials Science and Technology, 1981, *vol. 20: Ultrarapid Quenching of Liquid Alloys,* ed. Herbert Herman, Academic Press.

Uren, M. J., R. A. Davies, M. Kaveh and M. Pepper, 1981, *J. Phys. C: Solid State Phys.,* 14, L395.

van den Dries, L., C. van Haesendonck, Y. Bruynseraede and G. Deutscher, 1981, *Phys. Rev. Lett.,* 46, 565

Westwood, W. D. and F. C. Livermore, 1970, *Thin Solid Films,* 5, 407.

Williams, G. V. M., 1990, *Ph.D. Thesis,* Victoria University of Wellington.

Yamada, Y., Y. Itoh, T. Matsuda and U. Mizitani, 1987(a), *J. Phys. F: Met. Phys.,* 17, 2313.

Yamada, Y., Y. Itoh, U. Mizutani, N. Shibagaki and K. Tanaka, 1987(b), *J. Phys. F: Met. Phys.,* 17, 2303.

Zallen, R., 1983, *The Physics of Amorphous Solids,* John Wiley and Sons, Inc., USA.

Ziegler, J.F., J. Biersack and U. Littmark, 1982, *Empirical Stopping Power for Ions in Solids*, IBM Research Reports RC 9250.

Ziman, J. M., 1960, *Electrons and Phonons - The Theory of Transport Phenomena in Solids,* Oxford University Press, London.

Ziman, J. M., 1961, *Phil. Mag.*, 6, 1013.